BRNO UNIVERSITY OF TECHNOLOGY

VYSOKÉ UČENÍ TECHNICKÉ V BRNĚ

FACULTY OF MECHANICAL ENGINEERING

FAKULTA STROJNÍHO INŽENÝRSTVÍ

INSTITUTE OF PHYSICAL ENGINEERING

ÚSTAV FYZIKÁLNÍHO INŽENÝRSTVÍ

2D METAL-ORGANIC FRAMEWORKS FROM ORGANIC CARBONITRILE MOLECULES ON WEAKLY INTERACTING SUBSTRATES

2D METALO-ORGANICKÉ SÍTĚ PŘIPRAVENÉ Z ORGANICKÝCH KARBONITRILOVÝCH SLOUČENIN NA SLABĚ INTERAGUJÍCÍCH SUBSTRÁTECH

MASTER'S THESIS

DIPLOMOVÁ PRÁCE

AUTHOR — **Bc. Anna Kurowská**

AUTOR PRÁCE

SUPERVISOR — **Dr. Matthias Blatnik**

VEDOUCÍ PRÁCE

BRNO 2023

BRNO UNIVERSITY OF TECHNOLOGY
FACULTY OF MECHANICAL ENGINEERING

Assignment Master's Thesis

Institut:	Institute of Physical Engineering
Student:	**Bc. Anna Kurowská**
Degree programm:	Physical Engineering and Nanotechnology
Branch:	no specialisation
Supervisor:	**Dr. Matthias Blatnik**
Academic year:	2022/23

As provided for by the Act No. 111/98 Coll. on higher education institutions and the BUT Study and Examination Regulations, the director of the Institute hereby assigns the following topic of Master's Thesis:

2D metal–organic frameworks from organic carbonitrile molecules on weakly interacting substrates

Brief Description:

2D metal–organic frameworks (2D MOFs) allow a precise positioning of (magnetic) atoms into long–range ordered superstructures. At the surface of a material, this holds powerful possibilities, e.g., to change the electronic properties of an electronic device or enable the usage of exotic new states of matter in device technology. In this project, we aim to test a suitable candidate for an organic linker in such a 2D surface MOF using a large carbonitrile molecule (e.g., HATCN). We first investigate the formation of the 2D MOFs on a highly studied substrate, e.g., the Au(111) surface, to determine viable strategies for the formation on a more complex surface. As a second step, we then aim to transfer the obtained knowledge to a weakly interacting substrate, e.g., graphene on Ir(111) or Bi2Se3(0001).

Master's Thesis goals:

1) Review the status of the art of molecular adsorption and metal organic network formation from organic carbonitrile molecules on relevant substrates;
2) Experimental: Study the adsorption and formation of phases of large carbonitrile molecules at a low index coinage metal surfaces;
3) Experimental: Investigate the co–deposition of organic molecules with metal atoms and possible formation of a 2D metal–organic framework on the same coinage metal surfaces;
4) Experimental: Transfer the obtained knowledge to a weakly interacting surface, e.g., graphene/Ir(111) or Bi2Se3(0001), and study the formation of 2D MOFs on these substrates;

Recommended bibliography:

IBACH, H. Physics of surfaces and interfaces. Berlin: Springer, 2010. ISBN 978-3-642-07107-2.

LÜTH, Hans. Solid surfaces, interfaces and thin films. Sixth edition. Berlin: Springer, 2015. Graduate texts in physics. ISBN 978-3-319-10755-4.

Supramolecular chemistry on surfaces: 2D networks and 2D structures. Editor Neil R. CHAMPNESS. Weinheim: Wiley-VCH, 2022. ISBN 978-3-527-34491-8.

ORTMANN, Frank, Stephan ROCHE, Sergio O. VALENZUELA. Topological Insulators, Wiley-VCH, 2015, ISBN: 978-3-527-33702-6.

TSENG, Tzu Chun. TCNQ-based Supramolecular Architectures at Metal Substrates, PhD thesis, 2010.

WON, Sang-Yeon, Ji-Hoon KIM, Howon KIM, Jong Keon YOON, Se-Jong KAHNG, Young-Kyun KWON a Yongsup PARK. Linear and Hexagonal Porous Structures of an Organic Charge Acceptor Hexaaza-triphenylene-hexacarbonitrile on Au(111) with CN···CN Dipolar Interactions. The Journal of Physical Chemistry C. 2013, 117(41), 21371-21375. Dostupné z: doi:10.1021/jp407173w;

PIA, Ada Della, Simone LISI, Oreste De LUCA, et al. TCNQ Physisorption on the Topological Insulator Bi 2 Se 3. ChemPhysChem. 2018, 19(18), 2405-2410. Dostupné z: doi:10.1002/cphc.201800259

CAPUTO, Marco, Mirko PANIGHEL, Simone LISI, et al. Manipulating the Topological Interface by Molecular Adsorbates: Adsorption of Co-Phthalocyanine on Bi 2 Se 3. Nano Letters. 2016, 16(6), 3409-3414. Dostupné z: doi:10.1021/acs.nanolett.5b02635

JAKUB, Zdeněk, Anna KUROWSKÁ, Ondrej HERICH, Lenka ČERNÁ, Lukáš KORMOŠ, Azin SHAHSAVAR, Pavel PROCHÁZKA a Jan ČECHAL. Remarkably stable metal–organic frameworks on an inert substrate: M-TCNQ on graphene (M = Ni, Fe, Mn). Nanoscale. 2022, 14(26), 9507-9515. Dostupné z: doi:10.1039/D2NR02017C

DE LA RIE, Joris, Mihaela ENACHE, Qiankun WANG, Wenbo LU, Milan KIVALA a Meike STÖHR. Self-Assembly of a Triphenylene-Based Electron Donor Molecule on Graphene: Structural and Electronic Properties. The Journal of Physical Chemistry C. 2022, 126(23), 9855-9861. Dostupné z: doi:10.1021/acs.jpcc.1c10266

Deadline for submission Master's Thesis is given by the Schedule of the Academic year 2022/23

In Brno,

L. S.

prof. RNDr. Tomáš Šikola, CSc.
Director of the Institute

doc. Ing. Jiří Hlinka, Ph.D.
FME dean

Abstract
Molecular self-assembly is a spontaneous association of molecules into well-defined supramolecular structures on surfaces. Organic molecules exhibiting self-assembly can act as building blocks at the nanoscale and allow for a bottom-up synthesis of atomically precise arrangements, e.g., two-dimensional (2D) nanoarrays. The incorporation of metal atoms leads to the formation of a 2D metal-organic framework (2D MOF). Therein, embedded (magnetic) metal atoms are arranged in a periodic way, linked by organic linker units. At the surface of a material, this holds powerful opportunities, e.g., to change the electronic properties of a material or enable the usage of exotic new states of matter in device technology. This thesis studies assembled structures of carbonitrile molecules and transitional metal atoms on coinage metal and topological insulator surfaces. The molecules HATCN and DCA are tested as suitable candidates for organic linker units. We present especially LEEM and STM results for molecular self-assembly on both types of surfaces and for the metal-organic structure formation on coinage metals. In particular, the DCA molecules show high potential as a linker. We successfully formed a long-range ordered MOF with Fe atoms on the Ag(111) surface and a molecular self-assembly was observed for DCA deposited on Bi_2Se_3.

Abstrakt
Samouspořádávání je proces spontánního uspořádávání molekul do definovaných supramolekulárních struktur na površích. Organické molekuly vykazující schopnost samouspořádání mohou být použity jako stavební prvky pro výrobu struktur přístupem "bottom-up", který umožňuje syntézu atomárně přesných dvourozměrných (2D) struktur. Začleníme-li do molekulárního uspořádání atomy kovu může dojít k vytvoření 2D sítí organika-kov (2D MOF). Atomy kovu jsou v nich periodicky uspořádány díky organickým molekulám, které je vzájemě spojují. Takovéto struktury na povrchu materiálů mohou vést k zajímavým vlastnostem, např. změně elektrických vlastností materiálů, nebo použití nových exotických stavů hmoty v technologických zařízeních. Tato práce se zabývá studiem struktur na bázi karbonitrilových molekul a atomů přechodných kovů na povrchu ušlechtilých kovů a topologického izolantu. Vybrané molekuly, u nichž budeme studovat možnosti využití jako ligandu, jsou HATCN a DCA. Práce představuje výsledky z metod LEEM a STM pro molekulární samouspořádání na obou typech povrchů, a pro systémy organika-kov jen na ušlechtilých kovech; zejména DCA se ukazuje jako slibná molekula pro tvorbu 2D MOFs. Úspěšně jsme vytvořili periodicky uspořádané MOF s atomy Fe na povrchu Ag(111) a molekulární samouspořádání DCA molekul na povrchu Bi_2Se_3.

Keywords
Self-assembly, metal-organic frameworks (MOFs), long-range order, HATCN, DCA, Fe, Ag(111), Bi2Se3, diffraction, STM, LEEM, XPS.

Klíčová slova
Samouspořádání, metal-organické struktury, dalekodosahové uspořádání, HATCN, DCA, Fe, Ag(111), Bi2Se3, difrakce, STM, LEEM, XPS.

KUROWSKÁ, A. *2D metal-organic frameworks from organic carbonitrile molecules on weakly interacting substrates*. Brno: Brno University of Technology, Faculty of Mechanical Engineering, 2023. 61 s. Supervised by Dr. Matthias Blatnik.

I solemnly swear that I elaborated my master's thesis on the topic of *2D metal-organic frameworks from organic carbonitrile molecules on weakly interacting substrates* independently under the supervision of Dr. Matthias Blatnik, using the materials listed in the bibliography.

Bc. Anna Kurowská

Foremost, I would like to thank my supervisor **Dr. Matthias Blatnik** for his professional guidance, for his advice, and great patience, and for all the text corrections. I am very grateful for all his support and help during laboratory work, data analysis, and final writing. Furthermore, my thanks go to **doc. Ing. Jan Čechal, Ph.D.** and **Ing. Pavel Procházek, Ph.D.**, for consultations on studied topics, valuable advice on working in the laboratory and writing a professional text, and for all text corrections. Last but not least, I thank all my colleagues in the *Molecular Nanostructures at Surfaces* group, for their patience, kindness, and a lot of answered questions, which I always have a lot of. I would also like to mention my classmate **Kristýna Davídková** for being such a dreamteam! Thank you for carrying the burden of our studio together, for support in bad and worse times, and for all problems solved with laughter. A great thanks go to my mother **Petra Kurowská** for unceasing support and patience. Finally, many thanks to my family and friends for their great support, despite the little time I had for them in the last six months.

This work was performed with a support of CzechNanoLab (project ID LM2023051 funded by MEYS CR) at CEITEC Nano Research Infrastructure, BUT.

Bc. Anna Kurowská

Contents

Introduction

Molecular self-assembly is the spontaneous association of molecules into well-defined supramolecular structures. On surfaces, this process is controlled by molecular interactions between neighboring molecules, or atoms, and their interactions with the substrate. The choice of molecules, metal atoms, and a specific substrate therefore directly determines the resulting properties of the resulting structures.

Organic molecules exhibiting self-assembly can act as building blocks at the nanoscale and allow for a bottom-up synthesis of atomically precise arrangements, e.g. two dimensional (2D) nanoarrays. The incorporation of metal atoms leads to the formation of a 2D metal-organic framework (2D MOF). Therein, embedded metal atoms are arranged in a periodic way and linked by organic linker units. They are highly studied on well-defined substrate surfaces, e.g. low index surfaces of noble metals. For these instances their formation and the characterization of their properties can be well established and thus allow, e.g. a precise positioning of (magnetic) atoms into long–range ordered superstructures. At the surface of a material, this holds powerful possibilities, e.g. to change the electronic properties of a material or enable the usage of exotic new states of matter in device technology. Contrary to broad belief, the interaction with the metal substrate, even with that of a coinage metal, strongly masks the intrinsic electronic properties of the MOF. Currently, studies of MOF formations on weakly interacting substrates are highly desired. Topological insulators have recently drawn more and more attention due to their fascinating electronic properties. Some of them are van der Waals, layered materials that can act thus as a possible weakly interacting substrate for the formation of a 2D MOF. Moreover, the introduction of magnetic impurities influences their electronic and magnetic properties and accordingly could lead to several phenomena interesting for devices, e.g. an application of the quantum anomalous Hall effect at elevated temperatures. The presence of change of those properties seems to strongly depend on the nature of the impurities and also their possible clustering. The introduction of ordered and equally distanced monoatomic magnetic surface impurities, as in the case of magnetic metal atoms embedded in a MOF, might enable a highly precise, atomic control at the nano scale. However, the development of the applications is preceded by a fundamental investigation of the physical properties and sequentially by the development of a methodology how to prepare 2D MOFs on surfaces. This master's thesis, therefore, deals first with the with clean surface preparation of multiple crystals in ultra-high vacuum (UHV) and a subsequent search of optimal parameters for self-assembly of the above mentioned systems.

The main aim of this thesis is to form 2D MOF from organic carbonitrile molecules on weakly interacting substrates. This can be subdivided into multiple goals. First, the adsorption and phase formation of two different types of carbonitrile molecules at low-index coinage metal surfaces are studied. The molecules hexaazatriphenylene-hexacarboxinitril (HATCN) and dicyanoanthracene (DCA) are tested as suitable candidates to be applied as an organic linker. The success in MOF formation is given not only by choice of the building blocks and substrate but also by external parameters such as the deposition rate of molecules and metal atoms, in which order they are deposited, or the temperature of the surface. Hence, follow-up, we strive for suitable parameters resulting in the formation of MOFs based on HATCN or DCA molecules and transitional metal atoms first on coinage metal surfaces. In addition, in order to investigate the adsorbed layers on weakly interacting surfaces know-how for the cleaning of samples has to be established and ap-

plied, and the clean surface of the weakly interacting material has to be understood. We further build on the acquired results to transfer the obtained knowledge to the surface of the weakly interacting substrate – in this case the topological insulator Bi_2Se_3. The above-mentioned systems are then investigated by a multi-method surface science analysis using scanning tunneling microscopy (STM), low-energy electron microscopy (LEEM), and X-ray photoelectron spectroscopy (XPS).

The thesis is divided into three chapters. The first chapter is devoted to the knowledge of the theoretical background that is needed to understand the discussed topics. The chosen subjects such as the adsorption on surfaces, self-organization, and interactions involved, or the symmetries of crystal structures in two dimensions, are described first. Next, the state-of-the-art of molecular adsorption and metal-organic network formation from organic carbonitrile molecules on relevant substrates is reviewed. The end of the chapter presents the techniques used for the surface analysis. The second chapter is dedicated to the investigation of the self-assembly of molecular and the metal-organic structures on coinage metal surfaces. It is divided into two parts, the first one is devoted to the HATCN molecule self-assembly and structure it forms with Fe, and the second one explores the DCA molecule and the achieved MOF formation. Both experimental details and a discussion of the results are present in each of the parts. The third chapter dives into details about the surface of the Bi_2Se_3 crystals and the deposition of the two above mentioned molecules. First however, the establishing of a cleaning procedure and related emerging challenges are described. The last part deals with the details of the self-assembly and emerging superstructures of HATCN and DCA molecules on the (111) surface of the Bi_2Se_3 crystal. Finally, the thesis finishes with concluding remarks.

1. Theory

This work studies 2D metal-organic frameworks (MOFs) prepared from organic carbonitrile molecules on weakly interacting substrates. The first part is a theoretical chapter that is devoted to the theoretical background needed to understand the topic and to evaluate experimental results. Subsequently, the studied system will be presented together with current state of the art. The chapter concludes with a brief description of the techniques used for the surface analysis.

1.1. Theoretical background

In order to effectively and correctly analyze measured data, one needs to acquire a certain knowledge of the theory in the field of surface science. Therefore, first and foremost, the chosen topics will be discussed in the following sections to set the background needed to understand the discussed results of this work.

1.1.1. Adsorbates on surfaces

In the fundamental surface science studies atoms and molecules are usually deposited on a surface via the molecular beam epitaxy. Beam of particles can be considered as a gas phase and condensation on the surface is called adsorption, deposited particles are then adsorbates. Condensation is described by an impinging rate, i.e. the number of particles per cm^2 per second. Adsorption can be further divided into chemisorption and physisorption depending on the strength of the interaction between an adsorbate and a substrate. In the case of chemisorption, an adsorbate forms a strong chemical bond – covalent or ionic – with substrate atoms. Meanwhile, van der Waals forces dominate the situation of physisorption leading to the weak interactions. From now on, adsorption is discussed in all cases in this thesis dealing with phenomena showing physisorption. We will thus use only the term adsorption from now on. [1, 2]

Nucleation and growth of islands

Once a particle has condensed from the gas phase, becomes accommodated as an adatom with an adsorption energy E_{ads}. There are multiple processes that could ensue as depicted in Fig. 1.1. First, at any point, the free particle can re-evaporate from the surface. Then it might migrate along the surface with a certain probability via diffusion (this is linked to the energy E_{diff}). This may also lead to adsorption at special sites like edges or other defects. Those individual atomic processes determine the growth of an island in its initial stages. [1]

Deposition creates a population of diffusing single adatoms on the surface. Every atom may encounter one or many other adatoms and thus, besides adsorption at special defect sites, nucleation of more than one adsorbed particle in a cluster might occur. The small clusters are metastable and often decay back into individual atoms. However, with increasing size, the probability of its growth is greater than the probability of decay. There is a critical size defined as the minimal size when the addition of just one more atom makes the island stable. The binding energy of the critical cluster E_{i} (see Fig. 1.1) is approximately given by the number of nearest-neighbor atom bonds. A diffusing particle

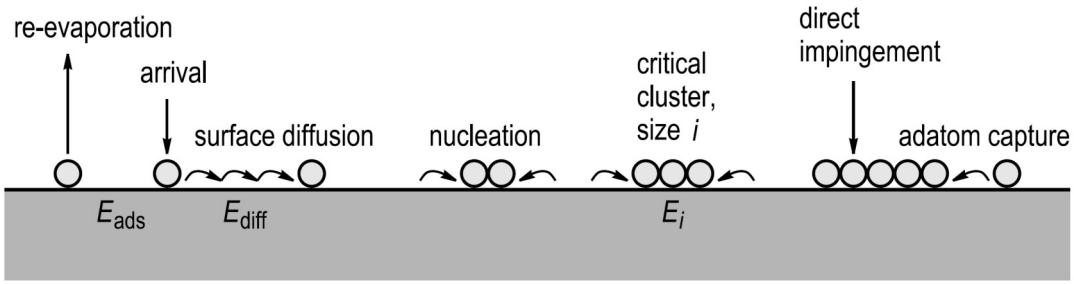

Figure 1.1: Schematic diagram illustrating the atomic processes involved in nucleation and growth on surface. Adsorbed atoms are shown as light grey circles, substrate is depicted as dark grey rectangle. Taken from [2].

might be also captured by an existing cluster or island and contribute to its further growth. Moreover, a particle can impinge on the island while condensation and directly incorporate. [1, 2]

The density of adatoms and islands can be divided into four coverage regimes, which describe the whole process of nucleation and growth of islands. First, in the low-coverage nucleation regime, the adatom density is much higher than the island density. Island nucleation is thus far more probable than the incorporation of an adatom into an existing island. With further deposition, the number of islands increases until it becomes comparable to the density of adatoms. So does the probability of nucleation and incorporation, which is the onset of the intermediate-coverage regime. In this regime, the adatom density reaches its highest point and begins to decrease, whereas the island density still increases yet much more slowly. Saturation of the island density occurs in a subsequent aggregation regime usually at a coverage between 0.1 and 0.4 ML. Henceforward, any further deposition results exclusively in island growth as the mean free path of diffusing adatom is equal to the mean island separation. Finally, in the coalescence and percolation regime, the islands join together, which leads to a decrease in the island number density. [2] The processes works in analogous way when the particle is a molecule containing up to few dozen of atoms, and could thus describe also growth of molecular islands.

In thermodynamic equilibrium, all processes proceed in two opposite directions at equal rates, e.g. condensation and re-evaporation. Therefore, in equilibrium, there is no net growth of islands, i.e. growth itself is a non-equilibrium kinetic process. Nevertheless, in general, certain parts of the overall process may be kinetically hindered, whereas others may be in local thermodynamic equilibrium. Overall, growth of adsorbed layers is controlled by the interplay of thermodynamics and kinetics. [1, 2]

Islands shape

The ability of the captured atom to diffuse along the edges of the island and to cross corners where two edges meet mostly determines the compactness of the island. And the shape of the island may differ in respect to those growth conditions. Therefore, islands can be subdivided into two general classes; ramified islands and compact islands. The formation of ramified islands usually takes place at relatively low temperatures, resulting into slow edge diffusion. Moreover, even if the adatom can diffuse along the island edge, in order to pass across the corner of the island it has to lower its coordination, and thus it might be unable to do such a crossing. In this class, the shape is dendritic with

rough island edges and fractal islands form branches usually with average thickness of a few atoms in width. When adatoms can easely cross island corners, the growth results in formation of compact islands such as of square, rectangular, triangular or hexagonal shape with relatively straight and equiaxial edges. In general, the compact island shape is controlled by the competition between steps of different orientations in accomodating arriving adatoms. The change from fractal-like to compact island growth can takes place for instance with increasing temperature. [2]

Surface diffusion of clusters

As discussed, a cluster can contain up to hundreds adatoms starting from two, and starting from a certain critical size becomes stable and is then called an island. The variety and complexity of diffusion processes are naturally enhanced when the diffusion species is a cluster rather than a single adatom. And depending on particular conditions, the cluster motion can proceed in many ways. Hence, many different mechanisms have been proposed. These might be subdivided into individual mechanisms, based on the motion of a single atom, or concerted together involving simultaneous motion of a group of atoms. In the first case, the displacement of the whole cluster is a result of independent motions of single atoms forming the cluster. Examples for this are a sequential displacement, i.e. one by one motion of single atoms of particular cluster, an edge diffusion mechanism, or an evaporation-condensation mechanism while there is an exchange of adatoms between the cluster and 2D adatom gas. In the second case, a simultaneous correlated motion, such as the gliding of all or just part of the atoms of a cluster, causes the displacement. In general, the larger the clusters the lower the mobility. However, also the shape of the cluster can influence the diffusion. [2]

1.1.2. Organic molecules and metal atoms as adsorbates

Adsorption of particles on the surface is widely used in the bottom-up approach of nanofabrication. And organic molecules and metal atoms adsorbed on a surface represent promising building blocks. The final structure depends not only on the nature of building blocks but also on the interactions between them and with the substrate. Driving forces for the spontaneous arrangement of organic molecules alone or with metal atoms will be discussed in the following subsections.

Self-assembly

Self-assembly is a spontaneous process of molecules creating ordered supramolecular structures driven by a complex set of molecular interactions. For self-assembly on surfaces, molecular interactions can be subdivided into two types. Interactions between molecules and substrate that stabilize the self-assembled structure on the surface, and non-covalent interactions between adjacent molecules. [3, 4, 5] The final supramolecular structure and its properties are given by interplay between the nature of the molecule and a set of external assembling parameters. Foremost, the structural geometry and the functional groups of the molecular building blocks dictate the intermolecular and molecule–substrate interactions. Furthermore, the molecules are thermally evaporated and the structure is prepared via deposition of molecules onto an atomically clean surface. Some of the key external parameters are thus entities like conditions in the environment, deposition rate

and time, nature of the surface, or temperature of the surface. The latter influences especially the kinetics of surface molecular assemblies. The use of ultra high vacuum (UHV) conditions enable careful control of the external parameters, therefore, self-assembly is investigated exclusively in-situ in this thesis. [6]

The nature of the substrate is chosen with respect to two factors. First, although imagining of the self-assembled molecular structure by scanning tunneling microscopy (see Sec. 1.3.2) reveals precise details, it raises a small limitation to work on conductive substrates. [7] Second, the surface does not play a passive role in self-assembly and in order for the molecules to retain the electronic properties that they might show in the gas phase or wet chemistry experiment, substrates that interact very weakly or not at all with molecules are required. [3, 8] Van der Waals forces are generally considered weak long-range attractive interactions between atoms or molecules. And a surface interacting with molecules only by van der Waals forces is usually labeled as weakly interacting. [4] Another example of a weak interaction is the $\pi - \pi$ interaction, which is mainly an interaction between aromatic nuclei. Thus, it is only present if π electrons are present in the system under consideration, such as in the case of organic molecules on graphene.

Non-covalent molecule-molecule interactions are also weak ones, usually mediated via dispersive interactions, or hydrogen bonds. Dispersive interactions usually occur between non-polar molecules, thus between transient dipoles. They belong to the group of attractive van der Waals forces, which, as mentioned, are very weak as their strength decreases with the sixth power of the distance between the atoms. The transient dipoles arise as a result of fluctuations in the instantaneous positions of the electrons, which gives the molecule an instantaneous dipole moment. The strength of the interaction depends on the polarizability of the first molecule. Nonetheless, its strength is relatively small compared to the hydrogen bond. The latter is an attractive interaction between two molecules based on the asymmetric charge distribution in the functional groups. As the name suggests, the bond is mediated by hydrogen atoms creating a link of the form $\mathrm{A}-\mathrm{H}\cdots\mathrm{B}$, where A, B are elements with high electronegativity (often N, O, F) and B has a lone electron pair. Hydrogen bonding is more common in supramolecular systems compared to the dispersion interaction. It is not only stronger but also more directional. [9]

Coordination compounds

In general, coordination compounds are bound by coordination bond. That is a type of bond formed between a functional groups of neutral organic molecule, a ligand, and a metal cation, a coordination centre. Ligands are characterized by a free electron pair, whereas coordination centers by unoccupied states in, e.g. d-orbitals, and thus the ability to accept electrons from ligands. Compared to other types of interactions, the coordination bond is weaker than covalent bonding, and stronger that the above mentioned non-covalent bonds (it has a higher cohesive energy). More over, it retains the attributes of the latter such as being reversible, highly directional and selective. The resulting metal-organic frameworks represent a possibility of periodically arranging a large number of metal centers with atomic precision. [10]

There are multiple bonding theories describing coordination compounds. Their accuracy can be judged according to their ability to explain and predict the number of bonds, shapes of molecules, magnetism and optical properties of coordination compounds. There are essentially three bonding concepts that are used to describe the bonding in coordina-

tion compounds. The first and simplest one is the valence bond theory, which is meant to explain covalent bonding in molecules of main group elements. Both bonds, coordination and covalent, have the common essence of sharing two electrons between two atoms, the coordination bond is thus sometimes also called coordination covalent. However, the origin of the electrons differs. In covalent bonding between two atoms both atoms contribute each one electron to the shared electron pair. In the case of the coordination bond it is assumed that one partner donates an electron pair and the other partner accepts it. Valence bond theory is useful for basic understanding of the bonding mechanism and it can explain the shapes of coordination compounds in some cases. But, overall, it does not work very well for transition metal complexes in view of being a bonding theory mostly for main group element molecules.

The second one is crystal field theory, originally developed to explain colour in ionic crystals, e.g. transition metal ions surrounded by anions. Later, it was found to be suitable also to explain the shapes and magnetism of coordination compounds, e.g. transition metal ions surrounded by ligands. In brief, electrons of all ligands surrounding the metal atom create an electric field, called the crystal field. Due to electrostatic repulsion between the ligand electrons and the metal electrons, the crystal field increases the energy of certain metal d-orbitals. This depends on the spatial arrangement of individual d-orbitals and the crystal field itself. Ligands can be treated as point charges in this case. Although this one is mostly based on repulsive electrostatic interactions, and thus it is per se not a bonding theory, it is often sufficient. It is convenient to use due to its simplicity, especially compared to the last and the most accurate bonding theory.

The third theory is the ligand field theory. It is the most powerful theory – essentially molecular orbital theory applied to coordination compounds – but also the most complicated one. Molecular orbitals can be constructed by a linear combination of atomic orbitals (adapted to the symmetry) just as in molecular orbital theory. However, slightly modified rules apply to optimize molecular orbital theory for coordination compounds due to the greater complexity. Very briefly, first, all molecular orbitals suitable for σ-bonding need to be constructed. Then, one needs to look for ligand orbitals that are suitable for π-bonding with the metal. The metal and ligand orbitals of the same symmetry are then combined to form molecular orbitals. Based on that a molecular orbital diagram for the bonding in the coordination compound can be drawn. [11]

1.1.3. Structural analysis

A solid surface is essentially an imperfection of a crystalline solid by destroying the periodicity of the structure in the third dimension perpendicular to the surface. Since there is no periodicity in the direction normal to the surface, a surface has 2D periodicity parallel to the surface. The vectors span the surface unit cell which sometimes matches the 2D projection of the 3D bulk unit cell. By considering types of 2D grids and possible the possible placement of lattice points, one obtains five lattice systems shown in Fig. 1.2, called Bravais lattices. [12]

Crystal symmetry in 2D

In addition to the five Bravais lattices, the surface can be characterized based on translation symmetry and the corresponding point symmetry elements. By definition, there is a

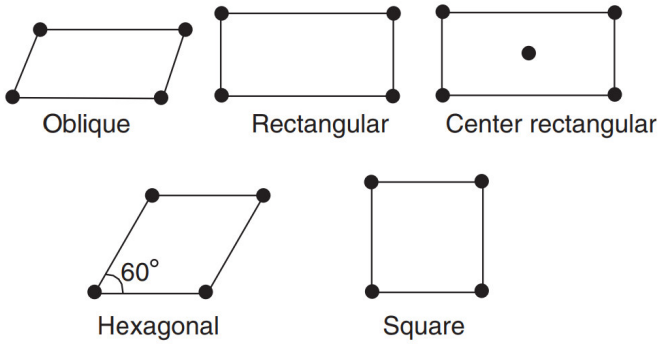

Figure 1.2: The five Bravais lattices – oblique, rectangular, centered rectangular, hexagonal (or also rhombus), and square. Taken from [12]

translation symmetry along the directions defined by the lattice vectors, meaning the grid geometry remains the same with a translation operation. The latter applies also to point symmetry operations. There are only three different types of point symmetry operations that qualify for two-dimensional planes: identity, rotation, and mirroring.

The identity operation only transforms the object into itself. In crystallography, it has a similar function to multiplication by the unit element in mathematics. The rotation symmetry operation generally rotates a point of coordinate $\mathbf{r}$ by a certain angle φ around the center of rotation $\mathbf{r}_0$ to a new coordinate $\mathbf{r}'$. However, only certain rotation angles transform the grid into itself. This limited rotational symmetry is denoted by $C_n(\mathbf{r}_0)$, where n represents the n-fold axis of rotation – the number of rotations during which it transforms into itself before the total rotation angle 360 ° is reached. Permissible axes of rotation are one-, two-, three-, four- and six-fold rotational axis. The mirror symmetry operation transforms a point of coordinates $\mathbf{r}$ into its image $\mathbf{r}'$ with respect to the mirror axis, e.g. with the axis of symmetry x, a point with coordinates $\mathbf{r} = (x, y)$ is transformed to new coordinates $\mathbf{r}' = (x, -y)$. Hence, a grid with mirror symmetry can be divided by mirror axes into two parts that are mirror images of each other. A grid can have multiple mirroring axes and, in general, their frequency corresponds to the n-frequency of rotational symmetry C_n.

There are ten possible types of motifs in 2D, that is, ten unique types of symmetries called point symmetry groups. The less symmetric half of them have 1-,2-,3-,4- or 6-fold axes of rotation but no mirror plane. Another five motifs of higher symmetry are obtained with mirror planes being present. Furthermore, a combination of mirror and translation operations create glide symmetry. The glide plane acts as a mirror plane, only the mirror is shifted by a vector parallel to the glide plane. In total, when five Bravais lattices combined with ten point symmetries and including the possible appearance of a glide symmetry, there are seventeen possible types of patterns in two dimensions called plane groups, that fully describe the symmetry of a surface reconstruction or an adsorbed layer. [13]

Superlattice

A superlattice describes the periodic structure of two (or more) layers of material, e.g. it describes the lattice of the surface reconstruction or the adsorbed layer on the surface via its relation the the pristine substrate.. There is a certain ratio between the lattice vectors

of the substrate and of the adsorbed periodic layer. A superlattice is then called to be commensurate simple if this ratio is of an integer value, e.g. adjacent molecules adsorb on the same side of the surface on every second substrate atom. The superlattice is called commensurate coincidence if this ratio is a rational number, e.g. two molecules adsorb on the same site of the surface separated by 50 molecules in between them not being placed on identical spots. Lastly, an irrational number denotes an incommensurate superlattice.

In a superlattice of hexagonal symmetry, lattice points can be placed into multiple possible positions, out of which two are of interest in this work. The first one is called a honeycomb and is described as a structure where lattice points are placed in the corners of the hexagons. The second one, called a kagome lattice, places lattice points in the middle of the sidelines of the hexagons. Both are depicted in Fig. 1.3 (a) and (b), respectively, and the latter is usually described by the green grid instead of hexagons.

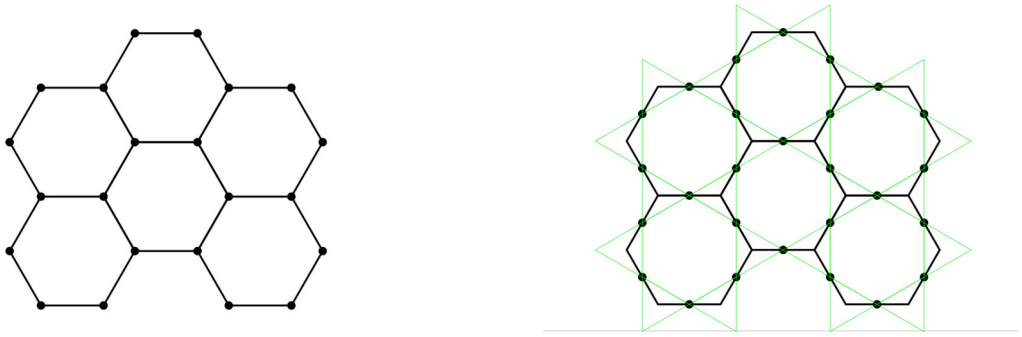

(a) (b)

Figure 1.3: Lattices with hexagonal symmetry - (a) honeycomb and (b) kagome.

Reciprocal lattice

An electron beam hitting the surface of the sample is described by the wave vector $\mathbf{k}_{in}$ and the diffracted electron is then described by the wave vector $\mathbf{k}_{out}$. These wave vectors must satisfy the law of conservation of energy, according to which the magnitudes of both vectors must be equal in the case of elastic scattering. Furthermore, their projections onto a plane parallel to the surface must satisfy the diffraction condition

$$\mathbf{k}_{\mathrm{out}||} = \mathbf{k}_{\mathrm{in}||} + \mathbf{G}_{\mathrm{hk}}. \tag{1.1}$$

The vector $\mathbf{G}_{\mathrm{hk}}$ is a reciprocal lattice vector which is given by the definition

$$\mathbf{G}_{\mathrm{hk}} = h\mathbf{a^*} + k\mathbf{b^*}, \tag{1.2}$$

where h, k are integers and $\mathbf{a^*}$, $\mathbf{b^*}$ are translation vectors of the reciprocal lattice. These reciprocal vectors can be rewritten into real space using the relations

$$\mathbf{a^*} = 2\pi \cdot \frac{\mathbf{b} \times \mathbf{n}}{|\ \mathbf{a} \times \mathbf{b}\ |} \qquad \mathbf{b^*} = 2\pi \cdot \frac{\mathbf{n} \times \mathbf{a}}{|\ \mathbf{a} \times \mathbf{b}\ |}, \tag{1.3}$$

where $\mathbf{n}$ is the unit vector normal to the surface and $\mathbf{a}$, $\mathbf{b}$ are the vectors of the real space lattice [14]. These relations can then be used in the analysis of the diffraction patterns obtained using LEEM in diffraction mode, as described in Sec. 1.3.1.

1.2. Studied systems & state of the art

For the introductory remarks, the title of this work, *2D metal-organic frameworks from organic carbonitrile molecules on weakly interacting substrates*, can be divided into three topical parts: 1) 2D metal-organic frameworks, 2) carbonitrile molecules, and 3) weakly interacting substrates. Two questions can be asked in each of them: what are they and why do we aim for them? The following subsections answer those questions with emphasis on what was already studied, what change is proposed in this work, and what challenges we could face.

1.2.1. Metal-organic frameworks

Metal-organic coordination frameworks (MOFs) are a class of materials based on organized arrays of metal centers and functional molecular linkers [15]. While there are a vast number of reports on three-dimensional, bulk MOFs, the synthesis and characterization of two-dimensional (2D) monolayer thick MOFs are less numerous [16, 17]. Currently, the on-surface, bottom-up, approach of supported MOFs in UHV conditions offers the most detailed view on atomic-scale ordering [18]. Especially, long-range ordered frameworks can be formed on surfaces via self-assembly.

MOFs (from now, MOFs refer to 2D MOFs exclusively, if not specified otherwise) have been recently studied for their promising properties rooted in long-range periodical arrangement, chemical tuneability, and environmental stability [19, 18]. The appealing idea is to controllably adjust the electronic and magnetic properties of MOFs through their building blocks. [20] Moreover, the coordination bond have high cohesive energy compared with other non-covalent intermolecular interactions [10]. That promotes chances of relatively high stability for a MOF structure. The attractiveness lies also in their possible applications, e.g. in catalysis [21, 22], sensing and organic electronics [19, 23], and spintronics [24, 25].

As mentioned, their ability of tuning and the arrangement of the MOFs arrays themself arise from metal atoms and organic molecules. Their choice is key. In particular, linker chemistry, electronic and magnetic interactions among the building blocks, and their interaction with the substrate are crucial factors. [16] A profuse variety of existing metal atoms and organic molecules leave us with a broad choice of combinations for systems to be studied. In this work, we are interested in carbonitrile molecules being the linkers for transition metal atoms, specifically iron (Fe), or nickel (Ni).

1.2.2. Carbonitrile molecules in MOFs

Organic molecules represent a promising class of building blocks within the bottom-up approach in general. Most importantly it is thanks to their ability to self-assemble into large and complex molecular superstructures driven by intermolecular interactions, as discussed in Sec. 1.1.2. Then also thanks to low manufacturing costs and often easy fabrication from precursor components. [50]

Carbonitrile molecules are molecules containing cyano-functional side groups (–CN), also called carbonitrile groups, which usually contribute to intermolecular interactions via bonds with hydrogen. Carbonitrile groups are electron-deficient and make the molecule a large electron acceptor. Carbonitrile molecules often contain an aromatic compound

as the central part, to which functional groups are bonded. This aromaticity ensures a flat adsorption configuration on surfaces facilitating in-plane intermolecular interactions through the functional group. Currently, one of the popular molecules as a linker in 2D MOFs is the highly electro-negative 7,7,8,8-Tetracyanoquinodimethane (TCNQ, see Fig. 1.4c, upper-most panel). It is the mostly studied on coinage metals, e.g. Au(111) and Ag(111) [10, 26, 27, 28], Cu(100) [29], and lately also investigated on surface of graphene on Ir(111) (Gr/Ir(111)) [18, 30]. The latter shows remarkable thermal and chemical stability [18]. However, there is plenty of other molecules with the potential for the creation of a MOF.

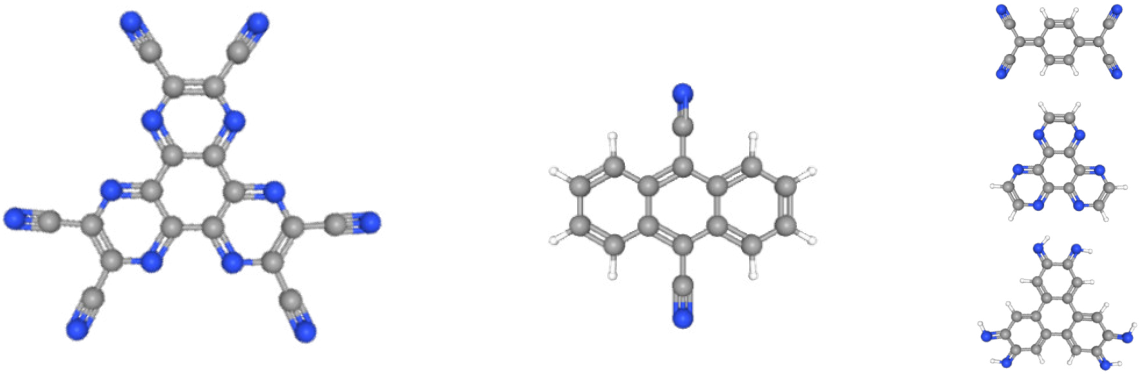

(a) (b) (c)

Figure 1.4: Carbonitrile molecules (a) HATCN and (b) DCA investigated in this work. (c) Other relevant molecules for MOFs mentioned in this work – TCNQ, HAT, HITP, up to down, respectively. (a-c) Balls-and-sticks models of five different organic molecules taken from [31], gray colour represents carbon, blue nitrogen, white hydrogen atoms.

HATCN molecule

One of the two studied molecules in this work is the 1,4,5,8,9,12-Hexaaza-triphenylene-hexacarbonitrile (HATCN) molecule (see Fig. 1.4a). It has a larger molecular size and weight in comparison to TCNQ as one molecule contains in addition eight nitrogen and six carbon atoms. Due to its size, it could have provide higher thermal stability to grown MOF structure on the surface [32]. Its parent molecule 1,4,5,8,9,12-Hexaaza-triphenylene (HAT, see Fig. 1.4c, middle) is one of the smallest flat polyheterocyclic aromatic systems. Compared to triphenylene – polycyclic aromatic hydrocarbons consisting of four fused benzene rings – HAT contains six nitrogen atoms with sp^2 hybridization giving the molecule an electron-deficient character [33]. Those bipyridine side groups can mediate bidentate chelating coordination (i.e. two nitrogen atoms are each involved in bonding to a single metal atom) forming conjugated MOFs with interesting magnetic properties [34].

HATCN, in addition, contains extra electron-withdrawing cyano groups as seen in Fig. 1.4a, which give to the π-conjugated organic system even more electron deficiency [35]. Therefore, HATCN are electron acceptors with a very high ionization energy (9,2 eV) [36]. Despite HAT, and its derivatives, e.g. HATCN, representing a promising class of linkers, until to date, there has been only one study devoted to the investigation HAT-based MOFs [34], and so far none to HATCN-based ones. This is why in this work, HATCN self-

assembly and a possible formation of MOFs including this molecule shall be investigated. Besides, up to date, a monolayer coverage of HATCN self-assembly was investigated on Au(111) [36, 37] and on Ag(111) [32, 38], forming honeycomb structures at atomic terraces. A linear structure was observed at atomic steps.

Furthermore, it has been recently shown that a geometrically similar organic molecule, 2,3,6,7,10,11-hexaiminotriphenylene (HITP, see Fig. 1.4c, bottom panel), coordinates with Ni, Fe, or Cr atoms and creates conjugated MOFs on Au(111) [39, 40, 41], respectively. Metal atoms in those MOFs forms a Kagome lattice with nearest-neighboring ones, while each metal atom is bonded with four nitrogen atoms in nearly square-planar coordination. Moreover, molecular self-assembly of HATP (due to coordination bond with metal deprotonates and thus becomes HITP) leads to honeycomb structure with very similar bonding scheme to the HATCN self-assembly. Therefore, due to mentioned similarities, the symmetry of potential HATCN with Fe coordination MOFs can be presumed as similar to HITP-Fe one.

DCA molecule

The other studied molecule in this work, and nowadays intensively investigated, is 9,10-dicyanoanthracene (DCA) molecule. Compared to the above-mentioned TCNQ and HATCN, it is medium in size with sixteen carbon and two nitrogen atoms. The DCA molecule consists of an anthracene core, which is one of the smallest polycyclic aromatic hydrocarbons containing three fused benzene rings, and of two functional cyano groups as seen in Fig. 1.4b. Kumar et al. showed that the DCA molecules self-assemble via hydrogen bonds into a homogeneous close-packed arrangement on Ag(111) [42], as well as on a single-layer hBN on Cu(111) [43]. In addition, it has been also reported that the molecule forms instantaneous coordination networks with substrate atoms after adsorption on Cu(111) [44, 45] and Au(111) [46]. The observed MOFs form islands or chains, and in case of Au(111) coexist with a close-packed self-assembly of DCA alone. DCA molecules in MOF structures exhibit kagome superlattice, while a honeycomb lattice was observed for embedded metal centres. The same symmetry of the superstructure was shown also for DCA-based MOF formation with non-substrate atoms. DCA coordination with Cu and Co metal centres was observed on Gr/Ir(111) [16, 47], and DCA with Au and Cu atoms was performed on the Ag(111) surface [48, 49]. DCA already proved its ability as a ligand in MOF formation not only on coinage metals and graphene surfaces but also on superconducting substrates. Yan et al. investigated MOF formation of DCA with Cu atoms on $NbSe_2$ surface and reached two phases of MOF formation, one of which is the mentioned honeycomb-kagome. DCA can be thus assumed to form MOFs also on the surface of other van-der-Waals weakly interacting surfaces, e.g. a topological insulator.

1.2.3. Substrates for MOFs studies

Coinage metals

In this work, coinage materials refer to gold and silver single crystals, which both have a face-centered cubic crystal structure. Silver and gold are stable transition metals, and are of the few metals found abundantly in nature as a pure native element. This stability is due to their relative inertness. The samples studied in this work are monocrystals

with a surface orientation of (111), which has also the lowest energy among the high-symmetry surfaces. The clean Ag(111) surface plane exhibits a close-packed, hexagonal structure with unit cell vector $a_{\mathrm{Ag}} = 0.2889\,\mathrm{nm}$ [51]. The clean Au(111) sample plane exhibits a close-packed surface as well, with unit cell vector $a_{\mathrm{Au}} = 0.2884\,\mathrm{nm}$ [51]. The latter moreover displays the well-known herringbone reconstruction, i.e. the top layer densifies by inserting an extra Au atom into an ⟨110⟩ atomic chain every twenty-two lattice constants. That results in a slight surface corrugation and formation of a moiré superlattice.

Surfaces of coinage metals are longtime known and their behavior is well studied. Thus, so far, MOF formation is mostly investigated on coinage metal surfaces (see Sec. 1.2.2 for examples). However, the interaction with the metal substrate strongly masks the intrinsic electronic properties of the MOF [47]. Therefore, currently, studies of MOF formation on weakly interacting substrates are highly desired. Substrates such as graphene, or other van der Waals layered materials, and bulk insulators, might enable to isolate intrinsic electronic properties of the MOF from the substrate [52]. Despite being mentioned, due to the extended knowledge of the substrates, coinage surfaces remain ideal model surfaces for the investigation of self-assembled structures. Once a MOF formation is reached on such a model surface, it is easier to transfer the achieved knowledge to the less known weakly interacting surface.

Bismut selenide

The weakly interacting substrate studied in this work is a bismuth selenide crystal (Bi_2Se_3). It belongs to the family of strong topological insulators (TIs), which are a class of materials with uncommon electronic properties. Its main characteristic is having an insulting bulk and topologically protected, spin-momentum-locked and gapless surface states [53, 54]. It is a layered material along the [0001] direction with alternating layers of Bi and Se which creates so-called quintuples (see Fig. 1.5). The sequence within one quintuple layer (QL) is Se-Bi-Se-Bi-Se and interaction between Bi and Se layers shows a strong covalent bonding character. Van der Waals forces bond neighboring QLs and are therefore responsible for easy cleavage between layers. [6, 55, 56] As one QL is on both sides Se-terminated, naturally cleaved surfaces are expected to be Se terminated as well and have extremely low surface activity toward adsorbates [57].

An atomically clean surface of Bi_2Se_3 is usually reached either by cleavage of the crystal [58, 56, 59], or by deposition of thin films [56]. Cleavage can be executed by a carbon tape (graphene-like exfoliation) or a mechanical cleaver and takes place in-situ, in UHV conditions, or ex-situ. According to Zhou et al., carbon tape induces more defects, which influences surface termination and the adsorption of contaminants, while mechanical cleavage can produce nearly atomically flat surfaces. In-situ exfoliated surfaces are well-ordered and Se-terminated, whereas surfaces prepared by ex-situ exfoliation are less well-ordered, contain adsorbed contaminants, and could be either Se-terminated or richer on Bi. [6]

On account of Bi_2Se_3, and TIs in general, substrate being weakly interacting, they is predicted to preserve intrinsic electronic properties of adsorbed MOFs. That being said, TI surfaces introduce another motivation for MOF formation. TIs are barely influenced by adsorbed and self-assembled non-magnetic structures. However, the introduction of magnetic impurities (such as 3d transitional metals) influences the electronic and magnetic

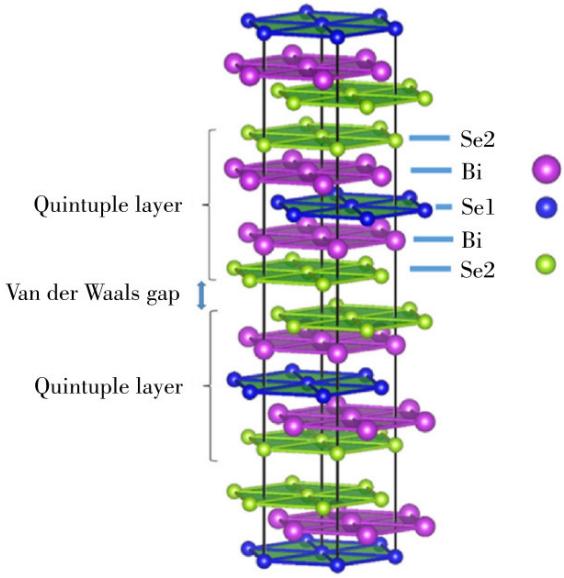

Figure 1.5: Ball-and-stick model of the crystal structure of Bi_2Se_3 with QLs and van der Waals gap between neighbouring QLs outlined. There are two types of selenium atoms within one QL, named here Se1 and Se2. Taken from [54].

properties of TIs. The effect on these properties seems to strongly depend on the nature of impurities and their possible clustering. Therefore, ordered and equally-distanced adsorption of known surface magnetic impurities, e.g. highly ordered MOF, would increase control over the change. An ordered array of magnetic metal adatoms should spontaneously break time-reversal symmetry and thus introduce a band gap in the topological surface state. [58, 60, 61] This could accordingly lead to several phenomena interesting for devices, e.g. the anomalous quantum Hall effect [62, 63].

Up until now, there are few reports about molecular self-assembly on Bi_2Se_3 [58, 64, 65], and none about MOFs. Della Pia et al. recently showed the self-assembly of strong electron acceptor molecules TCNQ on $Bi_2Se_3(0001)$ with the aim of subsequent MOFs formation in the future. They showed that adsorption of TCNQ alone on Bi_2Se_3 does not significantly modify the TI surface electronic states as it represents a non-magnetic impurity. And that molecules arrange into the same characteristic pattern which was also shown on graphene [4, 66], and coinage substrates [10, 26, 27, 28].

1.3. Experimental techniques

This thesis deals with the growth of structures on surfaces and coverages up to a monolayer. As the properties of the surface are very different from the internal parts of the solid, appropriate experimental techniques are needed. A high surface sensitivity is required in order to allow analysis of grown structures and their description at the atomic level. The techniques used in this work include X-ray photoelectron spectroscopy, which is introduced in the following Sec. 1.3.3, scanning tunneling microscopy (Sec. 1.3.2), and low-energy electron microscopy (Sec. 1.3.1). As mentioned above, our experiments are performed in UHV conditions and a schematic of the UHV cluster at CEITEC Nano infrastructure is depicted in Fig. 1.6.

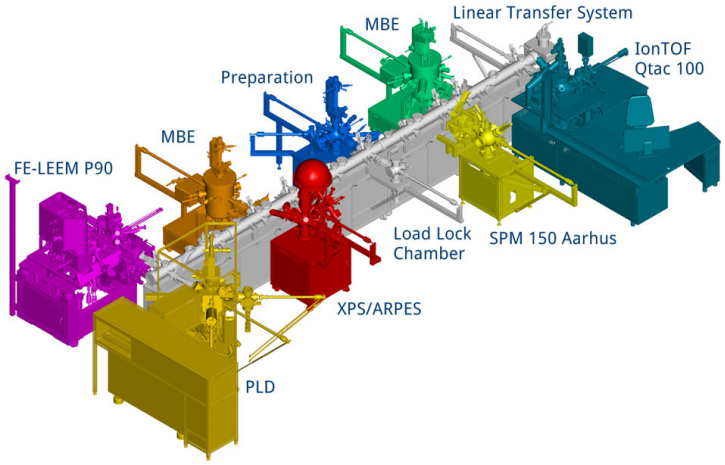

Figure 1.6: Schematic of UHV cluster at CEITEC Nano. Used techniques are XPS, LEEM, SPM, preparation of samples is performed in Preparation chamber and MBE.

1.3.1. Low Energy Electron Microscopy

Low energy electron microscopy (LEEM) image acquisition is based on the principle of elastic electron scattering on surfaces. Electrons hit the sample with low energy and those that are reflected are used to form a surface image. To some extent, the lower the energy is, the fewer are electrons able to penetrate. This is true until certain minimal energy and it is connected to the mean free path. The Fig. 1.7a shows the average mean free paths of electrons inside a solid (universal curve) in the energy range of 2–10,000 eV [12]. LEEM uses electron energies typically well below 100 eV, with a penetration depth in the range of 0.5−5.0 nm, which corresponds to only a few atomic layers of material. Therefore, this technique is highly surface sensitive and thus is suitable for the study of monolayers of molecules self-assembled on surfaces. [2]

Microscope set-up

A schematic of the LEEM system is presented in Fig. 1.7b. The LEEM column can be divided into two parts, an illumination and an imagining one, interconnected by a magnetic beam separator (called prism) bending the trajectory of the electron by 90 ° into the sample stage part of the microscope. The electron beam is formed in the illumination part, and the imagining part transfers scattered particles and collects them to finally generate an image.

Electrons, emitted from a cold cathode by field emission, leave the gun with relatively high energy (8 − 15 keV). This energy is reached by the negative potential relative to the rest of the column and the grounded objective lens. Subsequently, electrons pass a set of illumination lenses to be shaped into a beam. After deflection by the magnetic prism, the beam is focused onto the sample by the objective lens. The sample, same as the electron gun, is kept at high negative potential. Thus, electrons are decelerated to low energy of 0 − 100 eV before hitting the surface. Electrons scattered by the sample are re-accelerated due to the potential difference and collected again by the objective lens. The prism deflects the electrons into the imaging column, where the projector lenses and further the detector screen are located. [2, 68]

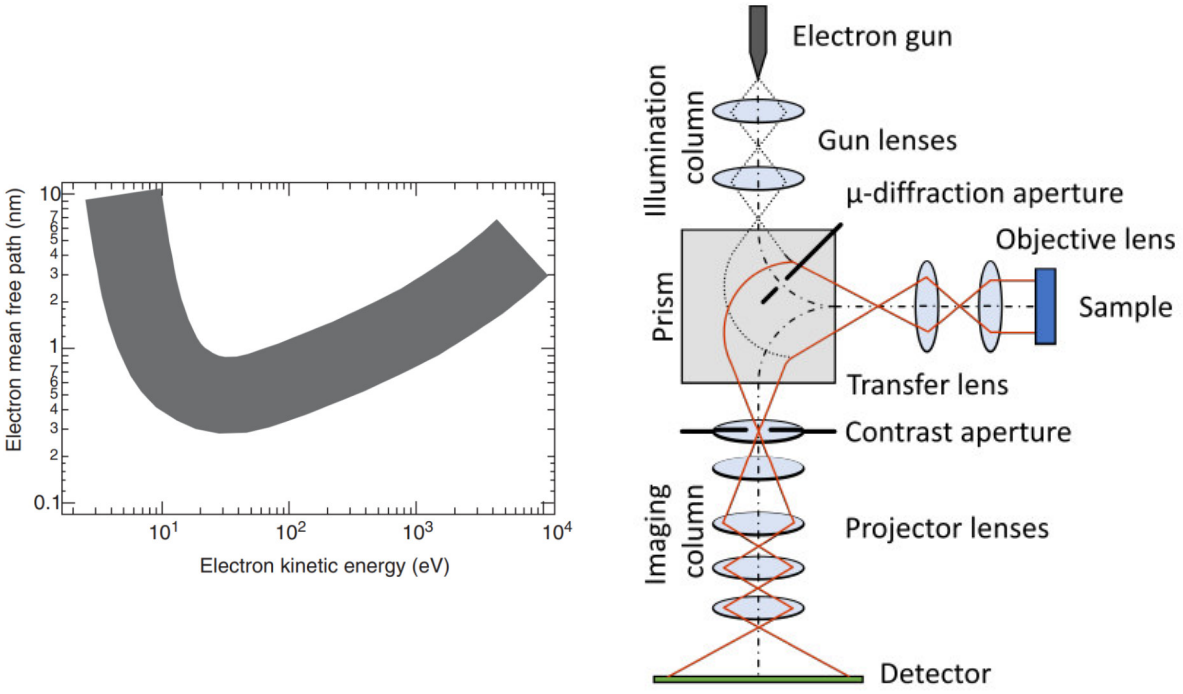

(a) (b)

Figure 1.7: (a) Universal curve of the average mean free paths of electrons inside a solid in the energy range of 2–10,000 eV. Taken from [12]. (b) Schematics of electron optics of the LEEM set-up. Taken from [67].

Imagining with LEEM

Imagining with LEEM typically starts with the sample approaching and tilt alignment with the help of a photoemission electron microscopy (PEEM) build in the set-up. Here, the sample is illuminated by a laboratory UV lamp (hv = 4.9 eV), and photoelectrons are excited. Electrons are collected and directly imaged by the image column. PEEM thus excludes the effects of the illumination optics. Once the electron beam is hitting the sample, electrons scattered from the surface are collected. Depending on adjustments of the magnetic lenses in the imagining column, it is possible to switch between two modes: imaging a diffraction pattern or imagining the real space image obtained from the diffraction pattern.

More detailed, the Fraunhofer diffraction pattern is created in the back focal plane of the projector lenses, where the electrons diffracted in the same direction cross their paths. The direction of electron propagation after scattering is determined by the 2D lattice of atoms arranged on the surface. The Fraunhofer diffraction pattern shows reciprocal lattice and it is a Fourier transform of the atomic arrangement in the real space lattice. [12] Imaged diffraction pattern obtained from clean Ag(111) surface is shown in Fig. 1.8a. Through a deeper study of the diffraction pattern, it is possible to determine the periodicity and symmetry of the surface structures and to find the appropriate arrangement of the adsorbed layer. For instance, the grey vectors and the rhombus depicted in Fig. 1.8a denote unit cell of silver lattice. One can also insert a micro-diffraction aperture in the path of the beam before contact with the sample. That enables measuring diffraction patterns from a small area of size in the order of few μm. Those are called micro-diffraction

patterns and are especially useful to detect individual patterns for different rotational domains of superstructures on the surfaces. They might be colored and merge into one image, in order to determine points of individual domains in complex diffraction patterns.

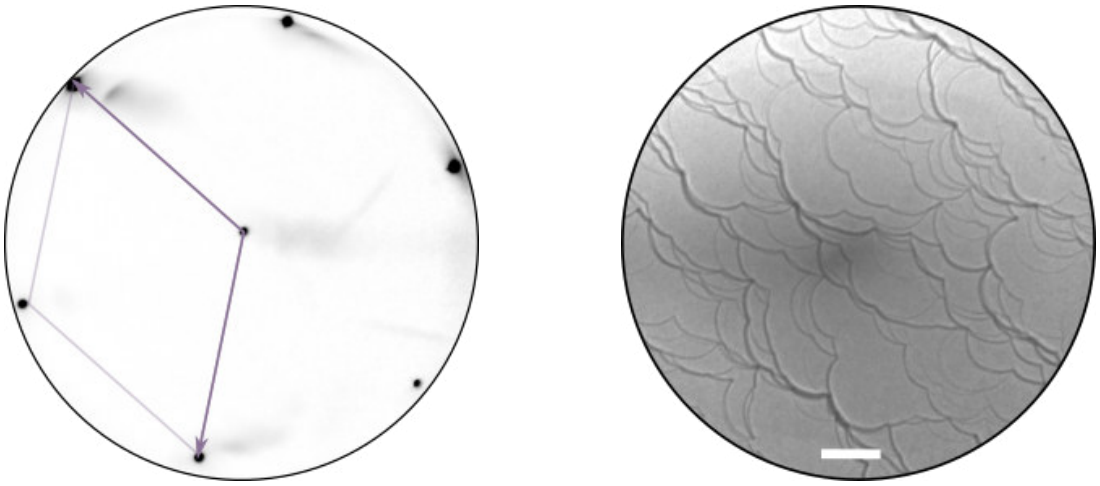

(a) (b)

Figure 1.8: Clean Ag(111) surface imaged by LEEM. (a) Diffraction pattern with inserted unit cell defining hexagonal surface symmetry. (b) Bright field image shows dark lines which corresponds to atomic step of silver, light grey area are thus atomic terraces. The white scale bar indicates a unit of 1 μm in length. Parameters: 5 eV, 4A and 30 eV, 3A, respectively.

In real space then, a contrast aperture is inserted in the back focal plane (where the diffraction pattern is formed) to increase the resolution. Thereby, one of the diffracted beams is chosen to be imaged. For bright field measurements, the contrast aperture lets only pass the central spot. The LEEM contrast arises from local differences in scattering and reflectivity properties of the surface e.g. crystal orientation, surface reconstruction, and adsorbate coverage. Accordingly, a different coverage or thickness of adsorbed layer shows different intensities in the bright field image. This is caused by the phase effects of the scattered electrons. Atomic steps of a surface appear as dark lines in bright field images, see Fig.1.8b, because of interference from electron waves reflected from higher and lower terrace around step edge. Next, for so-called dark-field measurements, one of the beams reflected at a non-zero angle is chosen to be imaged by the contrast aperture. In this way, one can identify and image regions of identical symmetry and with different rotational alignments over the substrate, i.e. domains. It is usually used to identify different domains of molecular self-assembly. Dark field images are colored based on colouring of individual domains in micro-diffraction patterns and also merged into one image. If compared to the bright field image of the same area, the molecular islands can be linked to individual rotational domains.

In further description of experiments, both, micro-diffraction and contrast, apertures are denoted as XA when used, as seen in description of parameters in Fig. 1.8. The letter A is an abbreviation of the word aperture, and X stands for an integer in the range $1-5$ referring to the size of the aperture (from larger to the smallest, respectively).

1.3.2. Scanning Tunnelling Microscopy

Scanning tunnelling microscopy (STM) is based on the quantum mechanical tunnelling effect. Electron tunnelling is thereby used as the mechanism to probe the surface. The probe particle has a certain probability of tunneling to the other side of a barrier, which is energetically too high to be overcome according to classical physics. This probability is given by the transmission coefficient

$$T \approx \exp^{-2\varkappa L}, \qquad \text{where} \qquad \varkappa = \sqrt{\frac{2m_{\mathrm{e}}(E_{\mathrm{p0}} - E)}{\hbar^2}}, \tag{1.4}$$

with L the width of the barrier, m the mass of the particle, $\hbar$ the reduced Planck constant, E_{p0} the potential energy of the barrier and E ($< E_{p0}$) the energy of the particle [69].

STM belongs to a wider class of techniques applying a scanning probe, where it is typical to record and display the signal depending on its position. The potential barrier is represented by the vacuum in between two conductors, a studied sample and a sharp metal tip (the probe). The latter is moving in close proximity above the surface and the tunneling current (signal) between the tip and the sample is measured depending on the position x, y [1, 71] as demonstrated in Fig. 1.9a. Since vacuum, as a potential barrier, is

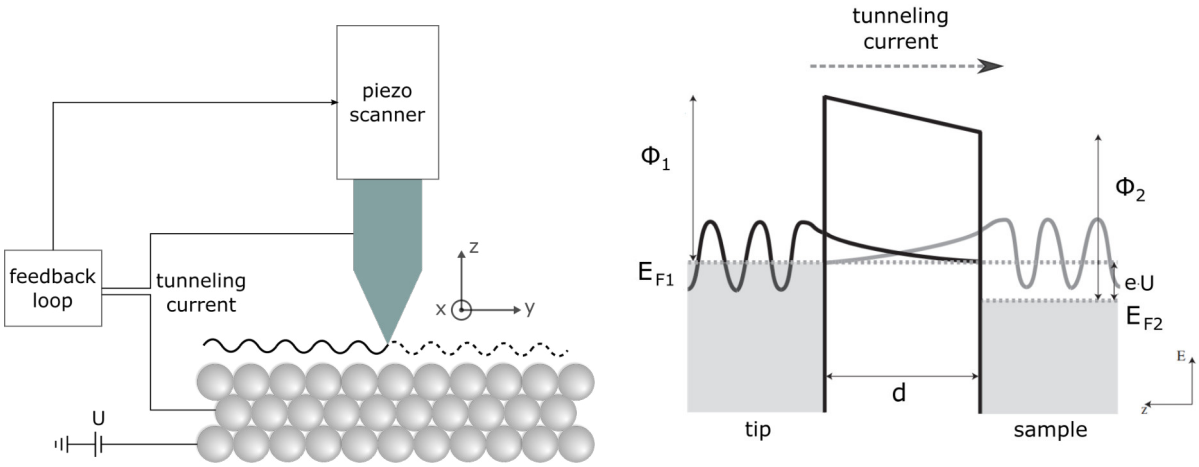

(a) (b)

Figure 1.9: (a) A schematic of STM probing mechanism. (b) A schematic illustration of the wave function overlap in the classical forbidden region between the sample and the tip. A positive bias voltage U is applied to the sample and the barrier height Φ_1 and Φ_2 are indicated. (b) Taken from [70].

of finite dimensions in z direction, wave functions of electrons can leak through it. As the last atom of a sharp tip and the atoms of the surface are in such proximity, the leaking wave functions can overlap in the forbidden region of the barrier [2], see Fig. 1.9b. The overlap is significant, and the tunneling current is well measurable, only for a vacuum gap in the order of tens of ångstöms. The arising tunneling current I_{T} is exponentially dependent on the distance d from the tip to the sample and can be written down as

$$I_{\mathrm{T}} \propto \frac{U}{d} \cdot \exp\left(-Kd\sqrt{\overline{\phi}}\right), \tag{1.5}$$

therein U is the applied bias voltage between the tip and the surface, $\overline{\phi}$ is average work function ($\overline{\phi} \gg eU$) representing the potential barrier and K is a constant. [1]

If surface and tip are on the same potential, e.g. grounded, the potential barrier will be symmetrical, electrons will tunnel in both directions, and the total current will be zero. By applying a bias voltage U between the tip and the surface, the symmetry disappears, as shown in Fig. 1.9b, and a tunneling current arises. STM can be typically operated in two modes – constant height and constant current. The latter is demonstrated in Fig. 1.9a and it is also the mode used in our measurements. In short, the feedback loop acquire the tunneling current and ensure the reaction of piezoelectric crystal elements, which secure the movement of the tip, in order to retain the current constant. This results in change in z, the tip copy the corrugation the electronic orbital landscape of the surface while scanning, which is then recorded.

Scan control is realized using three piezoelectric crystal elements that ensure movement in three spatial directions – perpendicular to the surface, z, and parallel to the surface, (x, y). In order to achieve this axial resolution, the distance d must be controlled with an accuracy of 0.05−0.10 Å. Accuracy in these dimensions can be reached thanks to the high sensitivity of the tip even to the slightest undulation of the electron density of the surface, caused by the exponential dependence of I_{T} current on the distance d. To achieve lateral resolution (in x, y) at atomic level, the movement of the sharp tip above surface must be controlled within 1−2 Å. Piezoelectric material allows such accuracy. Its characteristic is that after applying an electric voltage, it mechanically deforms. With an applied voltage of tens of volts, the tip moves along each of the axes (x, y, z) with an accuracy of 1 Å. The size of the scanned area ranges from units to hundreds of nm^2. [1, 2]

Scanning provide an image of a convolute of the topography and the electronic orbital landscape of the surface. However, as indicated above, the STM tip is sensitive to the local density of states, and not exactly to the positions of every atom. By applying a positive voltage to the surface relative to the tip, the STM image maps empty electron states. By setting a negative voltage, on the contrary, it displays filled states. Therefore, the height change measured in the STM image corresponds to both topographic protrusions on the surface and an increased local density of states. [2]

1.3.3. X-ray Photoelectron Spectroscopy

X-ray photoelectron spectroscopy (XPS) is a technique using photoelectrons excited by monochromatic X-ray radiation. The basis of this technique is the discovery of the photoelectric effect made in 1887 by H. R. Hertz. It was followed by E. Rutherford in 1914, who connected the measured kinetic energy of the emitted electron, E_{k}, with the radiation energy and the binding energy E_{b} of the electron in the atom through the equation

$$E_{\mathrm{k}} = h\nu - E_{\mathrm{b}}, \tag{1.6}$$

with ν being the X-ray frequency and h Planck's constant. [72] A quantum explanation of this phenomenon was provided by A. Einstein, for which he later received Nobel Prize in 1921. A few decades later, in 1981, K. Siegbahn obtained the Nobel Prize for developing the method of electron spectroscopy for chemical analysis based on Einstein's principle. Physicists nowadays called it X-ray photoelectron spectroscopy.

A schematic of the experimental set-up is shown in Fig. 1.10. X-ray radiation of energy 1486.6 eV (in the case of an aluminum Al K_α anode), or 1253.6 eV (in the case of a magnesium Mg K_α anode) hits the surface and excites electrons from core levels of the atoms in the surface. The photon is absorbed and the electron emitted. A part of the

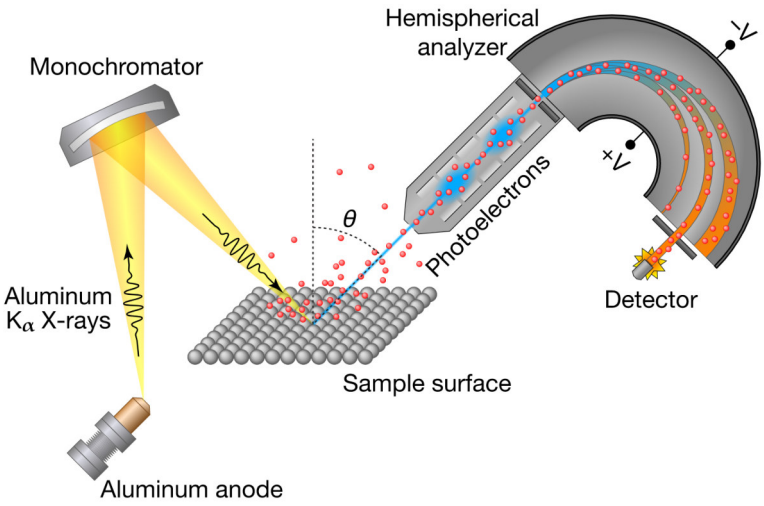

Figure 1.10: Schematics of an XPS set-up. Aluminum (or also magnesium) anode is a source of X-ray radiation. The hemispherical analyzer collects the emitted photoelectrons and serves as an energy filter – photoelectrons are there counted in dependence on their kinetic energy.

gained energy the electron uses to escape the atom, the rest it keeps in the form of kinetic energy. The emitted photoelectrons are collected into a hemispherical analyzer which serves as an energy filter and are there counted in dependence on their kinetic energy, resulting in a typical XPS spectrum. This is depicted in Fig. 1.11. The left panel shows an overview spectra, while the right one is a detailed energy region from $200-400\,\mathrm{eV}$. Elemental identification and information on chemical bonding can then be derived from the measured electron energy and the energy shift, respectively. [72]

Each element of the periodic table is distinguishable due to the specific set of values of the binding energy of excited electrons as energies of core levels are unique for each element. Therefore, there is a peak in intensity of elastically scattered electrons for those specific energies, which allows identifying the element-specific composition of the surface, as seen in Fig. 1.11. Nowadays data-analyzing software contains a database of element peak positions with the possibility of projecting directly into the spectrum (see vertical lines in Fig. 1.11), thus simplifying the evaluation. Furthermore, a measured peak of a given element can be shifted with respect to its characteristic position depending on the bonds with surrounding atoms. A chemical bond between atoms causes an increase or decrease of core levels energies, thus a shift of the peak to higher or lower binding energy, on account of the atoms receiving or giving up electric charge, respectively. [72]

Once photoelectrons escape the atom, there is a great chance of inelastic scattering when passing through the surrounding material. Therefore, electrons leaving the surface without losing kinetic energy are limited to that part of the sample close to the interface with the vacuum. This renders XPS a highly surface-sensitive technique and the depth of characterization is usually around $2-5\,\mathrm{nm}$ [72]. Nevertheless, detection of such electrons that loose part of the transmitted energy due to either inelastic scattering or due to them being excited by bremsstrahlung radiation causes a non-zero intensity in the background of the spectrum [73]. The background intensity decreases in the direction of increasing kinetic energy, i.e. (according to formula (1.6)) in the direction of decreasing binding energy [72], as seen in the left panel of Fig. 1.11.

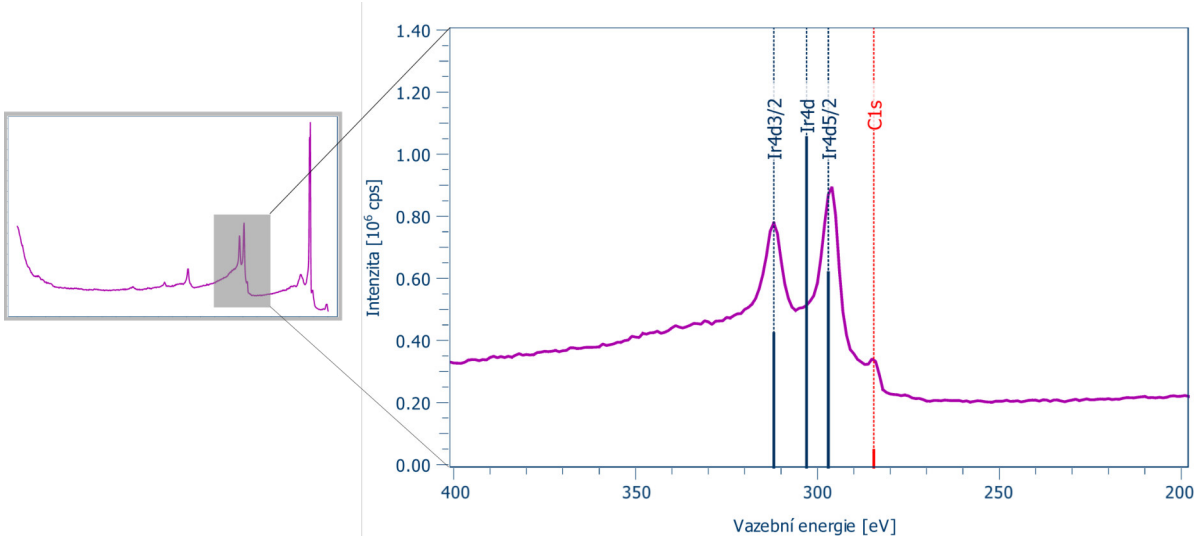

Figure 1.11: Measured XPS spektra for surface of Gr/Ir(111). Left panel shows overview spectra, right panel shows a detailed energy region from $200-400\,\mathrm{eV}$ containing Ir $3d_{3/2}$, Ir $3d_{3/2}$, and C 1s peak. Vertical lines represents tabular values that data-analyzing software supply based on a database.

In general, peaks of a spectrum can originate from various physical processes, e.g. photoelectrons, Auger electrons, or multiparticle scattering. The main peaks in most overview spectra, see Fig. 1.11, originate from the photoelectron process and the electrons being excited from the inner orbitals of the atom of the given element. These are denoted by the abbreviation $Xnl(j)$ consisting of the chemical symbol of the element X and the quantum numbers n, l, or j, which describe the energy level from which the detected electron was excited [73]. For instance, C 1s and Ir $4d_{3/2}$ can be seen in the right panel of Fig. 1.11. Except peaks corresponding to s orbitals, any other peak appears as a doublet in XPS, as seen in Fig. 1.11 for the $4d$ orbital. In brief, it is due to spin-orbit coupling, i.e. an interaction between an electron and its electronic orbital. This process results in the splitting of the orbital, and consequently splitting of the peak. The s orbitals do not produce doublets since they effectively have no orbital angular momentum due to their spherical symmetry.

XPS is sensitive to elemental composition, moreover, to the different chemical environment of elements. Both of the above-introduced molecules, HATCN and DCA contain carbon atoms which could be subdivided into three groups according to their interactions with adjacent atoms. As each bond shifts the position of the carbon peak differently, the measured carbon peak should be theoretically fitted by the same number of peaks, e.g. three. However, correct fitting of an XPS peak is usually more complicated than this one simple rule, requiring a deep understanding of chemical constitution of molecules and their bonding, of secondary physical processes of photoelectrons excitation, of peak shape functions used for fitting, and the interplay of all those factors. In the case of MOFs, there is, in addition, an ab-initio unknown number of coordinated molecules versus those remaining unbonded to metal atoms, resulting in the double amount of peaks and unknown ratios between them. Due to this complexity and time limitations, we will refrain from the fitting of XPS spectra and term it beyond the scope of this work.

2. MOFs on coinage metals

This chapter is devoted to the investigation of molecular and metal-organic structures on coinage surfaces. First, the cleaning procedure for metal surfaces is in brief discussed, followed by two sections – HATCN and DCA. Each section contains both, experimental details and achieved results. For the fabrication of a MOF, it is necessary to study the self-assembly of molecules alone. Thus, the first part of each sections aims to a rough understanding of the monolayer coverage. This then allows for a deeper understanding of a MOF's creation, which investigation is described in the second part of sections.

2.1. Clean coinage metals

Both samples, Ag(111) and Au(111), was cleaned by repeated cycles of ion sputtering (20 min, 1.2 kV) and annealing (5 min, 530 °C). The clean surface was checked in LEEM by the presence of a sharp diffraction pattern and sharp contrast of atomic steps in real space. LEEM data, diffraction pattern and bright field, for Ag(111) is demonstrated in Fig. 1.8a in Sec.1.3.1 of theory part. Atomic steps are active sites for chemical reactions, as well as nucleation and electron scattering centers, but their high density might cause a smaller final size of grown island. Large terraces are preferable for exploring the growth of molecular structures as we aim for large islands of structures. To enlarge terraces very slow cooling (30 min) is applied after the last annealing step allowing the surface atoms to diffuse more effectively.

2.2. HATCN molecules on coinage metal surfaces

Molecules are deposited onto the surface by molecular beam epitaxy and, starting from a certain surface concentration, self-assemble into periodically arranged strucutres as derscribed in Sec. 1.1.1 and 1.1.2. The following part focuses on the adsorption and phase formation of HATCN molecules on the clean surface of Ag(111) and subsequent investigation of HATCN metal-organic structure formation.

2.2.1. Adsorption and phase formation of HATCN

HATCN is evaporated at a temperature 215 °C from the effusion cell placed in the deposition chamber of the UHV cluster. The calibration of the deposition time for HATCN was estimated by a series of sequential depositions. The starting deposition time was 2 min, then multiple 3−4 minute long depositions were performed, until the total time increased to 25 min. Corresponding increase of coverage is observable in the bright field mode of LEEM, see Fig. 2.1a. Growing molecular islands and atomic steps appear as dark areas and lines, whereas brighter areas are the Ag(111) substrate. Imaged coverages include 6 min, 10 min, 13 min, left to right respectively, and the contrast in the latter suggests nearly a monolayer coverage being achieved.

The corresponding diffraction pattern, visualized in Fig. 2.1b, shows a well-known (7×7) superstructure [32], which is commensurate with Ag(111) lattice. The superlattice has six-fold symmetry and was found to be present in one orientation with respect to the substrate. Due to the symmetry of the superstructure with respect to substrate, the

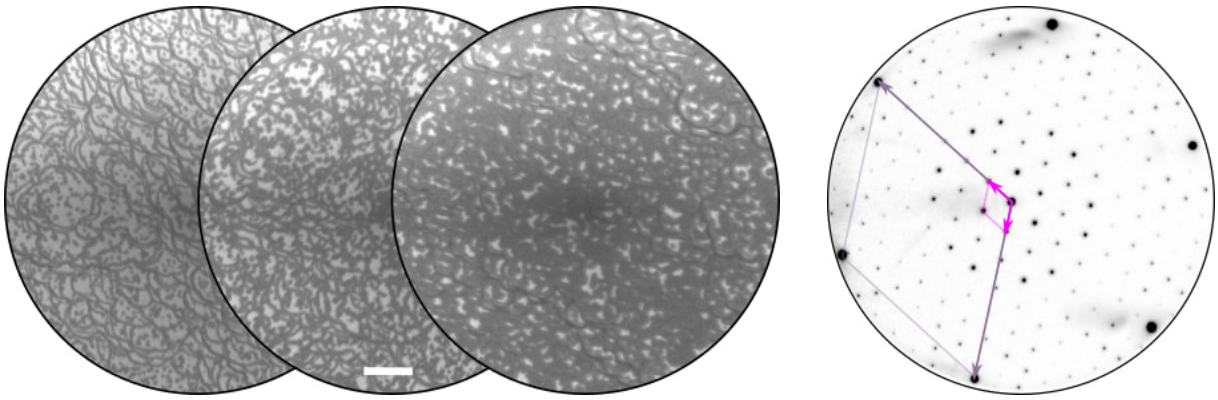

(a) (b)

Figure 2.1: LEEM analysis of HATCN molecules on Ag(111) substrate. (a) Increasing the HATCN coverage on Ag(111) imaged in bright field. Deposition time is 6 min, 10 min and 13 min, left to right. Uncovered silver substrate appear as bright, dark areas and lines correspond to step edges and islands of molecular self-assembly. (b) Difraction pattern of HATCN self-assembly on Ag(111) imaged in LEEM. The vector and unitcell of Ag(111) are visualized in grey, HATCN in pink. Parameters: (a) 5 eV, 4A (b) 30eV, 3A. The white scale bar indicates a unit of 1 μm in length.

rotated and mirrored domains are identical and there is only one visible domain in the pattern. The unit cell vectors of Ag(111) and HATCN have the same directions, and differ only in size as highlighted in reciprocal space Fig. 2.1b in grey and pink, respectively.

Upon deposition of molecules of small amounts, HATCN assembles into honeycomb superlattice on the atomic terraces, which is in accordance with reported self-assembly on Ag(111) [32, 38], and on Au(111) [36, 37]. A high-resolution STM image in Fig. 2.2 (right panel) shows the molecular arrangement on two adjacent terraces and molecules are visible as triangular protrusions. In addition, one can find a linear structure at the edges of the terrace, e.g. the round step flanked by a chain of molecules in the upper left corner of the right panel, or between honeycomb regions. The honeycomb structures are stabilized with three CN$\cdots$CN dipolar interactions per molecule as shown in detail in Fig. 2.2 (left panel). A model of both, the honeycomb and the linear, structures are overlayed over the detailed image to show the bonding scheme between molecules. The color coding ball-and-stick model presents simplified electrostatic potential distributions. The positive and negative potential distributions are represented with red and blue colors, respectively. The green oblique unit cell corresponds to the linear structure, whereas the pink rhombic unit cell refers to the honeycomb structure. The model for honeycomb is taken from Won et al., who investigated HATCN molecular self-assembly on Au(111) [36]. According to their conclusions, the unit cell of the most stable configuration on Au(111) matches well with the one observed on Ag(111). Both contain two molecules per unit cell [32, 36] with the size of $a_{\mathrm{HATCN}} = 2.02\,\mathrm{nm}$. Only the honeycomb structure model was shown in [36]. The linear structure was deduced from our experimental findings, adding information on the bonding mechanism and distances from Won et al.

The surface lattice constant of Ag(111) is $a_{\mathrm{Ag}} = 0.2889\,\mathrm{nm}$, thus $a_{\mathrm{HATCN}}/a_{\mathrm{Ag}} \approx 7$. The honeycomb self-assembly of HATCN, therefore, corresponds to a commensurate (7×7) superstructure [32], which is matching the initial analyses of our LEEM diffraction. The behavior of HATCN on Ag(111) is quite different from that of HATCN on Au(111) com-

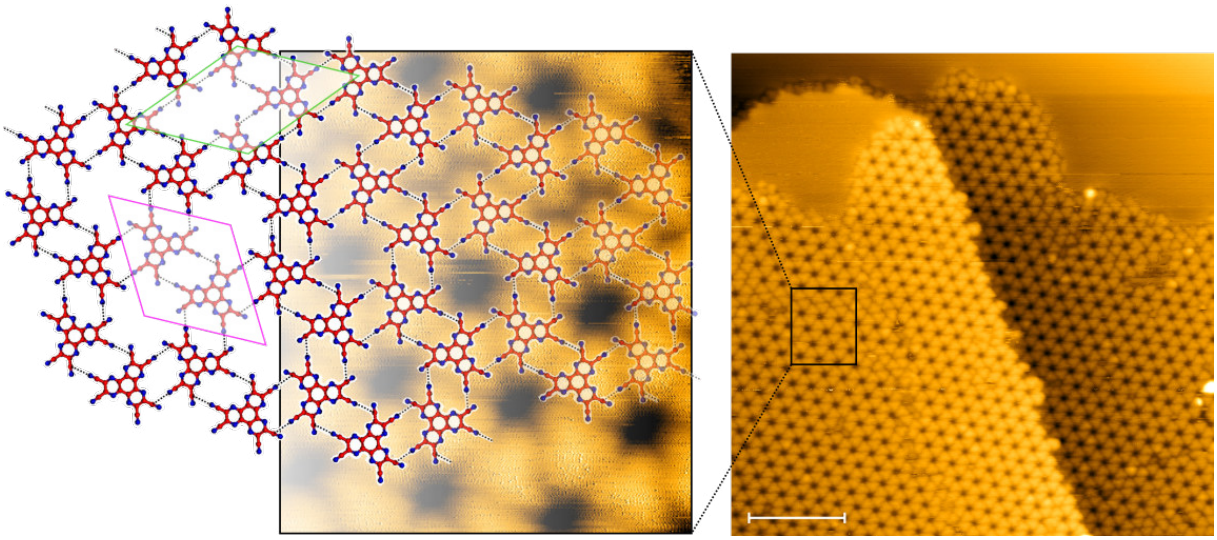

Figure 2.2: STM images of HATCN self-assembly on the Ag(111) surface. The large-scale image (right panel, scale bar 20 nm) shows two appearing patterns - the majority is a honeycomb structure. A few lines of the linear structure are also visible at the edges of the terrace or between honeycomb regions. A small-scale magnified detail of the right panel can be found on the left panel. It is overlayed by a model of molecular bonding scheme for both, linear and honeycomb, structures. The color coding ball-and-stick model, taken from [36], presents simplified electrostatic potential distributions – positive and negative potential distributions are represented with red and blue colors, respectively. Parameters: left panel current 30 pA, bias 2.6 mV, right panel current 40 pA, bias 2.6 mV. The white scale bar indicates a unit of 10 nm in length. Images processed in Gwyddion.

paring equivalent coverage. The diffraction pattern of HATCN on Au(111) consists only of points corresponding to a close-packed gold lattice with additional spots associated with the herringbone reconstruction. No superlattice points indicating periodical arrangement of molecules were observed. That is in accordance with what Frank et al. observed, concluding that based on thermal desorption spectroscopy the adsorbate was very mobile prior to desorption [32, 37]. As discussed in 1.1.1, adsorption begins at special sites such as step edges. In the case of high mobility, these are usually the only sites where to expect the molecules to stick. As a result, the atomic steps of Au(111) are flanked with the chains of molecules as displayed in Fig. 2.3b. No adsorption was observed elsewhere on a terrace in our experiments. However, it has been reported that HATCN molecules on Au(111) form a honeycomb structure. In the already mentioned study, Won et al. successfully mitigate the mobility in low-temperature conditions - deposition at 150 K and measurement at 80 K [36].

Even though HATCN molecules do not possess chirality, due to CN$\cdots$CN asymmetric bonding, the honeycomb structures do show a chirality, which was observed also in [36]. The molecules can thereby bond with their neighbors in the direction of a clockwise or counterclockwise wheel. The latter is also the case of the modeled structure in Fig. 2.2. A change of those two possible structures can be seen in Fig. 2.3a, where a thick green line represents a boundary. The middle part of the molecular arrangement is bound counterclockwise, whereas the upper and bottom parts show a clockwise direction. The difference of lattices in the boundary region, highlighted in green, shows up either as a misalignment of both structures (cyan arrow) or by missing molecules (pink arrow).

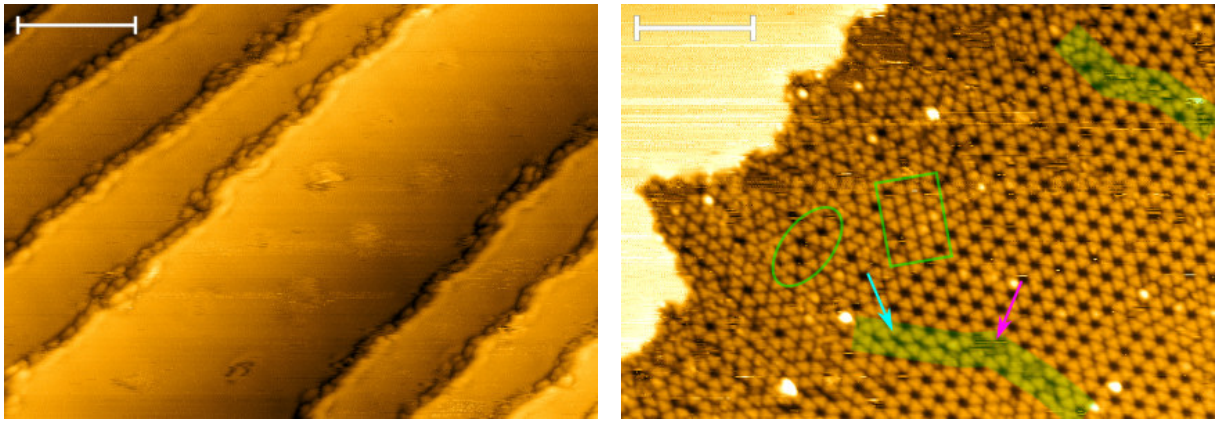

(a) (b)

Figure 2.3: STM images of HATCN self-assembly on the (a) Au(111), (b) Ag(111) surface, both scale bares 10 nm. (a) HATCN at the most favorable adsorption sites, i.e. step-edges, creating a chain of linear structure. (b) Detail of HATCN structure on a bottom edge of an atomic step. A honeycomb structure, dominating the terraces, verge into a compressed disordered arrangement in close proximity to the adjacent step-edge. Few places of both hexagonal and linear structures in the disordered strip around the edge. Parameters: (a) current 40 pA, bias 1.0 mV, (b) current 51 pA, bias 2.6 mV.The white scale bar indicates a unit of 10 nm in length. Images processed in Gwyddion.

The linear structure maintains the direction of bonding, and thus cannot stand for a boundary. In the model overlaying the left panel in Fig. 2.2, it can be seen that the direction of bonding on the edge of the linear chain (upper part of the model) is the same as in the honeycomb structure (bottom part).

An interesting behavior can be observed in the detail of image Fig. 2.3a. There is a transition in the molecular island from a honeycomb structure to a more condensed molecular arrangement. In the latter, the linear structure is partially present, e.g. area in the green rectangle, although without a higher density. Also, a few "rings" of honeycomb structure appear, e.g. area in the green ellipse. We assume here that this constrained structure is caused by an overload of molecules on the lower terrace and that the molecules do not have enough energy to jump onto the upper one to relieve this pressure.

2.2.2. Metal-organic structures with HATCN

Metal atoms can be deposited subsequently after molecules, which is called a sequential deposition, or simultaneously with molecules, called a co-deposition. Fe atoms were evaporated from an effusion cell at a temperature above 1000 °C (exact temperatures are given for each deposition in Tab. 2.1). Nickel atoms were evaporated from a rod, heated via filament at a current of 1.9 nA. The important factors for the formation of a MOF are the impinging rate of particles, condensation effectivity (i.e. how much is re-evaporation negligible), and diffusivity on the surface of both molecules and metal atoms, as described in Sec. 1.1.1.

Once molecular islands are formed and stabilized, sequentially introduced metal atoms are not easily incorporated. The key is either to provide enough activation energy after sequential deposition for both components, e.g. by post-annealing or to introduce metal atoms before molecular islands are formed, e.g. by deposition onto a sample held at

elevated temperature, or by co-deposition. Those strategies can be also combined in order to reach the ideal conditions, e.g. co-deposition on elevated temperature with subsequent annealing, or deposition of a small amount of molecules with subsequent co-deposition. This combination, hence the set of parameters of both depositions and the temperature on which the sample is held, is called a recipe in this work. Despite seeming to be relatively straight-forward self-assembly is often an on trial-and-error-based endavour [5] and so too was our investigation.

All tried recipes are summarized in Tab. 2.1. Prefixes *pre-*, *co-*, and *post-* express whether it was a sequential or simultaneous deposition, or a combination, and in which order. For each recipe in the table, the time of deposition and evaporation temperatures are specified as well as whether the sample was held at room temperature (RT) or at an an elevated one. The easiest recipe to prepare a MOF is to deposit metal atoms after

Table 2.1: Overview of deposition trials with the aim of creating a new recipe for the formation of metal-organic frameworks of HATCN linkers and metal centers on the Ag(111) surface. Temperatures in the co-deposition column denote the evaporation temperature of HATCN and iron (middle line of the boxes) and the temperature of the sample (bottom line of the boxes). An exception is the last row, which corresponds to the experiment with nickel atoms.

Date	Pre-deposition	Co-deposition	Post-deposition	Annealing	STM Fig. 2.6
2.12.	6 min HATCN 210 °C sample RT	-	80 min Fe 1010 °C sample RT	15 min 1.7 A (460 K)	(b)
27.12.	7 min HATCN 215 °C sample RT	70 min 215 °C, 1015 °C 1.55 A (430K)	-	15 min 1.7 A (460 K)	(-)
12.1.	10 min HATCN 210 °C sample RT	-	30 min Fe 1030 °C 1.8 A (480 K)	15 min 1.8 A (480 K)	(-)
20.1.	-	10 min 215 °C, 1060 °C sample RT	-	15 min 1.7 A (460K)	(c)
26.1.	5 min HATCN 215 °C 1.7 A (460 K)	8 min 217 °C, 1050 °C 1.7 A (460 K)	4 min Fe 1050 °C 1.8 A (480 K)	15 min 1.8 A (480 K)	(d)
4.2.	-	10 min 217 °C, 1060 °C 2.0 A (530 K)	-	10 min 2.0 A (530 K)	≈(c)
9.2.	-	9 min 218 °C, 1.9 nA 1.8 A (480 K)	-	-	(e)

molecular self-assembly. Sequential deposition has been shown to work for a range of organic molecules on different surfaces [15, 16, 34, 39, 74]. Hence, naturally, this was the first to be tried for our system. However, the sequential deposition was not successful for

the HATCN molecule and Fe atoms and no clear indication of MOF formation was found. The next strategy then was to deposit molecules and metal atoms simultaneously. That is also reported to lead to MOF formation [18, 20, 75]. Those trials however also were unsuccessful for our chosen systems of HATCN with Fe, or Ni atoms. Lastly, a certain combination of both sequential and simultaneous depositions was tested (see 2.1, 26.1.). And despite a change in the results, which will be more discussed in following text, not even this strategy led to a clear MOF formation.

As already mentioned, an elevated temperature of the sample is often needed in order to supply activation energy to the system, i.e. to increase the mobility of molecules on the surface and to limit its residence time [18]. However, no major change was observed for the recipes with heated sample. It has been reported, that HATCN do not follow the typical behavior of organic molecules – no desorption (of intact molecules or fragments) was observed at elevated temperatures. At the same time, the molecules are influenced by the temperature as Frank et al. also reported that the superstructure is destroyed, and termed the proposed rearrangement or chemical change of HATCN as a possible explanation. Our experiments showed also a disappearance of the honeycomb superlattice above roughly 550 K, thus the sample was held at temperatures below that threshold in our trials.

First, the grown structures were analyzed by LEEM. We present in Fig. 2.4a the bright field and observed mesoscale morphology for three different trials. Corresponding recipes can be found in Tab.2.1 based on the orange description in the images. Middle

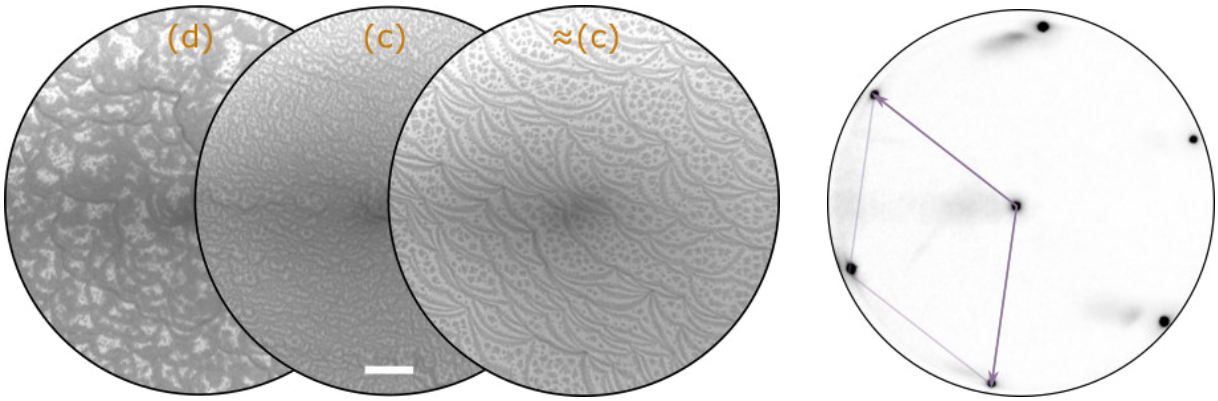

(a) (b)

Figure 2.4: LEEM analysis of HATCN and Fe deposition on the Ag(111) substrate. (a) In bright field, despite the overall low contrast, atomic terraces and grown structures appear as darker areas. The orange description refers to the respective recipe for growth accordingly to Tab.2.1. (b) Diffraction pattern with unit cell of hexagonal surface symmetry. Parameters: 5 eV, 4A, and 30 eV, 4A, respectively. The white scale bar indicates a unit of 1 μm in length.

and right bright fields (orange description (c) and ≈(c)) are images of the surface after co-deposition. The contrast is overall low, but there are dark lines and patches. When the right bright field is compared with the one from the clean surface, see Fig.1.8b, dark lines seem to correspond to the wreath of step edges with adsorbates which seem to cluster into islands also on the terraces. We can observe the same for the middle bright field image, although to rightly evaluate the image, one needs to know that the silver atomic steps were more frequent in this experiment, and terraces thus significantly smaller in size. The leftmost bright field (orange description (d)) differs in contrast which correlates

also with a bigger difference in the recipe of this trial. In this experiment the silver terraces can be again compared with the clean surface depicted in Fig. 1.8b and the atomic steps are here also dark lines. Dark areas are assumed to be here also grown structures, only the patches are larger and more coalescent. These formed islands are assumed to be metal-organic structures, however, long-range ordered frameworks were not achieved. The absence of long-range order manifests in the diffraction pattern, where only intensity points of the Ag(111) lattice are present without any superlattice points visible, see Fig. 2.4b. Therefore, our trials of MOF formation lead to the growth of structures, but without any observable order at the mesoscale.

Futher, XPS measurement were performed to confirm chemical composition and disclose expected shifts of peaks due to possible different bonding. Spectra in regions C 1s,

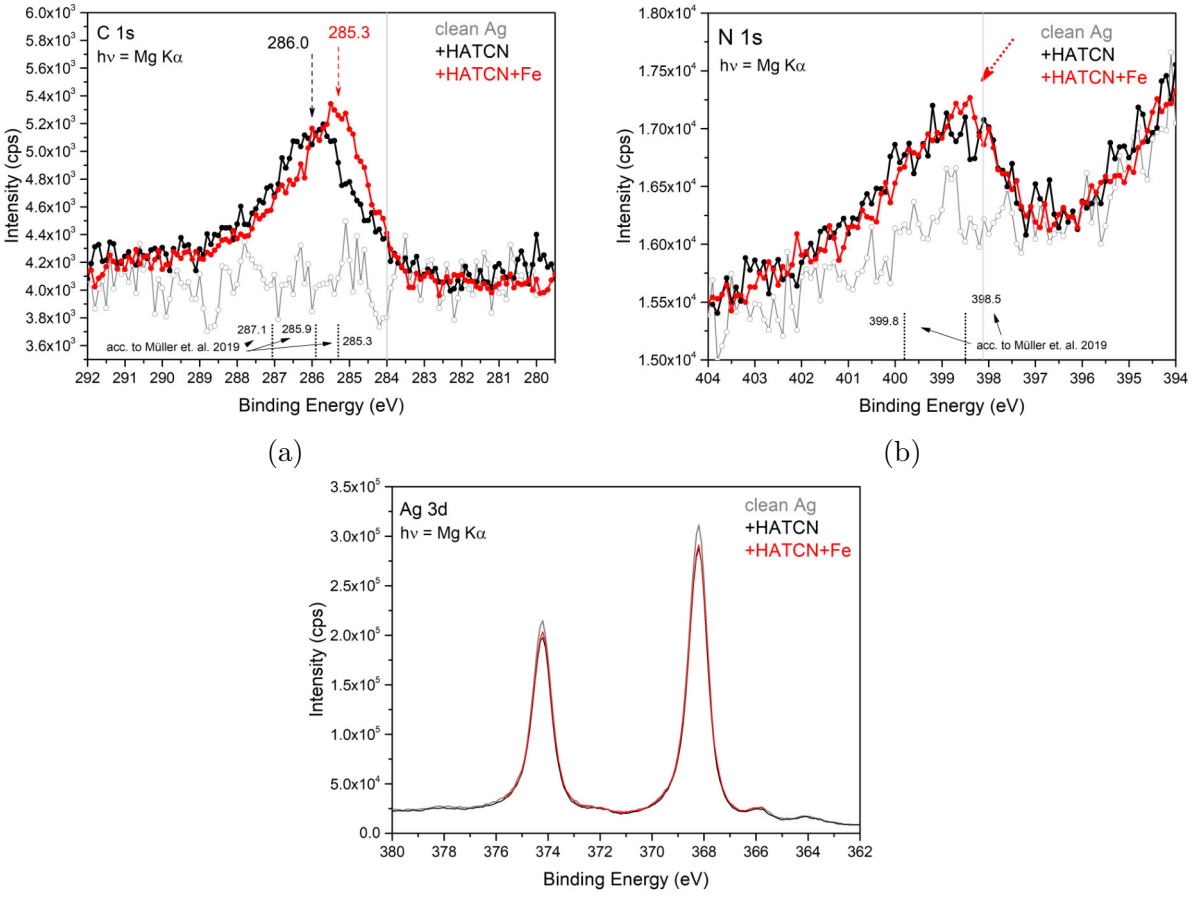

Figure 2.5: XPS spectra in (a) C 1s region, (b) N 1s region, and (c) Ag 3d region, which is noted in the left upper corner of graphics together with the type of source. The colour legend is in the right upper corner, +HATCN stands for 10 minute of HATCN deposition, +HATCN+Fe stands for co-deposition of HATCN and Fe, which respective recipe see in Tab. 2.1 row of 26.1. The C 1s and N 1s black peaks (+HATCN) can be fitted by three and two peaks due to three and two types of bonding, respectively. The values in the bottom part of (a,b) spectra are central positions of fitted peaks taken from literature [76]. Numbers are for C 1s 287.1, 285.9, 285.3 eV, and for N 1s 399.8, 395.5 eV. Red and black arrows in (a) represent the central position of measured peaks, and the red arrow in (b) points out a slight difference between red and black spectra.

N 1s, and Ag 3d are presented in Fig. 2.5 (a−c), respectively. The presence of a peak in the C 1s and N 1s region originates from the adsorbed molecules as one HATCN molecule contains eighteen carbon atoms and twelve nitrogen atoms. The peaks Ag $3d_{3/2}$ and Ag $3d_{5/2}$ in (c) correspond to the first few layers of the Ag(111) substrate. Therein, the spectra show a decrease in intensity after the deposition of HATCN and the co-deposition of HATCN and Fe. This correlates with results from LEEM, where the Ag(111) surface is seen to be covered by nearly a monolayer in the case of HATCN (see Fig. 2.1a) and almost fully covered also in the case of co-deposition of HATCN+Fe (see Fig. 2.4a, orange description (d)). Tabular values for C 1s and N 1s are marked by grey vertical lines. As described in theory Sec. 1.3.3, the shift from the tabular value gives us information about a change in bonding of the respective elements. The spectra visualized in black correspond to the molecular self-assembly of HATCN molecules. HATCN consists of three types of differently bonded carbon atoms – two types in backbone core and one in the cyano functional groups – and two types of nitrogen atoms – one in bipyridine side groups of the backbone core and the other in the cyano functional groups. The peaks C 1s and N 1s can be thus fitted by three and two peaks, respectively, and central positions of fitted peaks taken from the literature [76] are marked at the bottom of (a,b).

The red spectra in Fig. 2.5 correspond to the structure formed by co-deposition of HATCN and Fe. The red C 1s peak is shifted to the lower binding energy with respect to the black one by roughly 0.7 eV. One could expect that it reflects bonding of HATCN molecules with Fe atoms. However, no significant shift is visible for N 1s peak. There is only a small additional bump in the red spectra on the lower binding energies, highlighted by the red arrow in Fig. 2.5 (b). That could be explained by a little amount of molecules forming a coordination bond with the Fe metal atoms. The more significant shift in C 1s peak is not well understood yet and the explanation will be probably more complex. To sum up, the XPS spectra confirmed that the Ag(111) surface is covered after deposition and that it is covered by carbon and nitrogen atoms, which correlates with the deposition of HATCN molecules. After the introduction of Fe atoms, there is a significant visible change in C 1s peak, and a possible slight change in N 1s one. This might be explained by a coordination bond being formed between some molecules and metal atoms. Nevertheless, there is not enough evidence in the measured XPS data to confirm a formation of large-scale bonding between HATCN and Fe atoms and the full explanation of shifts might be more intricate.

Finally, the STM investigation reveals nanoscale details of the grown structures. In order to simplify the comparison, the image (a) in Fig. 2.6 corresponds to the honeycomb self-assembly of HATCN alone. The green inserted lines highlight the boundary regions between two domains of clockwise and counterclockwise bonding. The images (b−e) correspond to recipes described in Tab. 2.1, where the right-most column denotes to which recipe the image corresponds. First, the obtained structure after sequential deposition is displayed in Fig. 2.6 (b). If compared to the self-assembly of HATCN alone, the honeycomb structure partially remained (see pink ellipse in Fig. 2.6 (b)), the continuous layer is destroyed however. In between the remaining patches of honeycomb, there are structures without order. That might be randomly arranged molecules or molecules bound to the metal atoms in an unordered way. Any obvious coordination between the HATCN and the Fe atoms is not visible on this scale, and a better resolution image was not reached. The protrusions of overly bright contrast are assumed to be iron atoms clustering due to annealing.

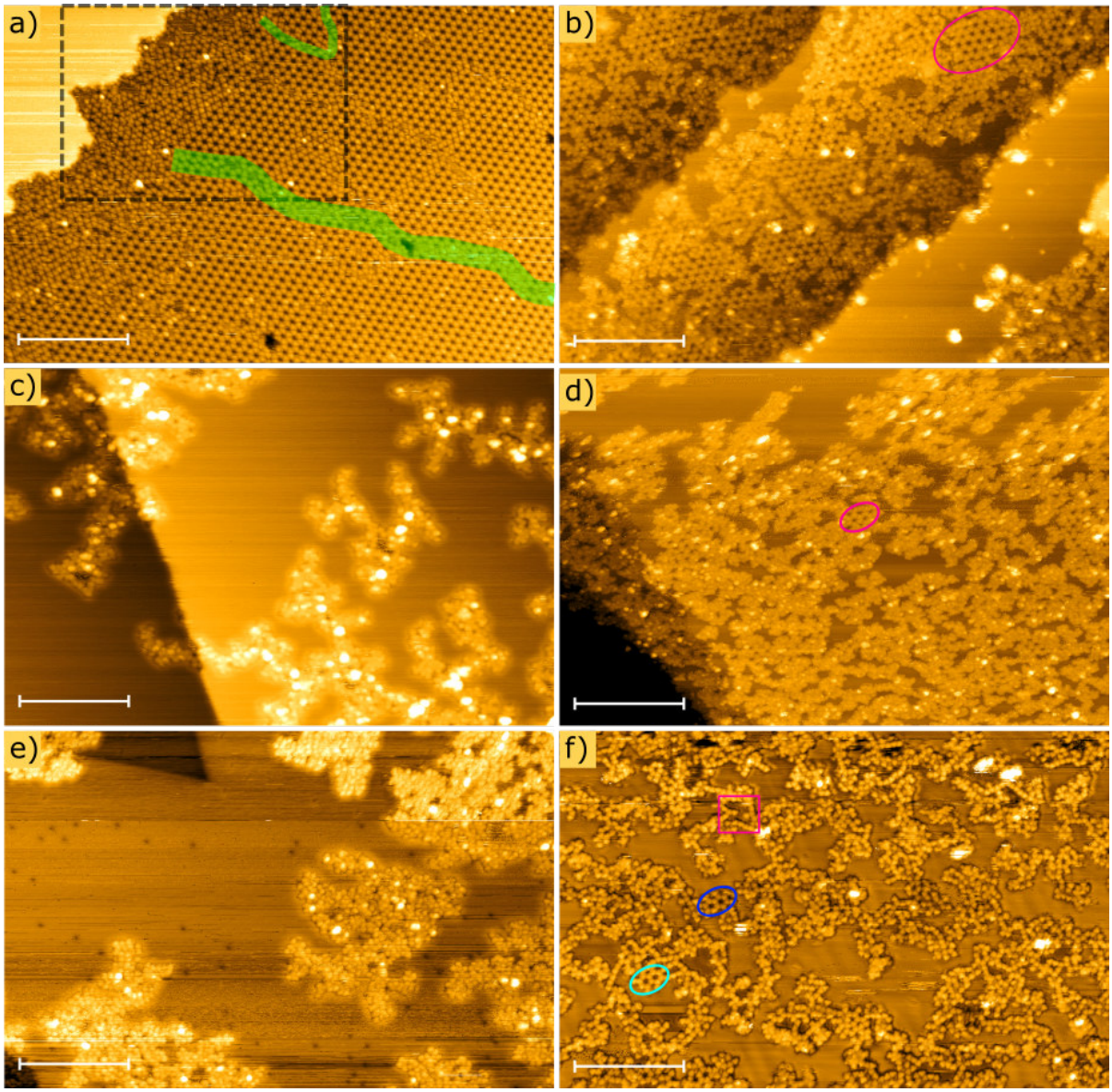

Figure 2.6: STM images of (a) HATCN self-assembly, (b−d) metal-organic structures based on HATCN and Fe, or (e) Ni atoms on Ag(111) surface, (f) based on HATCN and Fe atoms on Au(111) surface. (a) dashed rectangular detial part is shown separately in Fig. 2.3a, (c−d) images corresponds to deposition recipes described in Fig. 2.1. Parameters: (a) 51 pA, 2.6 mV (b) 50 pA, 2.6 mV (c) 30 pA, 2.8 mV (d) 50 pA, −2.1 mV (e) 40 pA, 1.2 mV (f) 70 pA, 1.2 mV, current, bias, respectively. The white scale bar indicates a unit of 20 nm in length. Images processed in Gwyddion.

Then, the resulting structures of co-deposition trials are depicted in Fig. 2.6 (c) for Fe metal atoms and in (e) for Ni metal atoms used. In Tab. 2.1, there is one recipe labelled as ≈(c). That means that for this recipe we observed very similar results in STM as in the presented (c) image. In cases of Fe as well as for Ni, there are islands of structures apparently consisting of bright triangular protrusions, assumed to be molecules, and overly bright protrusions, assumed to be again clusters of metal atoms. Due to the specific shape of the islands, we suggest a dendrite growth mode. This might be caused by the introduction of metal atoms and their interaction with molecules. However, no

long-range order was observed in either of the trials. And, here also, a better resolution was not reached, the STP tip was in general very unstable while measuring the grown metal-organic structures.
Lastly, the combination of both approaches, sequential and simultaneous depositions, combines also both structures already seen in (b) and (c,e). As can be seen in Fig. 2.6 (d), the surface is covered mostly with islands of dendrite shape. Unlike in co-deposition trials, islands here coalesce, although this difference might be caused only by different deposition times and thus coverage. In addition, also few patches of a honeycomb-like structure are present in between, as highlighted by a pink ellipse in Fig. 2.6 (d).

Furthermore, the (f) sub-figure in Fig. 2.6 shows the Au(111) surface after sequential deposition of HATCN (6 min at 210 °C) and Fe (40 min at 1010 °C) at RT, and subsequent annealing (15 min 1.7 A (450 K)). Despite the high mobility of HATCN on Au(111) alone at RT, after the introduction of metal atoms, the mobility seems to decrease. The molecules now form a random arrangement. Chains of linear-like structures can be recognized, as seen in the area of the pink rectangle, and also few double rings of honeycomb-like structure can be found, as highlighted by coloured ellipses. In the latter, both clockwise (blue) and counterclockwise (cyan) bonding is formed. Despite there seems to be some repeating bonding scheme in the formed structure, no long-range order was found.

Altogether, both sequential depositions and co-depositions most probably led to the formation of metal-organic coordination. However, no long-range order was observed. Sequential deposition led to partially hindered HATCN self-assembly, whereas co-deposition created directly disordered islands of dendrite-grown structures on the terraces of the substrate for both Fe and Ni being deposited as metal coordination centers. The combination of both approaches, co-deposition with preceding HATCN deposition, combines also both structures already imaged in STM. Sequential deposition on Au(111) surface led to lower mobility of HATCN and the formation of randomly assembled molecules but without instead forming metal-organic frameworks.

Although HATCN molecules self-assemble into molecular periodic arrays, metal atoms incorporate into this structure in non-periodic way. Therefore, no long-range order framework is formed. A few factors might be the cause for that. First, two different bonding schemes between ligands and metal atoms are possible. We expected a bonding via the carbonitrile group which could have led to a hexagonal lattice. Second, a strong bidentate chelating coordination, is available, which is dominating in the case of the HAT ligand [34]. Yet, the HATCN ligand precludes bonding with more than one HATCN molecules just out of geometric reasons of the molecule, i.e. steric hinderance, and because of the carbonitrile groups.

Furthermore, compared to the molecule HITP [39, 40, 41], the nitrogen atoms in carbonitrile groups of HATCN are apart from the central backbone structure. That make the square-planar coordination of metal atoms with four N atoms (depicted as black square) most probably impossible due to the length of the bond in the expected honeycomb geometry. For further explanation of the problematic bonding an approximate model is presented in Fig. 2.7. To preserve the length of the bond, nitrogen atoms, and thus two neighboring HATCN molecules, would need to be closer to each other (as seen in left panel of Fig. 2.7), which is problematic for multiple reasons. First, the nitrogen atoms would repel each other at that point probably. Then, the structures of coordination frameworks reflect ligand and metal coordination geometries and any existing geometry matches with the imagined resulting coordination (depicted as pink rectangle). The metal

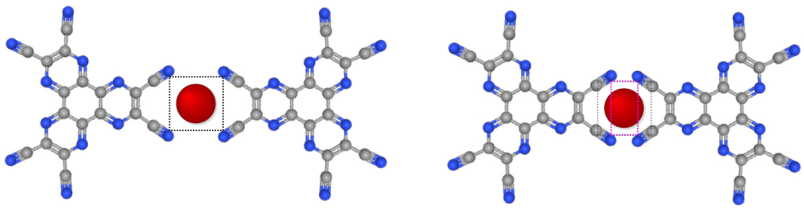

Figure 2.7: Model of possible problematic in HATCN coordination bonding that was expected to take place in MOF. Bonding distances are only approximate. Ball-and-stick model taken from [31].

center can be still bounded to one of the cyano groups, however. But this then precludes the formation of a periodic array, despite the possibility of bounding to more than one molecule.

To sum up, a HATCN metal-organic structure was achieved. Nonetheless, no long-range periodic order could be obtained. On the account of generating a recipe for a MOF formation to the Bi_2Se_3 substrate being our goal, we studied HATCN self-assembly on Bi_2Se_3 as well. This will be described in the next chapter, in Sec. 3.2.1. But as we found no periodic order on coinage metals for the metal-organic framework formation, there is no recipe to be transferred. Therefore, our further investigation reoriented to another carbonitrile molecule, specifically DCA.

2.3. DCA molecules on Ag(111) surface

Molecule DCA has already been reported to create MOFs on coinage metal surfaces [46, 48, 49], as well as on weakly interacting substrates, e.g. Gr/Ir(111) [16, 52], $NbSe_2$ [47]. Since a recipe of preparation recipe changes from chamber to chamber, and thus series of experiments were needed in order to calibrate the correct deposition parameters of depositions. Up to date, only STM investigation of such layers has been performed. In this thesis, we also focused on the mesoscale measurements and using a LEEM microscope that allowed us to map the morphology and reciprocal space. This part thus focuses on the adsorption and phase formation of DCA molecules and DCA-based MOFs formation on a clean surface of Ag(111).

2.3.1. Adsorption and phase formation of DCA

In literature, the deposition experiments of DCA molecules have been performed and reported at different temperatures – 60 °C, 80 °C, 100 °C, and 120 °C. Therefore, we first decided to try evaporation temperatures up to 100°C and check the achieved coverage by LEEM. Whereas the molecular flux at 60 °C led to slow growth of molecular islands, at 100 °C it led to a very fast increase of back-pressure. The Fig. 2.8a shows a LEEM bright field image of the Ag(111) surface after a deposition of DCA molecules for 15 min at 80 °C. At 12 eV, molecular islands appear as brighter areas, whereas darker areas are the Ag(111) substrate (see Fig. 2.8a), and fill the silver terraces in the course of the growth. However, unlike in the case of HATCN, DCA islands are very sensitive to e-beam irradiation, which makes the calibration process, as described earlier, more tedious.

Within a few seconds, the decomposition of molecular islands started – the islands fragment into smaller ones and finally disappear completely in less than a minute. The illustrative example of both effects shows Fig. 2.8 (a−c) in the area of yellow marked circle. The leftmost subplot is a bright field image after a 3 s of exposure, while the rightmost after 30 s. The middle one is a color-coded composition of dark field images measured in the meantime (color coding will be explained later in this section). The yellow circle Fig. 2.8a shows an area with a compact DCA island at the beginning of its irradiation. While measuring in dark field mode with a little delay, the island already disintegrated into three smaller ones, out of which two had already moved a bit further away from the central one. With a longer delay, the small islands moved again and shrunk as imaged in Fig. 2.8c.

Despite the disappearance of molecular islands, initially displayed as bright areas in Fig. 2.8a, the areas of the original islands remain different in contrast, see Fig. 2.8c. The intensity of islands is now lower and the points in the diffraction pattern corresponding to the molecular superlattice fainted. Thus, none of the colored points in model in Fig. 2.8e appears in pattern now, only Ag(111) lattice points are observed. A possible explanation is the chemical decomposition of molecules under the beam, resulting in decomposed parts of molecules covering the surface without any order. In addition, after an even longer exposition, also initially uncovered silver terraces become different in contrast. This is probably related to the higher concentration of molecular gas after islands decomposition.

In summary, all details mentioned above make the calibration of a monolayer coverage complicated. Furthermore, the deposition of DCA molecules creates a significant background pressure in the deposition chamber. Consequently, some amount of DCA

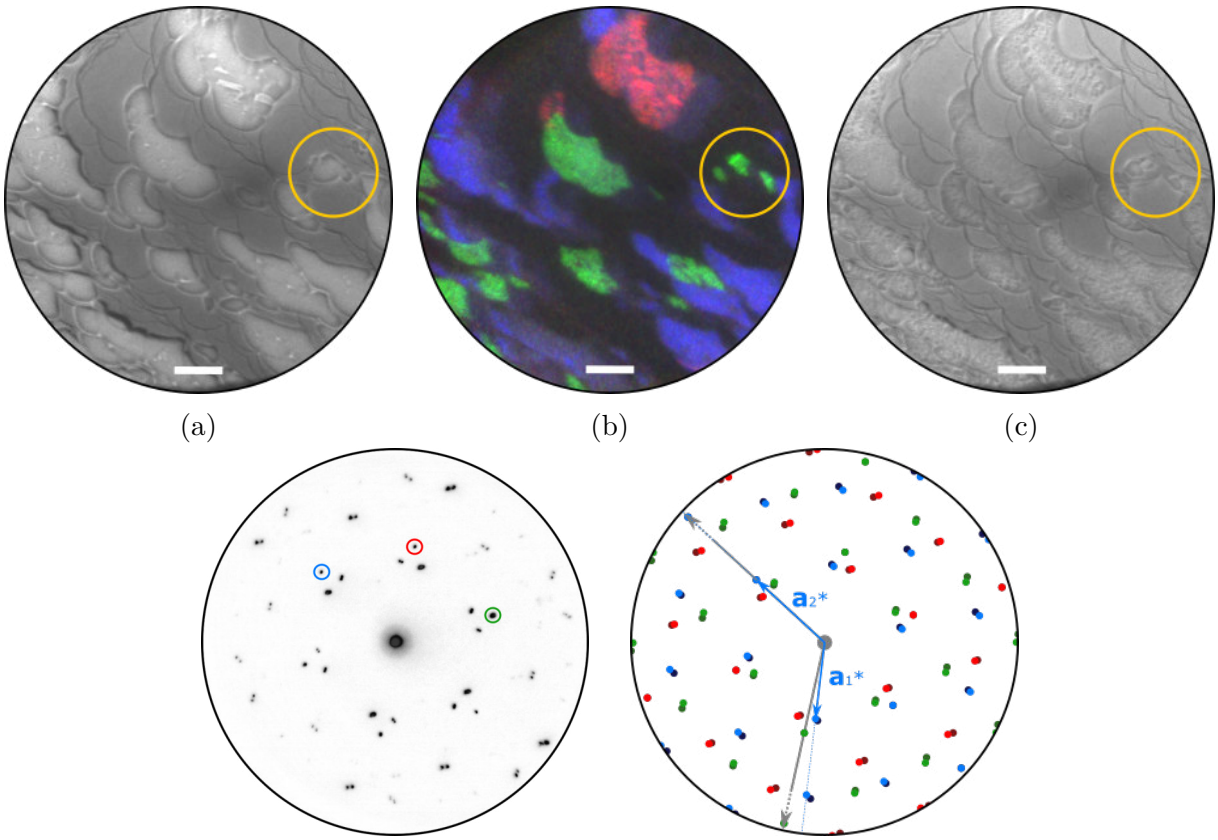

Figure 2.8: LEEM analysis of DCA molecules on Ag(111) substrate. (a) Bright field immediately after exposition to beam. Bright areas represent the molecular islands. (b) Color coded dark field composition of the same area measured during the e-beam exposure (5−25 s) using spots highlighted in (d). (c) Bright field image of the same area measured after 30 s of exposure – visible disintegration of molecular islands, change in contrast. Yellow details highlight the area where both effects are displayed – disintegration, and high mobility. (d) Diffraction pattern from a large area containing all domains of self-assembly with (e) the model, made using ProLEED Studio software in testing phase, based on unit cell parameters $\mathbf{a_1}$, $\mathbf{a_2}$ taken from [42]. Parameters: (a−c) 12 eV, 5A and (d) 12 eV, 1A. The white scale bar indicates a unit of 1 μm in length.

molecules are deposited in addition even during the subsequent deposition of Fe atoms. Even though growth of a monolayer coverage was not optimized in the end, a series of experiments resulted in settling for 15 min long deposition at 80 °C, which was just shown in LEEM results. The surface is covered by roughly 50 % with molecular islands of size in the order of few μm as seen in Fig. 2.8a. Moreover, the corresponding flux of molecules causes only a slow increase in the background pressure.

The diffraction pattern in Fig. 2.8d measured the same sample indicates the presence of different molecular domains. To clarify the presence of individual domains, we made a diffraction pattern model, using ProLEED Studio software in testing phase, based on unit cell vectors of Kumar et al. denoted as $\mathbf{a_1}$, $\mathbf{a_2}$ [42]. The modeled pattern with highlighted unit cell vectors is shown in Fig. 2.8e, and matches well the measured data. DCA molecules occupy surface sites so that the vector $\mathbf{a_1}$ is aligned with one of the substrate's $\langle 110 \rangle$ directions. Due to the substrate six-fold and DCA superlattice symmetry, there

are altogether six different domains. Those correspond to six colours in the model of the diffraction pattern in Fig. 2.8e.

As a result of the geometrical arrangement of DCA molecules in real space, there are only subtle angular differences between certain domains in reciprocal space. Especially in the proximity of the zero point of the diffraction pattern, where points mostly overlap. Consequently, we see apparent double spots seen in diffraction pattern in Fig. 2.8d. Although, all six domains might be imaged separately in micro-diffraction mode, only three different patterns were found among measured data. In the modeled pattern (Fig. 2.8e), hardly distinguishable domains are marked with two shades of the same colour. Due to the proximity of spots in the diffraction pattern, it was not possible to measure separate dark field images associated with these spots. Therefore, only three different ones were imaged using spots highlighted in Fig. 2.8d. An image of all dark fields, already processed, coloured, and merged into one, is shown in Fig. 2.8b.

Going from mesoscale to nanoscale, it has been shown that DCA adopts a planar adsorption configuration on Ag(111) [42]. Molecules self-assemble into a 2D monoclinic lattice with unit cell vectors $\mathbf{a_1} = (1.20 \pm 0.02)\,\mathrm{nm}$ and $\mathbf{a_2} = (0.99 \pm 0.01)\,\mathrm{nm}$ with in-between angle $\measuredangle(\mathbf{a_1}, \mathbf{a_2}) = (53 \pm 1)^\circ$ (see Fig. 2.9 (a), reprinted). In view of having lone electron pairs, the two-fold symmetric carbonitrile groups mediate directional hydrogen bonding, resulting in in-plane noncovalent networking. Kumar et al. show that such intermolecular bonding makes the molecular axis – along the anthracene group, displayed as a yellow dashed line – follow a $(5 \pm 1)^\circ$ angle with respect to $\mathbf{a_1}$, which causes a slight shift of lattice (see Fig. 2.9 (a) for details).

In an STM image, DCA molecules appear as bright protrusions (Fig. 2.9 (c) $-0.6\,\mathrm{V}$) with homogeneous contrast within one domain. This is true only up until a certain bias voltage. Kumar et al. observed a very significant bias-dependent reduction of the apparent height in STM. As is visible for different negative bias voltages (see Fig. 2.9 (c) -2.4, -2.6, $-3.0\,\mathrm{V}$) more and more molecules switch their appearance from bright to dark protrusion and so generate a new overlying periodicity. They found the cause to be a spatially periodic surface-to-molecule electron transfer and negative charging of individual DCA molecules induced by the local electric field at the STM junction [42]. They showed that the bias voltage needed to induce this change, in contrast, varies periodically within the molecular layer and is commensurate with the underlying Ag(111) atomic lattice. They explain this with small site-dependent variations of the molecule–surface distance measured by low-temperature tip-functionalized noncontact AFM (nc-AFM). In other words, two DCA molecules with the same adsorption site will exhibit the same bias-dependent change in STM imaging contrast. [42]

This subtle real-space long-range modulation of molecular apparent height is correlated with the mismatch of the substrate lattice and the molecular superlattice. By the nc-AFM measurement analysis, they found that the DCA molecules sit on the same site over the Ag(111) surface with a periodicity of 50 molecules in the $\langle 110 \rangle$ direction. The change in molecular STM imaging contrast observed at negative biases (see Fig. 2.9, (c)) depends on the adsorption site of molecules. Therefore, lower frequency peaks are present in the Fourier transform (FT) of the STM and the nc-AFM (the latter see in Fig. 2.9 (b)) forming a moiré pattern.

Going back to the already mentioned micro-diffraction measurement, in Fig. 2.10 (a–c) three micro-diffraction patterns of individual DCA domains are shown. They correspond to the green, red, and blue coloring in the diffraction pattern of Fig. 2.8e. Although

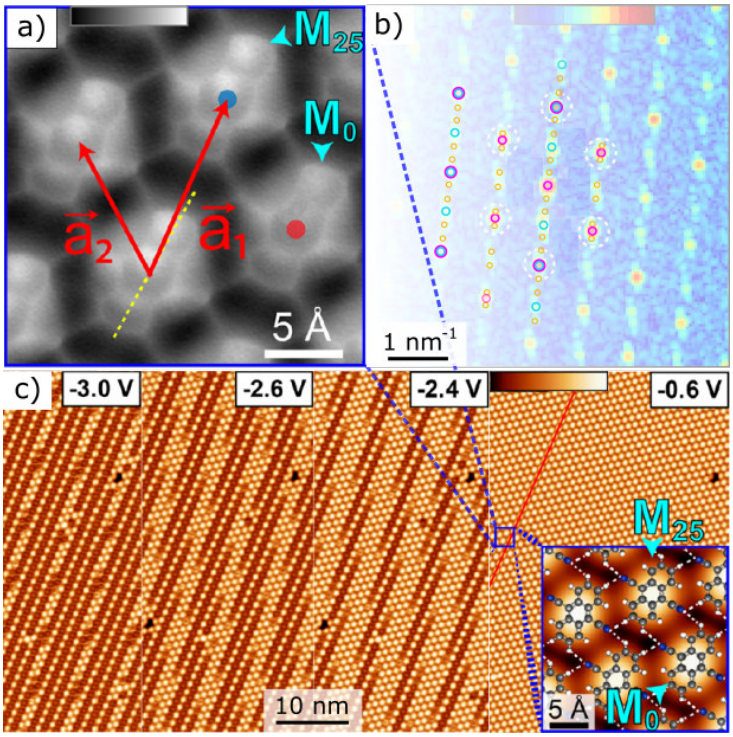

Figure 2.9: Self-assembly of DCA on Ag(111). (a) Four molecules imaged by CO-tip-functionalized nc-AFM. The red unit cell vectors are $\mathbf{a_1} = (1.20 \pm 0.02)\,\mathrm{nm}$ and $\mathbf{a_2} = (0.99 \pm 0.01)\,\mathrm{nm}$ with in-between angle $\measuredangle(\mathbf{a_1}, \mathbf{a_2}) = (53 \pm 1)°$. Long molecular axis (yellow dashed line) forms a 5° angle with the vector $\mathbf{a_1}$. (b) Fourier transform of a large scale of nc-AFM image, superimposed with a model of diffraction pattern from Fig. 2.10. (c) Constant-current STM images at bias voltages $-0.6\,\mathrm{V}$, $-2.4\,\mathrm{V}$, $-2.6\,\mathrm{V}$ and $-3.0\,\mathrm{V}$ ($I_t = 50\,\mathrm{pA}$). At bias $-0.6\,\mathrm{V}$, the molecular domain appears homogeneous; each bright protrusions is a DCA molecule. As bias decreases, some molecules are imaged darker (partial change in contrast from right to left), with a smaller apparent height. defining a periodic superstructure. The number of dark molecules increases with the increasing absolute value of bias. Images taken and adapted from [42].

compared to a single domain of the model, more points are present in the measured micro-diffraction patterns. As that model is based on unit cell vectors, only the periodicity of the superlattice is displayed. In order to explain higher order periodicities, modeled patterns were inserted in subfigures (a−c) and together replotted in (d−f) of Fig. 2.10.

The first pattern, see (a, d), can be described by points of cyan and yellow colour. Yellow points are very dense along the $\mathbf{a_2}^*$ reciprocal vector and its periodicity is portrayed by a simple black grid. Second (b,e) can be described by points of cyan and green colour. Green points are also more dense along the $\mathbf{a_2}^*$ reciprocal vector, however, the black grid shows a more complex periodicity in this case. Cyan points are higher in intensity and overlap with certain ones of the yellow/green colour. Their periodicity is visualized by cyan vectors. In the last, third, pattern (c) the cyan points can be found, however, the higher periodicity of non-lattice points in between is smeared into lines. The last model (f) was thus generated by combining the yellow and the green ones. The high density of both along $\mathbf{a_2}^*$ resulted in the clustering of yellow and green points in the form of short lines along the same direction. We propose a hypothesis that the smearing can be explained by the superposition and thus that there are two different periodicities of higher order in (c)

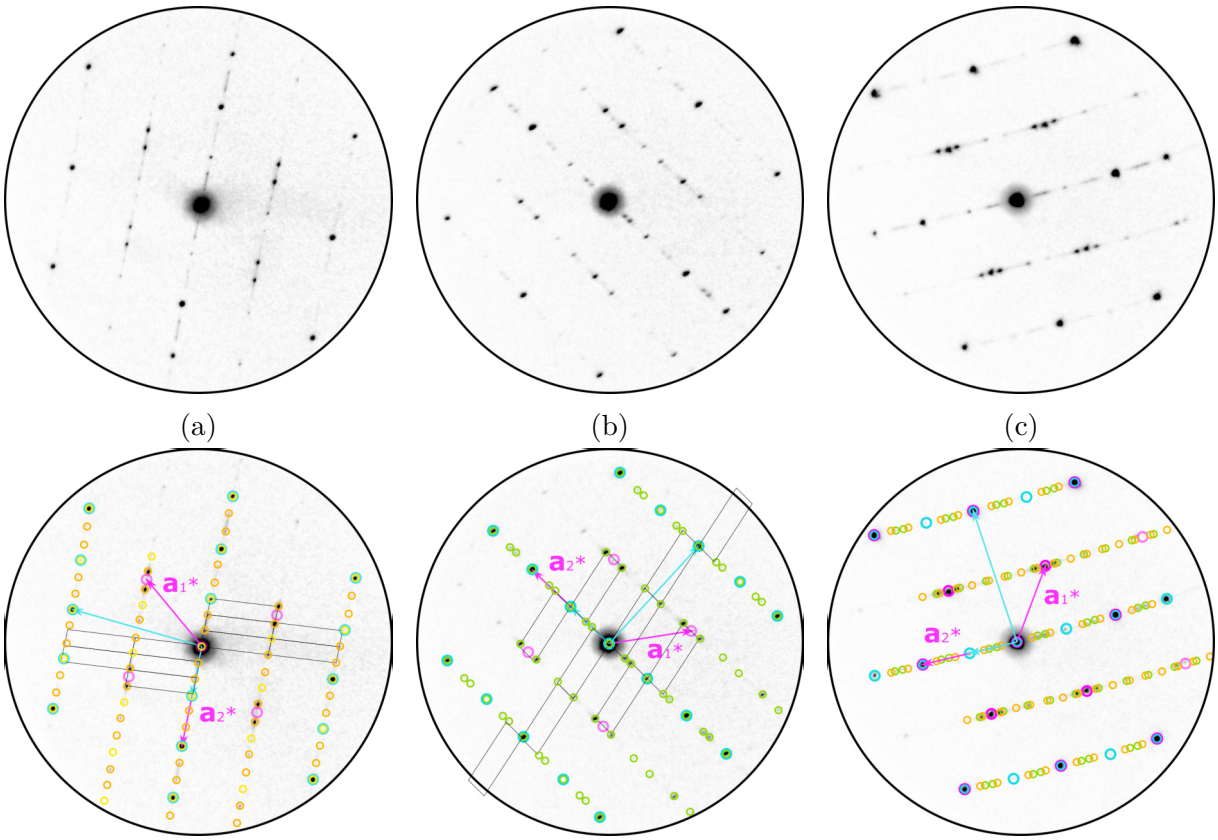

Figure 2.10: Micro-diffraction measurements of DCA self-assembled on Ag(111) surface imaged by LEEM. (a−c) Measured micro-diffractions of three domains corresponding to both shades of green, red, and blue spots of the model in Fig. 2.8e, respectively. Another three domains are indiscernible. (d−f) Identical images with inserted models of diffraction pattern. Pink points and vectors $\mathbf{a_1}$ and $\mathbf{a_2}$ corresponds to diffraction points of the superlattice. The cyan and yellow/green are points of higher symmetry deduced from measured patterns. Cyan vectors portray periodicity of the cyan points. The black grid portrays the periodicity of the yellow and green diffraction points in (d) and (e), respectively. Parameters: 12 eV, 3A.

pattern. Although, as there are still gaps in the model, the lines might be a superposition of more than two periodicities, which might be just not measured individually yet. If one is careful, it can be observed that the spots of DCA domains (thus the one defines by $\mathbf{a_1}^*$ and $\mathbf{a_2}^*$), coloured in pink, appear only in (c). In the pattern (a) and (b) this periodicity is fainted.

No reciprocal space measurements have been reported up to now. However, Kumar et al. provide a Furrier transform (FT) from a large-scale nc-AFM image [42]. When reciprocal spaces are compared, one of the models from Fig. 2.10 matches to some extent the FT image. It is the model with yellow points shown in (d) and is also superimposed over the FT results in Fig. 2.9 (b). The points of higher order in FT reflect the behavior of DCA on Ag(111). The DCA molecules occupy the same site on the surface with a certain periodicity, moreover, the site-dependent charging was found to generate a new overlying periodicity. The match between patterns suggests that both effects might be present also in LEEM measurements. The bright field study 2.8 (a−c) already showed

that the electron beam highly influences the behavior of molecular islands on the surface. This influence is immediate and can have an effect on measured results. The electron beam might be a source of charging of the molecular layer with the analogous effect as STM biased tip visualized with the STM bias dependence observation in literature.

The slight mismatch in details of FT and the model based on micro-diffraction can originate from two effects, which do not refute mentioned possible analogy. First, the physical principles of the used techniques differ, which comes with different distortion mechanisms. For instance, the use of electron optics influences the resulting image in LEEM, whereas thermal drift or nonlinearities of piezoelectric actuators cause distortion in STM imagining. Second, different conditions of experiments might induce a mismatch of results. Kumar et al. investigated samples cooled at low temperatures (4.3 K, [42]), meanwhile, samples of room temperature were measured in LEEM.

In spite of observed disintegration in bright fields, the micro-diffraction measurements do not confirm that behavior. Fading of the pattern as a whole was rather slow, and fading/appearance of individual points in the pattern seemed to be place-dependent, not time-dependent. On the other hand, the aperture needed for the micro-diffraction experiment restricts the beam, therefore, the intensity of exposition is reduced significantly. Furthermore, another experiment was performed in which deposition led to multilayer of DCA. Here, the measured diffraction pattern was a lot simpler. Only points of pink and cyan periodicity were observed, in between non-lattice points were missing. As the charging effect is based on surface-to-molecule electron transfer and is dependent on the site of molecule on the Ag(111) substrate, it is observable only in submonolayer coverage. Therefore, the non-lattice (yellow/green) points might reflect the periodicity of the site dependency and the charging effect.

In summary, the behavior of DCA self-assembly on Ag(111) is a complex topic by itself and would need considerably more time and investigation to be fully understood. As that is not the aim of this work, the bottom line from our investigation is that the diffraction of lattice points matches with those from Kumar et al. [42]. Hence, the molecules self-assemble into the same structure even at RT, although with higher mobility. Another point to be taken is the significant similarity in points of higher order between our models based on measured patterns and their FT of nc-AFM measurement. We are explaining this similarity by the fact, that the electron beam might be charging the molecular submonolayer in an analogously site-dependent way as with the STM tip.

2.3.2. Metal-organic frameworks with DCA

Although DCA has been already shown to form MOFs, a combination of DCA, Fe atoms and the Ag(111) surface has not been reported yet. Thus, a recipe of a DCA framework creation on Gr/Ir(111) surface has been taken from Kumar et al [16] and successfully tailored to coinage metal surface. The sequential deposition of DCA and metal atoms is sufficient for the formation of MOFs, which exhibits long-range order. Thus, the final recipe consist of 15 min long DCA deposition at 80 °C, and subsequent 30 min of Fe at 1030 °C.

The analysis of the grown metal-organic structure was performed in LEEM. In the bright field, there are dark islands of multiple sizes partially filling the Ag(111) terraces, see Fig. 2.11a. Large dark islands often adjoin the step-edge and are of size up to 0.5 μm. The complex diffraction pattern displayed in 2.11d, showing superlattice symmetry, proves

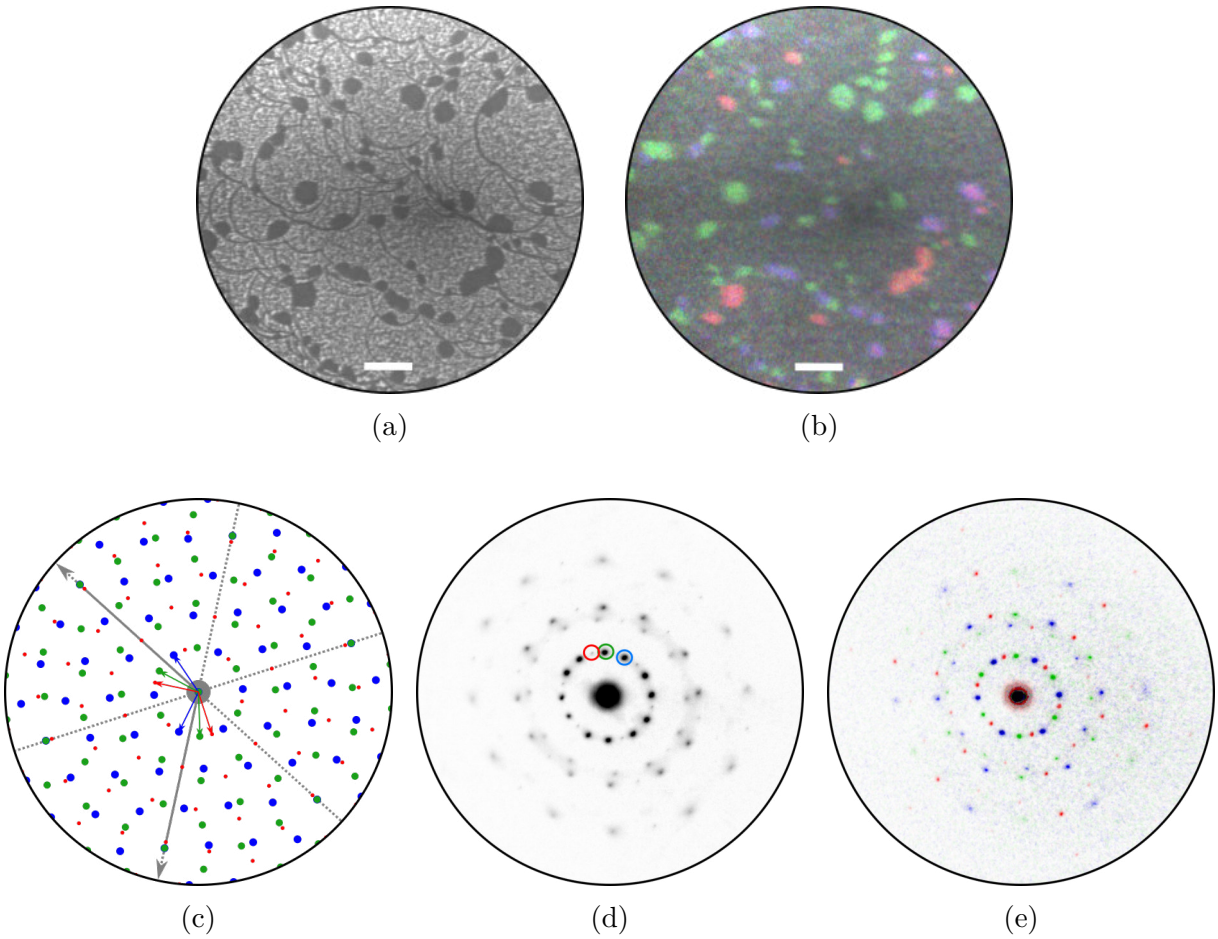

Figure 2.11: LEEM analysis of DCA-Fe MOFs formed on Ag(111) substrate. (a) Bright field, the dark areas and lines corresponds to islands of the MOF and atomic steps of Ag(111), respectively. (b) Color coded dark field composition of the same area measurement using spots highlighted in (d). (c) Model of the diffraction pattern, made using ProLEED Studio software in testing phase, based on the unit cell vector taken from [16] and on further analysis of measured micro-diffractions. (d) Measured diffraction pattern from a large area containing all domains and (e) micro-diffraction images coloured and merged into a composition. Parameters: (a,b) 14 eV, 5A, (d-e) 14 eV, 1A. The white scale bar indicates a unit of 1 μm in length.

that a framework of long-range order was achieved. Furthermore, the dark field measurement shows (see Fig. 2.11b) that the dark areas in the bright field corresponds to MOF structure as it matches with the colored islands of different domains. Elsewhere on the terraces, the contrast in bright field is variable, seemingly grainy. That might corresponds to islands very small in size, however, this prediction is neither confirmed nor denied as that is probably beyond the resolution abilities of dark field mode. Besides, it has been reported that subsequent annealing should increase the domain size of formed MOFs for DCA with Fe Gr/Ir(111) [16]. This is not the case for our system though. Annealing led to a breach of long-range order; the dark islands in the bright field expanded, but the diffraction pattern disappeared.

Different domains can be distinguished with the help of micro-diffraction mode. In Fig. 2.11e, three micro-diffraction images are processed, colored and merged into one. Each colour represents one measured domain and it also corresponds to colours in dark

field Fig. 2.11b which was imaged using spots highlighted in Fig. 2.11d. Altogether, combined domains create the same pattern as the measured one seen in Fig. 2.11d, which proves that there are only three domains of the MOF present on the surface. Focusing on just a single domain, MOF assembles into a structure with hexagonal symmetry. That is in accordance with observation on diverse substrates with the (111) surface termination, e.g. coinage metals [46, 49, 48], graphene [16, 52], van der Waals superconductor [47]. They observed that metal-organic framework structures combine a honeycomb lattice of metal centers with a kagome lattice of DCA molecules (see modeled structure in Fig.2.12). Based on unit cell vectors of Kumar et al. who investigated DCA-Co MOFs on Gr/Ir(111) [16], and further analysis of our measured data, a model of diffraction pattern was generated also using ProLEED Studio software in testing phase (see Fig. 2.11c). Red, blue, and green vectors define reciprocal unit cells of individual domains. As points corresponding to the substrate are further from the central point, inserted grey lines and vectors indicate only respective directions, and thus do not hold information about the size. Although the bonding distances in general differ for individual transitional metals and substrates, the model depicted in Fig. 2.11c matches well our measured data, i.e. DCA-Fe MOFs on the Ag(111) surface.

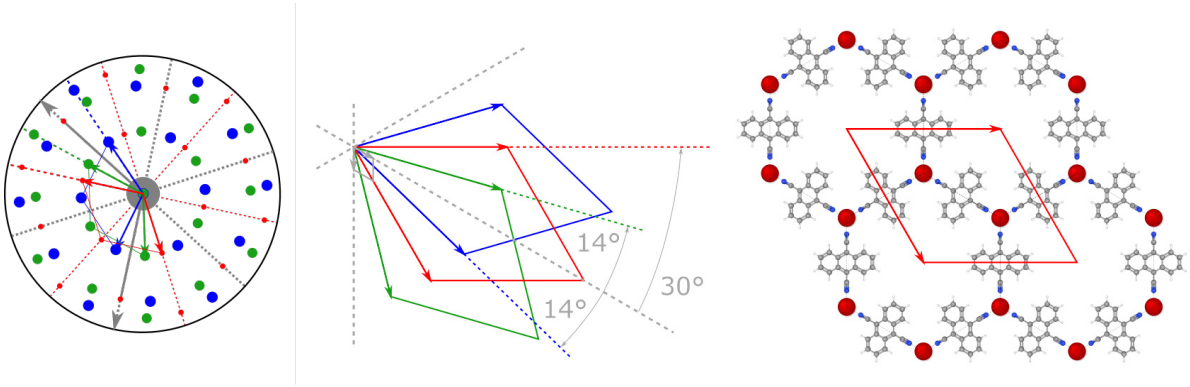

Figure 2.12: Models of MOF structure with DCA based on unit cell vectors of Kumar et al. investigating DCA-Co MOF formation. Left plot, detailed central part of diffraction model in Fig. 2.8e. Middle plot, DCA-Fe and Ag(111) unit cells of individual domains in red, blue, green and of Ag(111), respectively. Two orientations of DCA-Fe with respect to Ag(111) are present - rotated by 30°, red colour, and 14°, green, blue. Right plot, structure of DCA based metal-organic framework combining a honeycomb lattice of metal centers with a kagome lattice of DCA molecules. Red rhombus defines unit cell of the MOF structure. Ball-and-stick model of molecule taken from [31].

A detail of the central part of the model is depicted again in Fig. 2.12 (left). In order to explain better orientations of domains with respect to the substrate, also a model of real space unit cells is plotted in the middle. The right part of the figure then displays a model of the real space structure of metal-organic frameworks as reported in the literature. In the latter, the red rhombus defines the unit cell of the MOF structure in real space. Additional dashed lines in the left and middle plots represent the main directions of the hexagonal symmetry of the respective domains. One can see that the orientation of the red domain is rotated with respect to Ag(111) by 30°. Besides, the green domain was measured to be rotated by 14°. The same rotation is applied for blue, only in the other direction. The latter means those two domains are mirrored. Patterns with rotation 13° and 15° was also modeled to avoid possible measurement errors, e.g.

due to distortion, and neither matched with the measured pattern. Overall, as it clearly shows the middle plot in Fig. 2.12, there are two orientation of DCA+Fe superlattice with respect to the Ag(111) substrate lattice – with reciprocal unit cell vectors rotated by 30° (the red domaine), then by 14° (the blue and green domain). Due to the substrate six-fold, DCA+Fe superlattice symmetry and two possible orientations, there are altogether three different domains. Those correspond to three colours in the model of the diffraction pattern in Fig. 2.8e. Comparing a coloured diffraction pattern (Fig. 2.11c, or 2.11e) to the measured one in Fig. 2.11d, one can see the domain of red colour is lower in intensity. Therefore it can be concluded that the orientation rotated by 30° respectively to Ag(111) is remarkably less present on the surface than the other, rotated by 14°.

Further, like for HATCN, XPS measurements were performed to confirm the chemical composition and disclose expected shifts of peaks due to possible different bonding. Spectra in regions C 1s, N 1s, and Ag 3d are presented in Fig. 2.13 (a−c), respectively. The presence of a peak in the C 1s and N 1s region after deposition originates from DCA containing sixteen carbon atoms and two nitrogen atoms per molecule. The peaks of Ag $3d_{3/2}$ and Ag $3d_{5/2}$ in (c), also here, correspond to the first few layers of the Ag(111) substrate. Therein, the spectra show a significant decrease in intensity after the deposition of DCA and after subsequent Fe deposition, suggesting more than a monolayer of molecules in coverage. That does not correlate with results from LEEM, because the presented XPS data are from a different experiment with much higher coverage. In view of only two cyano functional groups the intensity of N 1s peak for lower coverage was too low to reasonably judge changes. Tabular values for C 1s and N 1s are again marked by grey vertical lines. The black spectra correspond to the molecular self-assembly of DCA molecules. Unlike HATCN, DCA molecules contain only two types of differently bound carbon atoms – one type in the anthracene core and one in the cyano functional groups – and only one type of nitrogen atoms – in the cyano functional groups. The XPS analysis of self-assembled DCA molecules was not reported yet, and thus there are no literature values of fitted C 1s peak for comparison. The N 1s peak is composed of only one peak.

The red spectra in Fig. 2.13 correspond to formed structures of DCA and Fe after the subsequent introduction of Fe atoms. The red C 1s peak is shifted to the lower binding energy with respect to the black one by roughly 0.5 eV. On account of the LEEM results correlating with parameters of MOFs reported in the literature, and thus the coordination bond being formed, the change might be caused by the bonding of cyano groups to Fe atoms. However, here again, the N 1s peak does not follow this prediction. The red spectra itself appears to have a peak shifted to lower binding energies, which would be in accordance with the statement. Although, when compared to the grey spectra of clean Ag(111), one can see a significant resemblance in which the peak appears just as noise. At the same time, the red spectra were measured with better resolution and it has an overall lower signal-to-noise ratio, thus we could ascribe it as a small bump at lower binding energies, i.e. where the red arrow points in (b). Moreover, a decrease in intensity of the N 1s peak is in agreement with a remarkable decrease observed also in the C 1s peak after the introduction of Fe atoms. This change might be connected to the deposition of high coverages of DCA, which behavior is not well studied yet and is left aside here to not assume a further conclusion.

To sum up, the XPS spectra again confirm that the Ag(111) substrate is covered by carbon and nitrogen atoms after the deposition of DCA molecules. After the introduction of Fe atoms, there is a significant visible change in the C 1s peak, and a possible

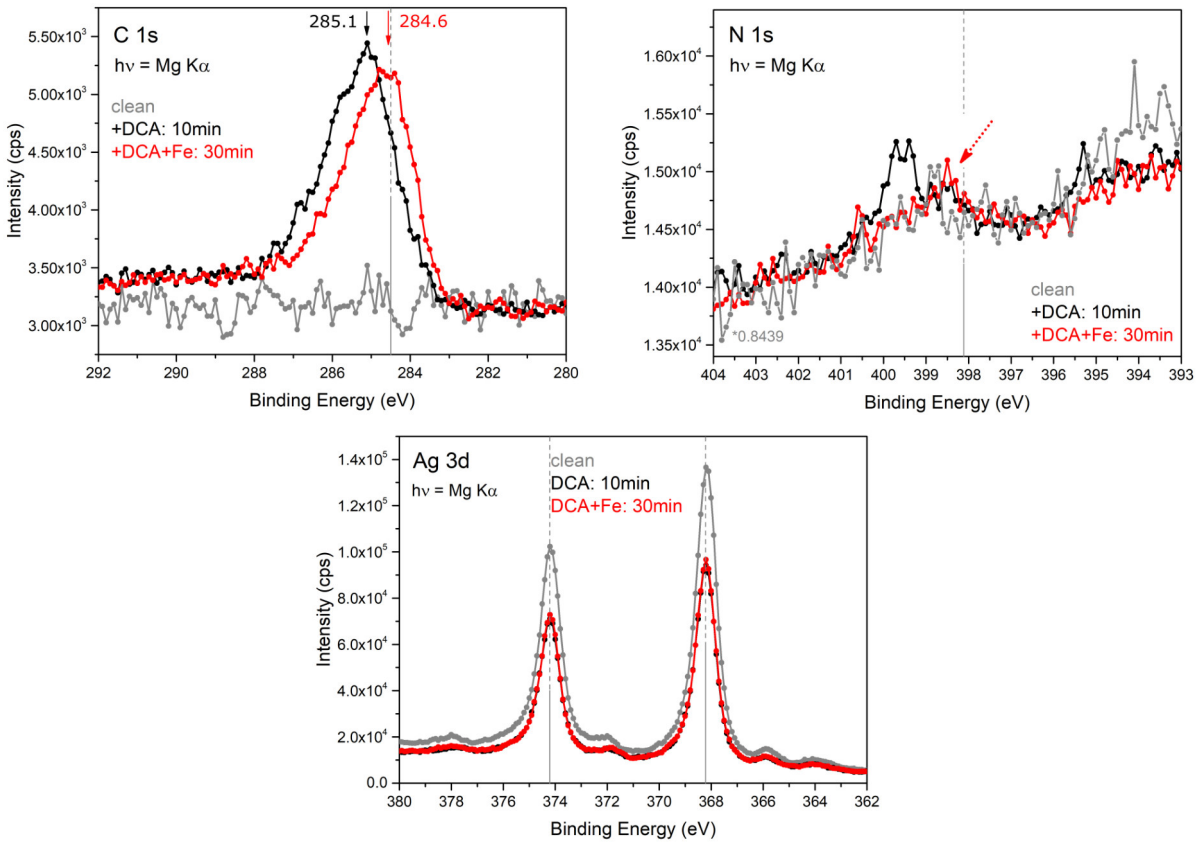

Figure 2.13: XPS spectra of the (a) C 1s region, (b) N 1s region, and (c) Ag 3d region, which is also noted in the left upper corner of the subfigures together with the type of source. The colour legend are present in each, +DCA stands for 10 min of DCA deposition (at 100 °C evaporator temperature), +DCA+Fe stands for 10 min of DCA deposition (at 100 °C) with sequential 30 min deposition of Fe (at 1030 °C). Red and black arrows in (a) represent the central position of measured peaks, and the red arrow in (b) points out a small bump in the red spectra and a possible difference at that energy between red and black spectra.

slight change in the N 1s one. In view of DCA coordination with Fe atoms shown in LEEM, we could ascribe these changes, at least partially, to the bond between DCA and Fe atoms. However, an XPS investigation of neither DCA self-assembly nor DCA coordination frameworks was performed before, the understanding thus remains narrow for now. The explanation might be more intricate and from XPS alone we cannot confirm the formation of the coordination bond.

To conclude, a long-range order of DCA metal-organic framework with Fe was achieved on the surface Ag(111). Molecules and metal centers form coordination bonds and arrange into a kagome and honeycomb superlattice, respectively. The grown structures are in the order of tenths of a μm in size. On the account of generating a recipe for the MOF formation on the Bi_2Se_3 substrate being our goal, we studied DCA self-assembly on Bi_2Se_3 as well. The latter will be described in the next chapter, in Sec. 3.2.1. In comparison to HATCN molecules, there is a recipe for MOF formation which might be transferred onto the TI surface.

3. Carbonitrile molecules on Bi_2Se_3

The final chapter deals with the topological insulator surface Bi_2Se_3 and how to transfer the knowledge of molecular self-assembly from coinage metal surfaces onto this weakly interacting surface. In particular the preparation of a clean substrate surface will be discussed first – a task that is not achieved easily in the used UHV set-up. Thus, first we will adress the delivery of a clean Bi_2Se_3 surface. Subsequently, the deposition of different molecules, that have been tested for coinage metals, will be discussed. As was discussed in the last chapter, no recipe for HATCN and Fe coordination was found, thus only a submonolayer deposition of HATCN will be reported. In the case of DCA, even though a recipe for a MOF formation was found and could be transferred, due to the limited time available, this work only reports on the molecular self-assembly of DCA on a weakly interacting surface.

3.1. Clean $Bi_2Se_3(0001)$ surface

As discussed in Sec. 1.2.3, cleavage of the sample can be executed in two ways. Neither the studied sample, due to its small thickness, nor the UHV cluster set-up, is suitable for the cleavage with a mechanical cleaver. Therefore, graphene-like exfoliation was the only performed. Fig. 3.1a shows two possible arrangements of such an exfoliation procedures in-situ, in our UHV cluster set-up. In a first attempt of exfoliation in-situ, an elaborate

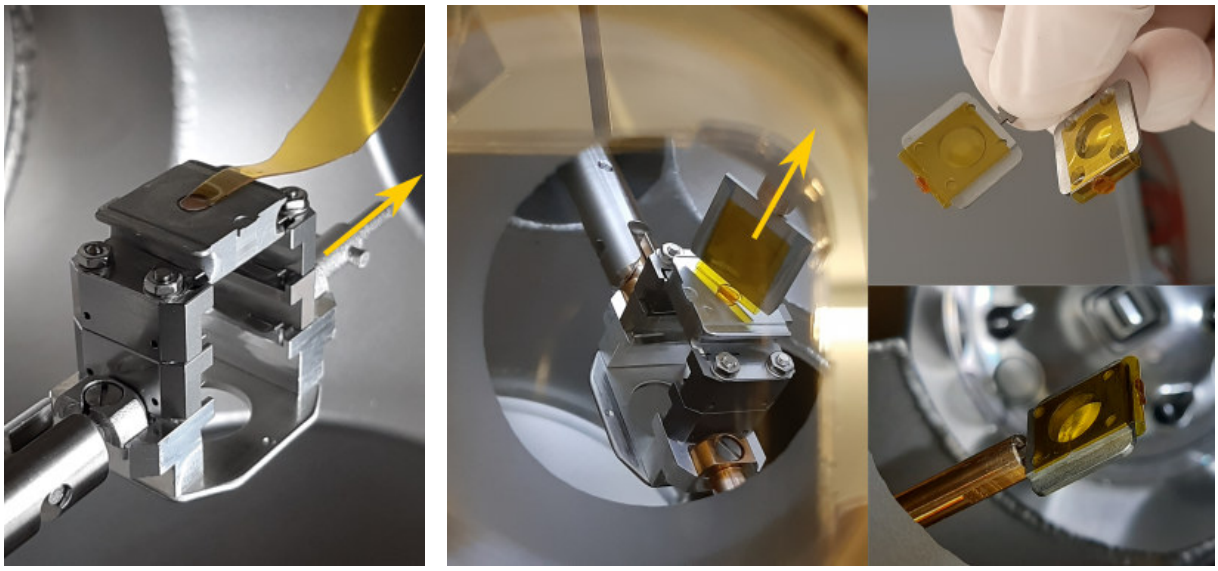

(a) (b)

Figure 3.1: Two possible arrangements of in-situ exfoliation in UHV system. (a) exfoliated by inserting the trolley with the sample into transfer line. (b) exfoliated by wobble stick mechanism described more in detail in text.

construction of Kapton tape was attached to the walls of the load-lock chamber and to the surface of a Bi_2Se_3 sample fixed in a sample holder. The end part of the tape is fixed on the sample as shown in Fig. 3.1a. To reach the surface of the Bi_2Se_3 crystal through the hole of the sample holder a little tower construction of Kapton circles had to be designed. This then was attached to the surface of the crystal and mounted in the

load lock. The exfoliation is then performed by sliding the whole trolley away from under the tape fixation spot in the load lock. This is visualized by the yellow arrow in Fig. 3.1a showing the direction of movement from the load lock to the UHV transfer system. The exfoliation was usually done at pressure of low to mid 10^{-8} mbar – the best-obtainable back pressure of the load lock without extensive waiting times of several hours.

This approach had a low rate of success as roughly just one exfoliation trial out of four was successful. Thus, another more suitable arrangement had to be found. Due to the extensive knowledge on exfoliation in our working group, a second strategy how to exfoliate the material in-situ was soon found and is thus described below. The difference of this second method is that the construction of Kapton tape cirles and tape is now put on an empty sample holder, which can be operated by a wobble-stick as shown in Fig. 3.1b. Approaching with the wobble-stick then results in the tape being attached to the surface. The exfoliation is then performed through the wobble-stick being withdrawn. Again in this case, Fig. 3.1b shows the details of the method applied and a yellow arrow highlights the direction of the exfoliation device being moved to produce the clean surface. The second method of exfoliation has a good success rate. The tape sticks to the sample by the little tower construction of Kapton circles and it peels off just the exposed part of the sample. However, once the surface is not showing any easy access points for the adhesiveness, i.e. easy starting points for the tearing off of the exfoliated material, the exfoliation becomes harder. However, so-far exfoliation did work to the extent necessary, but improvements will definitely be necessary in the upcoming future.

At the mesoscale, the clean surface differs slightly with every trial after in-situ exfoliation. One representative bright field image of the clean surface is shown shown in Fig. 3.2a. The exfoliation takes of multilayers of material away – sometimes in a non-uniform way.

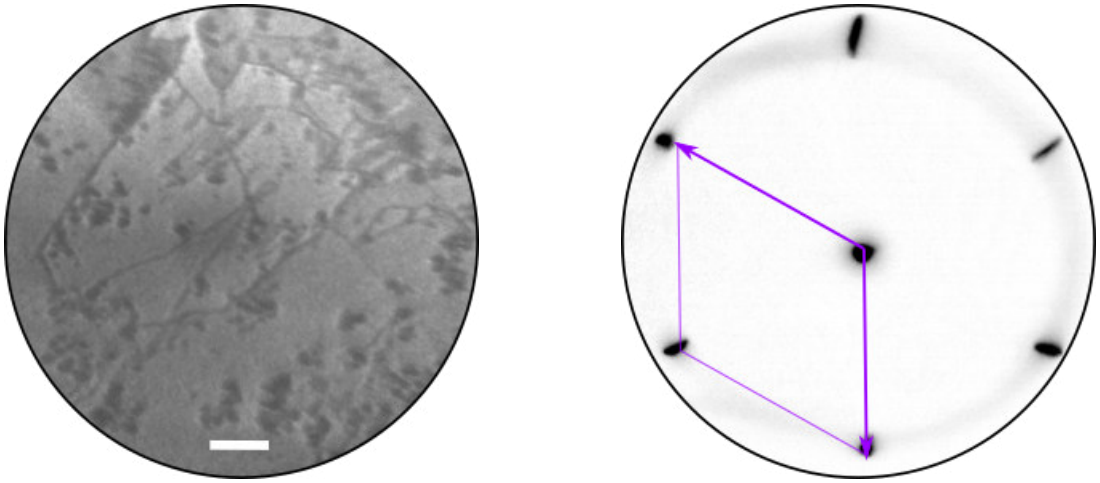

(a) (b)

Figure 3.2: The in-situ exfoliated Bi_2Se_3 surface imaged by LEEM. (a) In bright field image, the bright areas displays terraces of the Bi2Se3 surface, QL steps appear as dark lines. (b) Corresponding diffraction pattern showing a nice hexagonal pattern. Unit cell vectors represented in purple colour. Parameters: (a) 12 eV, (b) 16 eV. The white scale bar indicates a unit of 1 μm in length.

That way, terraces with alternating step differences are produced in the exfoliation and different QLs can be seen side-by-side in one image. As in the case of the LEEM images of the coinage metal surfaces, also here the dark lines indicate the step in neighbouring

QLs of the material. The dark island-like areas are somewhat puzzeling to us and either show contaminants from the tape or places where the exfoliation did work in a different way as anticipated producing Bi-rich surface areas or a different QL being exposed to the vacuum. In reciprocal space, there is a hexagonal diffraction pattern reflecting the symmetry of the QL (111) terminating surface. This is shown in Fig. 3.1b. A reciprocal unit cell has been inserted and is highlighted in purple colour.

The real space unit cell of the surface is also marked in the atomic resolution STM image of the in-situ exfoliated Bi_2Se_3, it can be found in Fig. 3.3. There, a large-scale image of 50×50 nm can be found in the left panel and a 10×10 nm image with atomic resolution is visualized on the right. According to to [77] and [78], the bright protrusions are the Se atoms in the topmost layer of the QL. Based on this STM image, the periodicity of Se atoms, and thus also the length of the purple unit cell vectors, is 0.40 ± 0.01 nm. The apparent high is approximately 10 pm. The surface structure in large scale is shown in the left panel of Fig. 3.3. The dark triangular depressions are Se vacancies or small holes in the topmost QL. The presence of triangular defects like a half-height QL induced by tape exfoliation has been also reported in literature [78]. The contaminants on the surface, visible as overly bright protrusions, are due to a contaminated ARPES (angle-resolved photoelectron spectroscopy) measurement done directly before the sample was put into the STM.

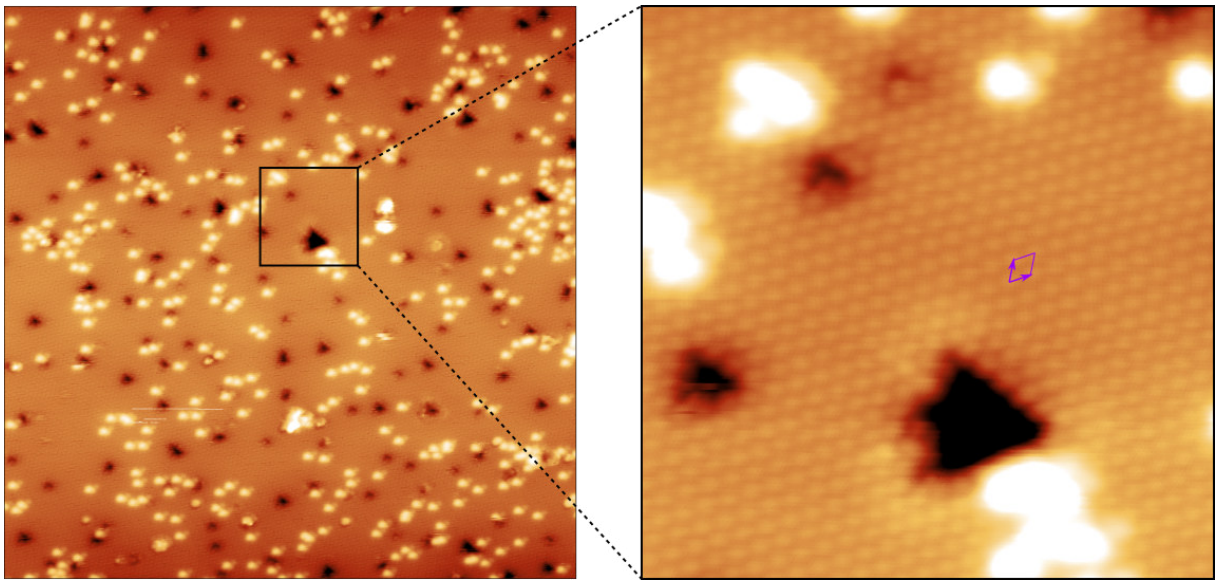

Figure 3.3: The in-situ exfoliated Bi_2Se_3 surface imaged by STM showing a large scale of 50×50 nm is shown on the left. It was taken after an ARPES measurement slightly contaminating the surface of the crystal. A magnification of the square 10×10 nm big area highlighted left is visualized in the right panel of the Figure. Atomically resolved Se atoms can be easily recognized as bright regular hexagonally arranged protrusions. Parameters: (left) -1 V, 50 pA, (right) -1 V, 50 pA, courtesy to Dr. Matthias Blatnik.

Due to the challenging set-up regarding the in-situ exfoliation, different possibilities for cleaning were considered. First, the cleanliness of an ex-situ exfoliated sample was studied and then compared to the in-situ exfoliated one. This was achieved by a little study applying LEIS (low energy ion spectroscopy) where help from Ing. Pavel Babík and doc Ing. Stanislav Průša, Ph.D. is greatly appreciated. This method is highly surface sensitive and reflects the chemical composition of only the first few layers. Thus, it

is ideal for the estimation of the respective differences in contamination. Three types of exfoliation were studied - in-situ exfoliation, and two types of differently ex-situ exfoliated samples. First, an exfoliation ex-situ in front of the UHV load-lock was tried with an air exposure for of just a few seconds (from now on termed ex-situ short). This allowed better control over the exfoliation process, although it still required a complex tape system of multilayered Kapton circles. The other ex-situ exfoliation was performed on the whole sample, before mounting it into the sample holder. Due to the mounting, the exposure was up to a few minutes (here-after called ex-situ long).

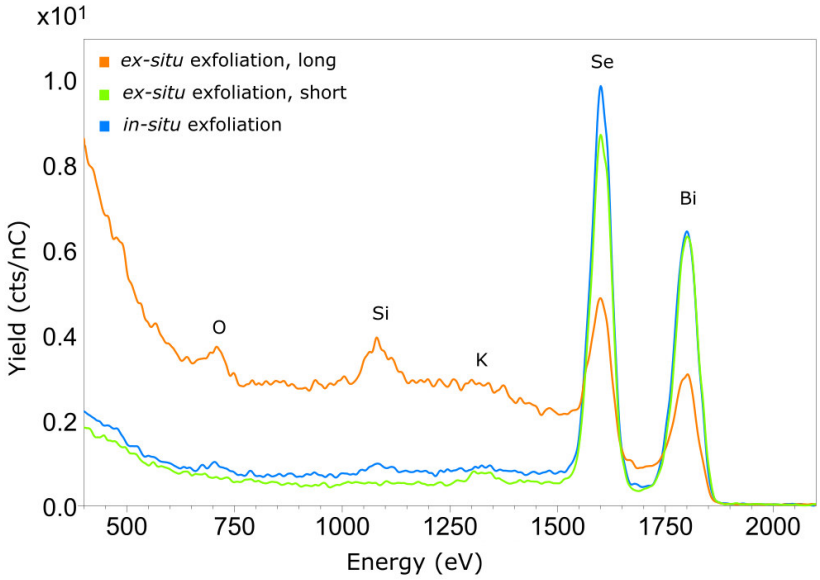

Figure 3.4: LEIS (low energy ion spectroscopy) spectra of the Bi_2Se_3 surface cleaned by three types of exfoliation. First, the in-situ exfoliation is depicted in bleu. Then, two spectra of differently ex-situ exfoliated samples are present. One with an air exposure for of just a few seconds, called short, is green colored, the other with an air exposure up to a few minutes, called long, is in orange. Help from Ing. Pavel Babík and doc Ing. Stanislav Průša, Ph.D. is greatly appreciated.

The graph in Fig. 3.4 shows the results of this investigation. As expected, the ex-situ long exfoliation resulted in the highest contamination, which manifests in the presence of peaks (denoted by element abbreviations) in the left part of the spectra This corresponds to contaminations of elements with a lower atomic number (e.g. O, Si or K). For the clean surface, we expect no peak in that area, which is true for both the in-situ and the short ex-situ exfoliation. An unexpected result is, that in this set of experiments, the ex-situ exfoliation spectra show the most clean surface. However, the in-situ procedure in LEIS conditions was not ideal, which might be the cause of the more contaminated resulting spectrum in the case of the in-situ exfoliation. Therefore, the bottom line from this investigation is that the ex-situ exfoliation with short air exposure exhibits a high cleanliness. Moreover, despite a successful in-situ exfoliation at first sight, it might not be an effective and completely successful one. On the contrary, the long exposure time introduced an elevated amount of contaminations from the ambient to the surface such that further care was needed to establish a clean surface. The latter, i.e. how to establish a clean surface after ex-situ exfoliation, will be further discussed in more detail.

Recently, it has been shown that ion bombardment and annealing (IBA) is an alternative preparation technique for cleaning thin samples which cannot be exfoliated [56]. IBA is suitable also as the further care needed to establish a clean surface after ex-situ exfoliation [6, 59]. A recipe for IBA cleaning was taken from [6, 56] and consists of repeated cycles of 10 minute long argon sputtering at 0.5 keV acceleration energy, and 20–30 minute long annealing. The adequate annealing temperature varied depending on the thickness of the sample and Zhou et al. showed that after reaching a certain threshold the surface structure is destroyed. Annealing to 430 °C was found to be safe in our conditions, where IBA is usually performed.

Ion sputtering is very invasive compared to the exfoliation and it might change the surface in an undesired way. While searching for annealing parameters, annealing in LEEM was discovered to show far better control of efficiently and sufficiently cleaning to surface. At the same time LEEM allows for an observation of mesoscale morphology in real-time. Thus, this procedure allows to more safely reach a higher temperature resulting in a more effective reconstruction of the surface.

Both approaches work and lead to a clean surfaces with triangularly shaped step-edges of QLs (see Fig. 3.5 (h) for details). And both procedures should lead to clean surfaces of the same quality as the in-situ exfoliated ones, i.e. Se-terminated and well-ordered, according to Roy et al. investigation [56]. Although, further LEIS measurement would be needed to confirm the Se-termination in our conditions. The reached cleanliness of the surface after LEEM annealing at a displayed temperature of 530 °C is usually the same, or better, than with described recipe of IBA.

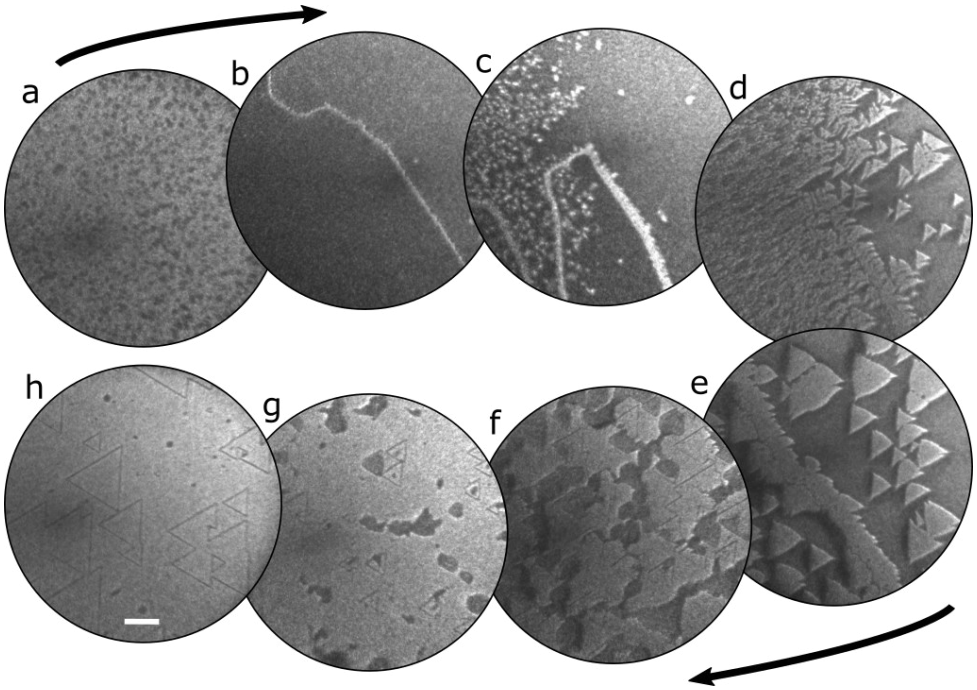

Figure 3.5: Bright field images of Bi_2Se_3 exfoliated ex-situ and annealed in LEEM to elevated temperaturs. The white scale bar indicates a unit of 1 μm in length. Parameters: 8 eV, 4A. The white scale bar indicates a unit of 1 μm in length.

As LEEM allows measurements in real-time, Fig. 3.5 shows an evolution (subfigure (a) to (h)) of the Bi_2Se_3 surface changing considerably in bright field LEEM during annealing to elevated temperatures after ex-situ exfoliation outside the UHV cluster. The arrows

indicate the time evolution of the experiment. The captured evolution follows quite nicely the evolution of the nucleation and island growth as described in theory Sec. 1.1. Panel (a) in Fig. 3.5 displays the morphology of Bi_2Se_3 surface with high contamination from ambient due to ex-situ exfoliation – contrast is very low, dark areas might correspond to the contaminants. With increasing temperature, the spots of dark areas vanish, and sharp bright lines appear, see (b). The latter become subsequently centers of further growth as it is captured in (c). In between (c) and (d), the density of islands still increases, but more slowly, suggesting the intermediate-coverage regime. Nonetheless, the islands also start already to join and percolate in some places. The triangular shape of growing islands is due to the three-fold symmetry of the QLs. The density of islands in (d) seems to reach the saturation and with further time on elevated temperature (see (e) to (h)), one can observe only the coalescence and percolation regime, i.e. the triangular islands join together and percolate as growing in size. With increasing size, dark lines start to appear on the bright areas of growing islands. Here the lines indicate the step edges of neighboring QLs of the material, as in the case of the bright field of in-situ exfoliated surface (see Fig. 3.2a). After reaching surface quality as depicted in panel (h), now again in Fig. 3.5, further annealing leads only to the reorganization of triangular terraces, no more change in contrast occurs.

To conclude, two arrangements of in-situ exfoliation were tried and a clean surface was achieved. The second method of exfoliation has also a good success rate. However, the clean surface differs slightly with every trial after in-situ exfoliation. Due to that fact, and due to the challenging set-up regarding the in-situ exfoliation, further investigation of molecular deposition was performed on the surface of Bi_2Se_3 exfoliated ex-situ and further cleaned in UHV conditions by annealing in LEEM.

3.2. Molecular depositions on Bi_2Se_3 surface

Clean Bi_2Se_3 surface is terminated by Se and thus has extremely low surface activity toward adsorbates. Molecule-substrate interactions are consequently very small and molecular self-assembly is directed almost exclusively by molecule-molecule interaction. At the same time, however, weakly interacting substrates have lower sticking abilities. Hence, an increase in deposition rate or time is required in order to create a population of adsorbed molecules high enough to enable the island nucleation and further growth. Due to the recent extensive investigation of molecular deposition on Bi_2Se_3 in our working group, it has been found that longer deposition times up to 90 min are needed to observe molecular structure on clean Bi_2Se_3 surface. Nevertheless, the rate of molecular desorption is very high even at RT, hence, the achieved coverage disappears usually within 30 min.

3.2.1. HATCN self-assembly

Deposition times of 30, 60, and 120 minutes were performed and the grown structure was analyzed in LEEM. The bright field image for each deposition time is shown in Fig. 3.6 (a−c), respectively. Dark lines represent step-edges of QL – same triangular terraces as already observed for the clean Bi_2Se_3 (see 3.5 (h)). Dark areas correspond to molecular growth. One can thus observe that HATCN molecules adsorb and form islands of seemingly triangular shape. However, no additional superlattice points appear in the

diffraction pattern for any of tried deposition times. This suggests that no structural 2D order is formed on the topological insulator surface when depositing the HATCN molecules at room temperature.

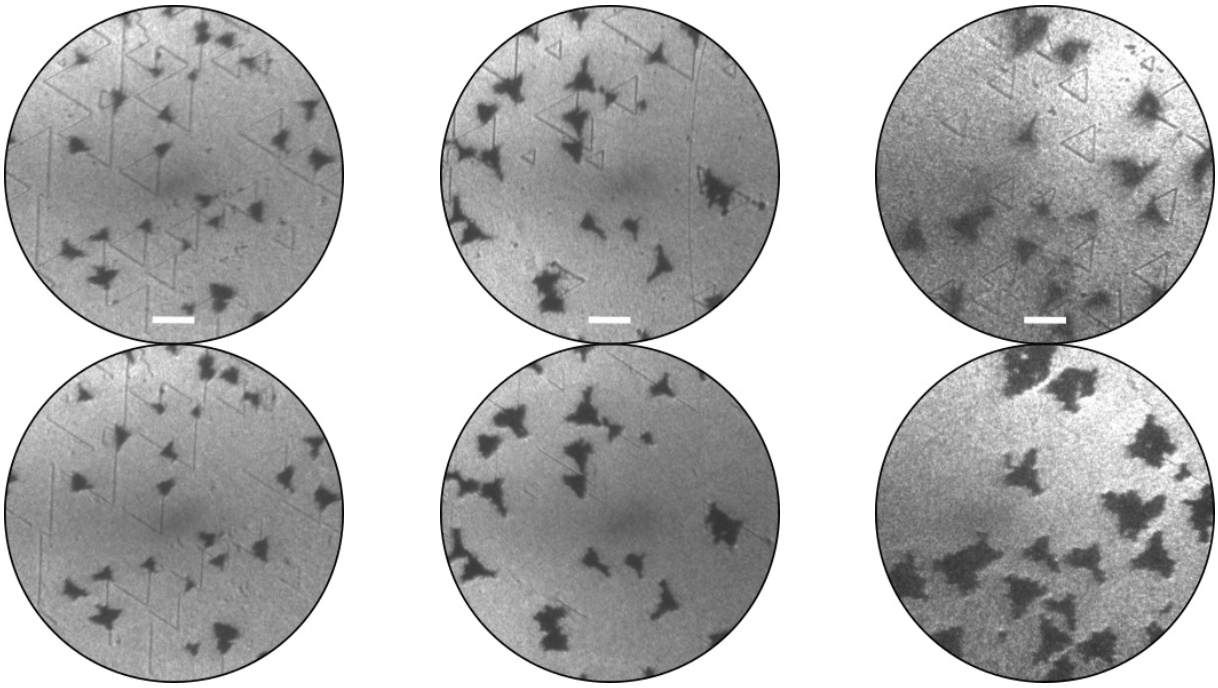

(a) (b) (c)

Figure 3.6: LEEM bright field images of Bi_2Se_3 surface with deposited HATCN molecule (a) 30 min, (b) 60 min, (c) 120 min. Depicted regions of upper and lower panels (a-c) match in size measured but are focused on different elements in the respective regions. Dark lines represent QL steps of Bi_2Se_3. Dark areas displays islands of grown HATCN molecular structure. Parameters: (a−c) 8 eV. The white scale bar indicates a unit of 1 μm in length.

Furthermore, in 3.6, the upper and lower images in (a-c) matches in depicted regions, but are focused on different details. The upper focuses on Bi_2Se_3 terraces, whereas the lower focus on grown islands. Focusing in order that both are sharp was troublesome. One had to refocus significantly in order to see the Bi_2Se_3 surface terraces or sharp shape of the island. This difficulty even increased with increasing coverage. When islands are in focus (the lower images), the dark lines corresponding to QL steps are barely visible in (b), and not anymore present in (c). That reflects a significantly different high of islands with respect to QL steps and suggests more than a monolayer of molecules. Furthermore, in the case of 30 min long deposition (a), the islands seem to grow into a compact triangular shape. However, the larger islands are, the more they seem to acquire the dendritic growth mode. Altogether, that leads us to believe that HATCN forms 3D structures on the surface of a topological insulator.

Besides, it has been reported that from a certain amount of HATCN deposited on Ag(111), molecules within the self-assembly reorganize themselves [32]. Frank et al. found that after saturation of the planar (face-on) monolayer, the molecules tend to stand up directly on the surface as the molecular density is increased, instead of planar growth of the second layer. Moreover, another study, investigating HATCN crystal obtained from solution, revealed that neutral molecules do not stack as they avoid self-π-complexation

due to their strong electron-deficient heterocycles [79]. Instead, they are significantly offset, and Szalay et al. found that the overall crystal packing leads to complicated, but highly symmetric, 3D hexagonal arrangement. In respect of Bi_2Se_3 being a van der Waals material with a weakly interacting surface, the adsorption of HATCN might be strongly related to a growth mode that strongly resembles 3D growth. And indeed, the collected LEEM bright field data hints at a 3D bulk-like growth of molecular islands on the surface of the topological insulator.

3.2.2. DCA self-assembly

For the deposition of DCA molecules on the Ag(111) surface, it was crucial to keep the backpressure low to avoid overload and to have the deposition rate under control. However, an extensive load of molecules is needed in order to reach a critical surface concentration on Bi_2Se_3 that leads to the nucleation of islands. In a bright field (see Fig. 3.7), the islands of DCA molecules show up as bright areas. The step-edges of QL appear as dark triangles and lines. The shape of the molecular islands is hard to define as seemingly there is one large island fragmented by the step-edges. The sequence of bright field images demonstrates how fast molecules disappear from under the beam. Overall, within 2 min the bright areas disappeared completely, exposing the Bi_2Se_3 surface. The mobility of DCA on Bi_2Se_3 is thus significantly higher than observed on the Ag(111).

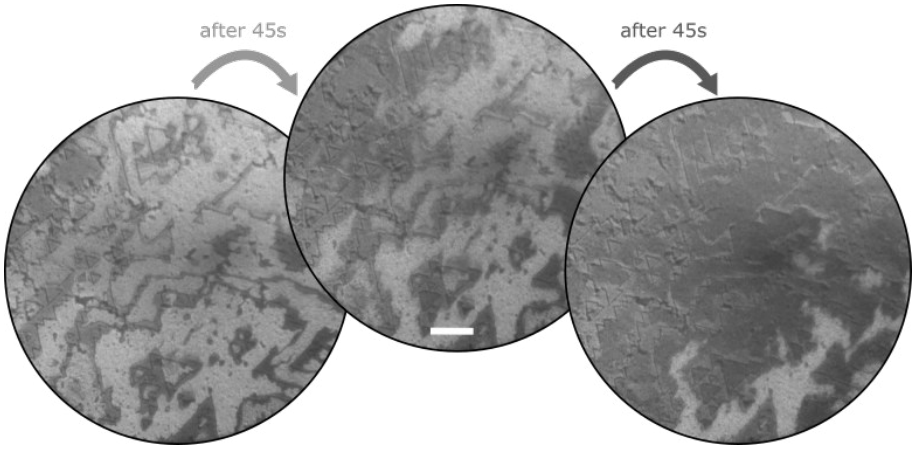

Figure 3.7: Bright field images of DCA molecules self-assembled on Bi_2Se_3(111). The bright areas correspond to molecular islands, dark to the Bi_2Se_3 substrate with triangular steps in QL. The sequence shows high mobility and desorption of molecules under the beam. Parameters: 8 eV. The white scale bar indicates a unit of 1 μm in length.

Further, the measured diffraction pattern is quite complex as seen in Fig. 3.8d. Micro-diffraction measurement revealed six different domains of DCA self-assembly. Those are depicted in Fig. 3.8 in already processed and colored form. All six merged together give rise to a coloured diffraction pattern, see Fig. 3.8h, that matches the measured one quite nicely. Thus, only six domains of DCA self-assembly are present on the Bi_2Se_3 surface. Compare individual micro-diffraction patterns to those observed for DCA on the Ag(111) surface (see Fig. 2.10), one could see resemblances. First, on the Ag(111) there were pairs of indistinguishable domains. Within the micro-diffractions on the Bi_2Se_3, there are pairs as well – distinguishable but very similar, specifically (a,b), (c,g), and (e,f). Second, the periodicity in the diffraction pattern is complex even for a single domain and exhibits a

high density of points along certain directions resulting in lines. On the other hand, the periodicity of the Bi_2Se_3 is highlighted in purple for all images in Fig. 3.8, and those lines do not follow the main directions of the surface lattice points as was the case of DCA self-assembly on the Ag(111).

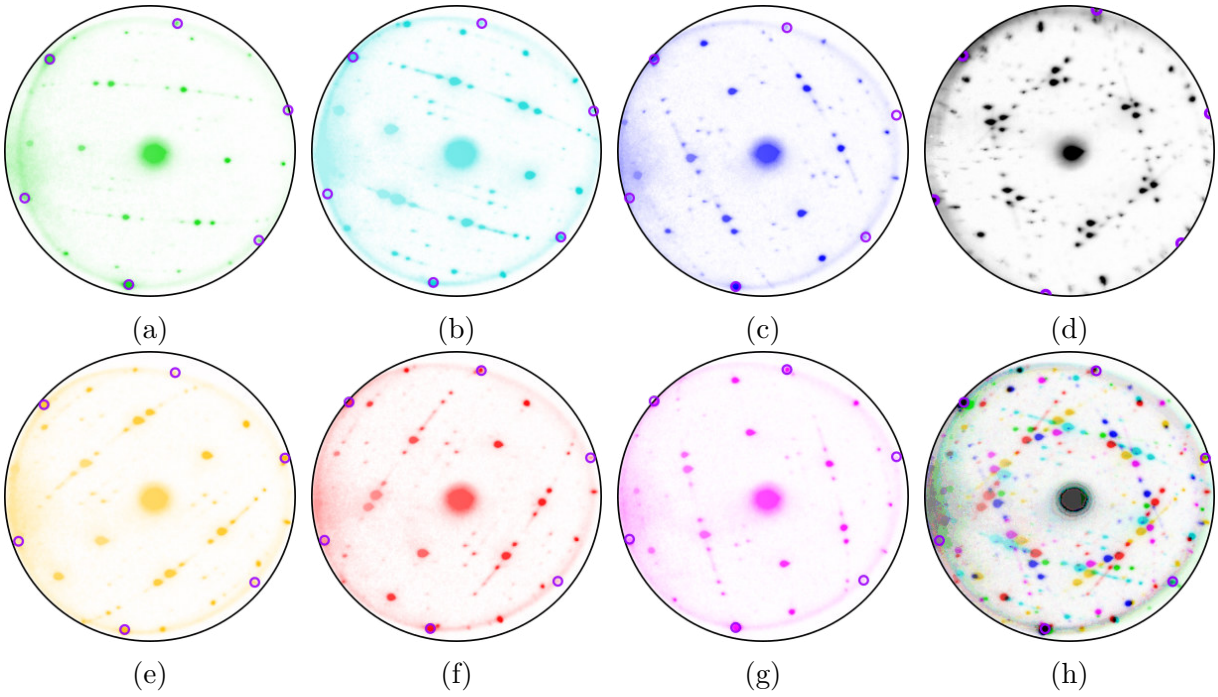

Figure 3.8: Self-assembled DCA molecules on clean Bi_2Se_3 surface imaged by LEEM diffraction mode. (a−c) and (e−g) displays measured micro-diffraction patterns of six individual domains. Measured patterns are processed and colored. (d) Measured diffraction pattern. (h) Composition of measured micro-diffraction patterns – six merged into one coloured. Purple rings highlight the Bi_2Se_3 lattice points in patterns. Parameters: (a-c) and (e-h) 16 eV, (d) 20 eV.

To sum up, a submonolayer coverage of DCA molecules was reached on the weakly interacting surface of Bi_2Se_3. It self-assembles into a pattern that to a certain extent resembles phase formation on the Ag(111). However, further investigation is needed to fully understand the phase formation of DCA molecules on the surface of a weakly interacting topological insulator. That is out of the scope of this work not only due to the complexity of the topic and limited time available but also due to room temperature conditions. High diffusivity and high rate of re-evaporation of molecules make measurements of the self-assembly at room temperature complicated, e.g. molecules desorb before an XPS spectrum is finished. At the same time, DCA is an appealing candidate for MOF formation on weakly interacting substrates and coordination bonds impart higher stability to the system. Therefore, extended analysis of the MOF structure at room temperature might be possible and will be further investigated in follow-up studies.

Conclusion

This thesis deals with the formation of self-assembled structures based on the carbonitrile molecules HATCN and DCA. The subject of the investigation was, first of all, the formation of molecular and metal-organic structures grown on low-index coinage metal surfaces. In this work Ag(111) and Au(111) were used in this regard. Further, we build on the acquired results as an additional goal was to transfer the obtained knowledge to a weakly interacting surface of the topological insulator Bi_2Se_3. Sample preparation and surface analysis were carried out in the UHV cleanroom complex of the CEITEC Nano infrastructure. Three experimental techniques were used to analyze the surface: STM, LEEM, and XPS.

For the fabrication of a MOF, it is first necessary to study the self-assembly of molecules alone. Therefore, the first step was to achieve an understanding of the monolayer coverage of HATCN and DCA molecules on coinage metal surfaces. We have confirm that HATCN molecules on Ag(111) form a well-known honeycomb (7×7) superstructure commensurate with substrate lattice. Moreover, a linear structure was observed in STM in the form of chains around the edges or between honeycomb regions, a detail not visible in the diffraction pattern. Only one domain of honeycomb structure was found by analysis of the diffraction pattern. Although, due to the chirality of the HATCN structure, there are two domains, which were revealed by STM. The behavior of HATCN on Au(111) is quite different from that of HATCN on Ag(111) comparing equivalent coverage. Long-range order of periodic arrangement was observed neither in LEEM nor in STM, only chains of linear arrangement flank the step edges. The DCA molecule was investigated only on the Ag(111) surface. There, the molecules form supramolecular structures showing complex periodicities in diffraction and unusual contrast changes in bright field of molecular islands under the electron beam in our LEEM experiments. A model was generated with the help of vectors reported in a recent STM study and we were thus able to identify a monoclinic superlattice in the measured diffraction pattern. This large periodicity is associated with a unit cell of the molecular superstructure. We observed also additional, more complex, smaller periodicities when imaging in micro-diffraction mode. This periodicities originate from the lattice mismatch of the molecular superstructure and the underlying Ag(111) substrate, which cause also the complex periodicity in the charging effect observed in STM. As we observed also combinations and site-dependent behaviour of the spot-appearance in micro-diffraction mode, we state here that a detailed analysis is complex and thus that a further, more detailed investigation would be needed to model all the appearing diffraction spots of all domains completely.

The understanding of molecular self-assembly then allowed for a deeper knowledge of a MOF's creation, e.g. changes in bonding. This was investigated in a second step on the same coinage surfaces. A series of experiments with HATCN molecules and Fe or Ni atoms was performed, however, neither of the tried combinations of parameters led to a large scale formation of a MOF on neither Ag(111) nor Au(111). We assume that the molecules are not able to form a large scale periodical arrangement featuring coordination. This might be caused by effects like the competing bonding interest of both N species within the molecule or the steric hinderence of adjacent cyano functional groups. DCA molecules, however, show high potential as a linker. A long-range ordered MOF with Fe atoms was achieved on the Ag(111) surface with a lattice of hexagonal symmetry. According to the literature, the observed structure can be subdivided into a honeycomb lattice that belongs

to the metal centers, and a kagome lattice belonging to the DCA molecules. By analyzing the LEEM data, we were able to identify two preferential orientations of Fe–DCA MOF with respect to the Ag(111) substrate, which then gives rise to three possible domains of the framework.

In order to transfer the obtained knowledge from the coinage metal surfaces to the weakly interacting surface of Bi_2Se_3, we had to overcome challenges of how to achieve an ultra-clean surface in our set-up and still be able to apply all necessary surface science techniques. The third step was to search for various cleaning mechanisms to obtain a clean surface of reproducible quality. Here, we present an optimized exfoliation in-situ method and cleaning by annealing of an ex-situ exfoliated sample in controlled conditions of the LEEM. The first one is favorable due to ensuring the intrinsic electronic properties. However, the quality of the prepared surfaces differ slightly in each experiment. The second method is simpler and more reliable, nonetheless, further experiments will be needed to confirm the Se termination of the surface after annealing and more importantly intact electronic properties. The last step then was to study molecular self-assembly on the clean Bi_2Se_3 surface. HATCN is unexpectedly stable on this weakly interacting surface, however, do not form any nice 2D periodicity. Based on bright field measurement, we conclude here that the adsorption of HATCN might be strongly related to a growth mode that strongly resembles 3D growth reported for HATCN self-assembly in solution. On the contrary, highly mobile molecular self-assembly was observed for DCA deposited on Bi_2Se_3. We were able to identify six rotational domains of the DCA self-assembly on the surface, although further experiments are needed to determine the unit cell of the superlattice, or the exact orientation with respect to the substrate lattice. A high mobility of the molecules at room temperature together with a high re-evaporation rate rather complicates the experiments and low-temperature conditions might be needed here also for further investigations.

Although a MOF formation was shifted to after "work" due to the limited time available, we have built a rudimentary understanding for the topic and for further MOF formation in follow-up studies. In particular, the DCA molecule shows an interesting and complex behavior on both surfaces, Ag(111) and Bi_2Se_3, and thus will be further investigated targeting MOFs on Bi_2Se_3.

References

[1] LÜTH, H.: *Solid Surfaces, Interfaces and Thin Films.* Springer International Publishing, 2015. ISBN 978-3-642-13591-0.

[2] OURA, K.: *Surface Science An Introduction.* Open WorldCat, 2003. ISBN 978-3-662-05179-5.

[3] MacLEOD, J.M., ROSEI, F.: Molecular Self-Assembly on Graphene. *Small*, March 2014, vol. 10, no. 6, p. 1038–1049. DOI: 10.1002/smll.201301982

[4] KUMAR, A., et al.: Molecular assembly on two-dimensional materials. *Nanotechnology*, January 2017, vol. 28, no. 8, p. 082001. DOI: 10.1088/1361-6528/aa564f

[5] *Supramolecular chemistry on surfaces: 2D networks and 2D structures.* Editor Neil R. CHAMPNESS. Weinheim: Wiley-VCH, 2022. ISBN 978-3-527-34491-8

[6] ZHOU, W., et al.: Termination of Single-Crystal Bi_2Se_3 Surfaces Prepared by Various Methods. *Physical Review B*, November 2016, vol. 94, no. 19, p. 195408. DOI: 10.1103/PhysRevB.94.195408

[7] GENG, Y.-F., et al.: STM Probing the Supramolecular Coordination Chemistry on Solid Surface: Structure, Dynamic, and Reactivity. *Coordination Chemistry Review*, April 2017, vol. 337, n. n/a, p. 145–77. DOI: 10.1016/j.ccr.2017.01.014

[8] Champness, L., et al.: Two-Dimensional Supramolecular Chemistry on Surfaces. *Comprehensive Supramolecular Chemistry II, Elsevier*, 2017, vol. n/a, n. n/a, p. 181–99. DOI: 10.1016/B978-0-12-409547-2.12501-6

[9] ATKINS, P. W., De PAULA, J.: *Physical chemistry.* 9th ed, W.H. Freeman, 2010. ISBN 1-4292-1812-6.

[10] DONG, L., *et al.*: Self-Assembly of Metal–Organic Coordination Structures on Surfaces. *Progress in Surface Science*, August 2016, vol. 91, no. 3, p. 101–135. DOI: 10.1016/j.progsurf.2016.08.001

[11] LANDSKRON, K.: Inorganic coordination chemistry - 7.1 Bonding in Coordination Compounds. *Chemistry LibreTexts.*Published November 2021, accessed may 2023. See also https://chem.libretexts.org/Bookshelves/Inorganic_Chemistry.

[12] SAKAMOTO, K.: SURFACE ANALYSIS | Low-Energy Electron Diffraction. *Encyclopedia of Analytical Science*, Elsevier, 2005, p. 535–543. DOI: 10.1016/B0-12-369397-7/00603-8.

[13] HERMANN, K.: *Crystallography and Surface Structure: An Introduction for Surface Scientists and Nanoscientists.* Second, Revised and Expanded edition, Wiley-VCH, 2016. ISBN 978-3-527-33970-9

[14] WOODRUFF, D. P.: Encyclopedia of Materials: Science and Technology - Low-Energy Electron Diffraction. *Elsevier*, 2002, p. 1–4. DOI: 10.1016/B0-08-043152-6/01840-4.

[15] URGEL, J. I., et al.: Controlling Coordination Reactions and Assembly on a Cu(111) Supported Boron Nitride Monolayer. *Journal of the American Chemical Society*, February 2015, vol. 137, n. 7, p. 2420–2423. DOI: 10.1021/ja511611r

[16] KUMAR, A., et al.: Two-Dimensional Band Structure in Honeycomb Metal–Organic Frameworks. *Nano Letters*, September 2018, vol. 18, n. 9, p. 5596–5602. DOI: 10.1021/acs.nanolett.8b02062

[17] YAN, L., et al.: Synthesis and Local Probe Gating of a Monolayer Metal-Organic Framework. *Advanced Functional Materials*, May 2021, vol. 31, n. 22, p. 2100519. DOI: 10.1002/adfm.202100519

[18] JAKUB, Z., *et al.*: Remarkably stable metal–organic frameworks on an inert substrate: M-TCNQ on graphene (M = Ni, Fe, Mn). *Nanoscale*, 2022, vol. 14, no. 26, p. 9507-9515. DOI: 10.1039/D2NR02017C.

[19] STAVILA, V., *et al.*: MOF-based electronic and opto-electronic devices. *Chem. Soc. Rev.*, 2014, vol. 43, no. 16, p. 5994-6010. DOI: 10.1039/C4CS00096J

[20] LI, J., et al.: Low-Dimensional Metal–Organic Coordination Structures on Graphene. *The Journal of Physical Chemistry C*, May 2019, vol. 123, n. 20, p. 12730–12735. DOI: 10.1021/ja511611r

[21] DONG, Y., *et al.*: MOF-based electronic and optoelectronic devices. *ACS Catal.*, 2019, vol. 9, no. 3, p. 1779–1798. DOI: 10.1021/acscatal.8b04515.

[22] HAIGEN, H., *et al.*: Metal–Organic Frameworks as a Good Platform for the Fabrication of Single-Atom Catalysts. *ACS Catal.*, 2020, vol. 10, no. 12, p. 6579–6586. DOI: 10.1021/acscatal.0c01459.

[23] KRENO, E. L., *et al.*: Metal-organic framework materials as chemical sensors. *Chem Rev.*, 2012, vol. 8, no. 112(2), p. 1105-1125. DOI: 10.1021/cr200324t.

[24] SONG, X.,*et al.*: 2D Conductive Metal-Organic Frameworks for Electronics and Spintronics. *Science China Chemistry*, October 2020, vol. 63, no. 10, p. 1391–1401. DOI: 10.1007/s11426-020-9791-2.

[25] YUE, W., *et al.*: Spin-Gapless Semiconductors and Quantum Anomalous Hall Effects of Tetraazanaphthotetraphene-Based Two-Dimensional Transition-Metal Organic Frameworks on Spintronics and Electrocatalysts for CO_2 Reduction. *ACS Applied Electronic Materials*, February 2023, vol. 5, no. 2, p. 1243–1251. DOI: 10.1021/acsaelm.2c01694.

[26] TORRENTE, I. F., et al.: Structure and Electronic Configuration of Tetracyanoquino-dimethane Layers on a Au(111) Surface. *International Journal of Mass Spectrometry*, November 2008, vol. 277, no. 1–3, p. 269–73. DOI: 10.1016/j.ijms.2008.07.013

[27] FRAGGI, M. N., *et al.*: Bonding and Charge Transfer in Metal–Organic Coordination Networks on Au(111) with Strong Acceptor Molecules. *J. Phys. Chem. C*, 2012, vol. 116, no. 46, p. 24558–24565. DOI: 10.1021/jp306780n

[28] ABDURAKHMANOVA, N., *et al.*: Stereoselectivity and electrostatics in charge-transfer Mn- and Cs-TCNQ4 networks on Ag(100). *Nat Commun*, 2012, vol. 3, p. 930. DOI: 10.1038/ncomms1942

[29] TSENG, T. Ch.: *TCNQ-based Supramolecular Architectures at Metal Substrates.* [PhD thesis.] EPFL, Faculté de Science du base, Physics and Mathematics, 2010, 109p.

[30] KORMOŠ, L.: *2D Molecular systems at surfaces.* [Doctoral thesis.] Brno: VUT, FSI, 2020. 140 s. Thesis supervisor: doc. Ing. Jan Čechal, Ph.D.

[31] PubChem. *3D Conformer, Interactive Chemical Structure Model, Balls-and-Sticks.* Accessed May 2023. HATCN, DCA, TCNQ, HAT, HITP.

[32] FRANK, P., *et al.*: Layer Growth, Thermal Stability, and Desorption Behavior of Hexaaza-triphenylene-hexacarbonitrile on Ag(111). *The Journal of Physical Chemistry C*, 2010, vol. 114, no. 14, p. 6650-6657. DOI: 10.1021/jp100704v

[33] SEGURA, J. L., *et al.*: Hexaazatriphenylene (HAT) derivatives: from synthesis to molecular design, self-organization and device applications. *Chem. Soc. Rev.*, 2015, vol. 44, no. 19, p. 6850-6885. DOI: 10.1039/C5CS00181A

[34] LYU, C.-K., *et al.*: Synthesis of Single-Layer Two-Dimensional Metal–Organic Frameworks M3(HAT)2 (M=Ni, Fe, Co, HAT=1,4,5,8,9,12-hexaazatriphenylene) Using an On-Surface Reaction. *Angewandte Chemie International Edition*, 2022, vol. 61, no. 27, p. e202204528. DOI: 10.1002/anie.202204528

[35] KITAGAWA, S., MASAOKA, S.: Metal complexes of hexaazatriphenylene (hat) and its derivatives—from oligonuclear complexes to coordination polymers. *Coordination Chemistry Reviews*, 2003, vol. 246, no. 1, p. 73-88. DOI: 10.1016/S0010-8545(03)00109-7

[36] WON, S.-Y, *et al.*: Linear and Hexagonal Porous Structures of an Organic Charge Acceptor Hexaaza-triphenylene-hexacarbonitrile on Au(111) with CN $\cdot\cdot\cdot$ CN Dipolar Interactions. *J. Phys. Chem. C*, 2013, vol. 117, no. 41, p. 21371–21375. DOI: 10.1021/jp407173w

[37] FRANK, P., *et al.*: Layer growth and desorption kinetics of a discoid molecular acceptor on Au(111). *Chemical Physics Letters*, 2009, vol. 473, no. 04, p. 321–325. DOI: 10.1016/j.cplett.2009.04.019

[38] GLOWATZKI, H., *et al.*: "Soft" Metallic Contact to Isolated C60 Molecules. *Nano Lett.*, 2008, vol. 8, no. 11, p. 3825–3829. DOI: 10.1021/nl8021797

[39] GAO, Z.'A., et al.: Synthesis and Characterization of a Single-Layer Conjugated Metal–Organic Structure Featuring a Non-Trivial Topological Gap. *Nanoscaley*, 2019, vol. 11, no. 3, p. 878–881. DOI: 10.1039/C8NR08477G

[40] GAO, Z.'A., et al.: Design and Synthesis of a Single-Layer Ferromagnetic Metal–Organic Framework with Topological Nontrivial Gaps. *The Journal of Physical Chemistry C*, December 2020, vol. 124, no. 49, p. 27017–27023. DOI: 10.1021/acs.jpcc.0c08140

[41] ZHONG, W., et al.: Synthesizing Cr-Based Two-Dimensional Conjugated Metal-Organic Framework Through On-Surface Substitution Reaction. *Small*, February 2023, vol. n/a, n. n/a, p. 2207877. DOI: 10.1002/smll.202207877

[42] KUMAR, D. G., *et al.*: Electric Field Control of Molecular Charge State in a Single-Component 2D Organic Nanoarray. *ACS Nano*, 2019, vol. 13, no. 10., p. 11882-11890. DOI: 10.1021/acsnano.9b05950.

[43] KUMAR, D. G., *et al.*: Mesoscopic 2D Molecular Self-Assembly on an Insulator. *Nanotechnology*, February 2023, vol. 34, no. 20., p. 205601. DOI: 10.1088/1361-6528/acba20.

[44] MUNTWILER, M., *et al.*: Surface Science at the PEARL Beamline of the Swiss Light Source. *Journal of Synchrotron Radiation*, January 2017, vol. 24, no. 1, p. 354–366. DOI: 10.1107/S1600577516018646.

[45] LUO, M.: *An STM Study of Molecular Self-Assemblies on Cu(111): Structure, Interaction, and Effects of Confinement.* [Doctoral thesis.] UC Riverside, 2012, p. 94.

[46] YAN, L., *et al.*: On-Surface Assembly of Au-Dicyanoanthracene Coordination Structures on Au(111). *ChemPhysChem*, September 2019, vol. 20, no. 18., p. 2297–2300. DOI: 10.1002/cphc.201900255.

[47] YAN, L., *et al.*: Two-Dimensional Metal–Organic Framework on Superconducting $NbSe_2$. *ACS Nano*, November 2021, vol. 15, no. 11., p. 17813–17819. DOI: 10.1021/acsnano.1c05986.

[48] LOWE, B., *et al.*: Selective Activation of Aromatic C–H Bonds Catalyzed by Single Gold Atoms at Room Temperature. *Journal of the American Chemical Society*, November 2022, vol. 144, no. 46., p. 21389–21397. DOI: 10.1021/jacs.2c10154.

[49] KUMAR, D. G., *et al.*: Manifestation of Strongly Correlated Electrons in a 2D Kagome Metal–Organic Framework. *Advanced Functional Materials*, November 2021, vol. 31, no. 48., p. 2106474. DOI: 10.1002/adfm.202106474.

[50] KUMAR, D. G.: *Atomically Engineered Electronic Two-Dimensional Organic Nanostructures.* [Doctoral thesis.] Monash University, Faculty of Science - Physics and Astronomy, 2021, 196p.

[51] Lattice Constants for all the elements in the Periodic Table. *Lattice Constants of the elements.* Accessed May 2023. See also https://periodictable.com/Properties/A/LatticeConstants.html.

[52] YAN, L., *et al.*: Synthesis and Local Probe Gating of a Monolayer Metal-Organic Framework. *Advanced Functional Materials*, May 2021, vol. 31, no. 22., p. 2100519. DOI: 10.1002/adfm.202100519.

[53] ORTMANN, F., ROCHE, S., O. VALENZUELA, S. *Topological Insulators.* Editor Neil R. CHAMPNESS. Wiley-VCH, 2015, ISBN 978-3-527-33702-6

[54] MAZUMDER, K., SHIRAGE, P. M.: A Brief Review of Bi_2Se_3 Based Topological Insulator: From Fundamentals to Applications. *Journal of Alloys and Compounds*, December 2021, vol. 888, n. n/a, p. 161492. DOI: 10.1016/j.jallcom.2021.161492

[55] SEVRUIK, V.: *Scanning tunneling microscopy study of Bi_2Se_3(0001) and of FeSe and Bi nanostructures on Bi_2Se_3(0001).* [Doctoral thesis.] Halle-Wittenberg: MLU, Faculty of Natural Sciences II - Chemistry, Physics and Mathematics, 2017, 95p.

[56] ROY, S., et al.: Atomic relaxations at the (0001) surface of Bi_2Se_3 single crystals and ultrathin films. *Physical Review B*, October 2014, vol. 90, no. 15, p. 155456. DOI: 10.1103/PhysRevB.90.155456

[57] ZHANG, Y. N.: Communication: Surface Stability and Topological Surface States of Cleaved Bi_2Se_3: First-Principles Studies. *The Journal of Chemical Physics*, October 2015, vol. 143, no. 15, p. 151101. DOI: 10.1063/1.4933298

[58] Della PIA, A., *et al.*: TCNQ Physisorption on the Topological Insulator Bi_2Se_3. *ChemPhysChem*, September 2018, vol. 19, no. 18, p. 2405–2410. DOI: 10.1002/cphc.201800259

[59] CAVALLIN, A., et al. Preparation and Characterization of Bi_2Se_3(0001) and of Epitaxial FeSe Nanocrystals on Bi_2Se_3(0001). *Surface Science*, April 2016, vol. 646, p. 72–82. DOI: 10.1016/j.susc.2015.09.001

[60] HASAN, M. Z., KANE, C. L.: Colloquium: Topological Insulators. *Reviews of Modern Physics*, November 2010, vol. 82, no. 4, p. 3045–67. DOI: 10.1103/RevModPhys.82.3045

[61] CAPUTO, M., et al.: Manipulating the Topological Interface by Molecular Adsorbates: Adsorption of Co-Phthalocyanine on Bi_2Se_3. *Nano Letters.* 2016, vol. 16, no. 6, p. 2405-2410. DOI: 10.1021/acs.nanolett.5b02635

[62] YU, R., et al.: Quantized Anomalous Hall Effect in Magnetic Topological Insulators. *Physical Review B*, July 2010, vol. 329, n. 5987, p. 61–64. DOI: 10.1126/science.1187485

[63] CHANG, C.-Z., et al.: Experimental Observation of the Quantum Anomalous Hall Effect in a Magnetic Topological Insulator. *Science*, April 2013, vol. 340, n. 6129, p. 167–170. DOI: 10.1126/science.1234414

[64] KITAZAWA, T., *et al.*:Topological Surface State of Bi 2 Se 3 Modified by Adsorption of Organic Donor Molecule Tetrathianaphthacene. *Advanced Materials Interfaces*, July 2020, vol. 7, no. 14, p. 2000524. DOI: 10.1002/admi.202000524

[65] MOUE, R., *et al.*: Topological Surface State of Bi_2Se_3 Modified by Physisorption of n-Alkane. *ChemNanoMat*, March 2023, vol. 9, no. 3, p. e202200538. DOI: 10.1002/cnma.202200538

[66] KUROWSKÁ, A.: *Metal-organic networks on graphene.* [Bachelor thesis.] Brno: VUT FSI, 2021, 35p. Thesis supervisor: doc. Ing. Jan Čechal, Ph.D.

[67] KOVAŘÍK, Š.: *Self-assembled molecular layers on epitaxial graphene.* [Master's thesis.] Brno: VUT, FSI, 2018. 54 s. Thesis supervisor: doc. Ing. Jan Čechal, Ph.D.

[68] BAUER, E.: Surface microscopy with low energy electrons: LEEM. *Journal of Electron Spectroscopy and Related Phenomena*, 2020, vol. 241, no. 28, p. 146806. DOI: 10.1016/j.elspec.2018.11.005.

[69] HALLIDAY, D., RESNICK, R., WALKER, J.: *Fyzika.* Redakce českého vydání Petr Dub. Brno: VUT, nakladatelství VUTIUM, druhé vydání. ISBN 978-80-214-4123-1

[70] ÅHLUND, J.: *Electronic and Geometrical Structure of Phthalocyanines on Surfaces An Electron Spectroscopy and Scanning Tunneling Microscopy Study.* [PhD thesis.] Uppsala Universitet, Faculty of Science and Technology, 2007, 67p.

[71] JIA, J.-F., *et al.*: Scanning Tunneling Microscopy. *Handbook of Microscopy for Nanotechnology*, edited by Yao and Wang, Kluwer Academic Publishers, 2005, pp. 55–112. DOI: 10.1007/1-4020-8006-9_3.

[72] OSWALD, S.: X-ray Photoelectron Spectroscopy in Analysis of Surfaces. Update based on the original article by Steffen Oswald, *Encyclopedia of Analytical Chemistry*, March 2013, John Wiley & Sons, Ltd. DOI: 10.1002/9780470027318.a2517.pub2.

[73] ČECHAL, J.: *Analýza povrchu a tenkých vrstev využitím fotoelektronové spektroskopie.* [Dizertační práce] Brno: FSI VUT. ISBN 80–214–3209–8.

[74] MORENO, D., *et al.*: Dysprosium-Directed Metallosupramolecular Network on Graphene/Ir(111). *Chemical Communications*, 2021, vol. 57, no. 11, p. 1380–1383. DOI: 10.1039/D0CC07315F.

[75] SHAIEK, N., et al.: Self-Organized Kagomé-Lattice in a Conductive Metal-Organic Monolayer. *Advanced Materials Interfaces*, August 2022, vol. 9, n. 23, p. 2201099. DOI: 10.1002/admi.202201099

[76] MULER, K., et al.: Triphenylene-Derived Electron Acceptors and Donors on Ag(111): Formation of Intermolecular Charge-Transfer Complexes with Common Unoccupied Molecular States. *Small*, August 2019, vol. 15, n. 33, p. 1901741. DOI: 10.1002/smll.201901741

[77] HANAGURI, T., et al.: Momentum-Resolved Landau-Level Spectroscopy of Dirac Surface State in Bi_2Se_3. *Physical Review B*, August 2010, vol. 82, n. 8, p. 081305. DOI: 10.1103/PhysRevB.82.081305

[78] URAZHDIN, S., et al.: Surface Effects in Layered Semiconductors Bi_2Se_3 and Bi_2Te_3. *Physical Review B*, February 2004, vol. 69, n. 8, p. 085313. DOI: 10.1103/PhysRevB.69.085313

[79] SZALAY, P. S., et al.: HAT(CN)6: A New Building Block for Molecule-Based Magnetic Materials. *Synthetic Metals*, August 2001, vol. 122, no. 3, p. 535–42. DOI: 10.1016/S0379-6779(01)00342-3

List of used abbreviations and symbols

2D	Two-dimentional
3D	Three-dimentional
$a_{\mathrm{Ag/Au}}$	Unit cell size of Ag(111) or Au(111) surface
a_{DCA}	Unit cell size of DCA self-assembly
a_{HATCN}	Unit cell size of HATCN self-assembly
A	Aperture
ARPES	Angle resolved photoelectron spectroscopy
Bi_2Se_3	Bismuth selenide
CEITEC	Central European Institute of Technology
DCA	Dicyanoanthracene
Fe	Iron
Gr/Ir(111)	Graphene grown on Ir(111)
HAT	Hexaza-triphenylene
HATCN	Hexaza-triphenylene-hexacarbbonitrile
HATCN	Hexaimino-triphenylene
LEEM	Low-energy electron microscopy
LEIS	Low energy ion spectroscopy
MOF	Metal-organic framework
QL	Quintuple layer
STM	Scanning tunneling microscopy
TCNQ	Tetracyanoquinodimethane
TI	Topological insulator
UHV	Ultra high vacuum
XPS	X-ray photoelectron spectroscopy